

AD-A161 487

AGE HARDENING OF BINARY IRON-NICKEL MARTENSITES(U)
MICHIGAN UNIV ANN ARBOR DEPT OF MATERIALS AND
METALLURGICAL ENGINEERING J T CARTER ET AL. JUL 85

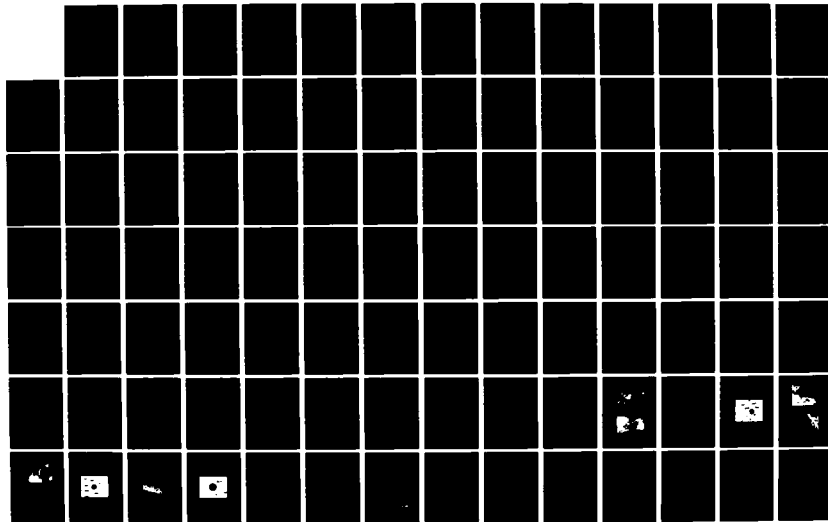
1/2

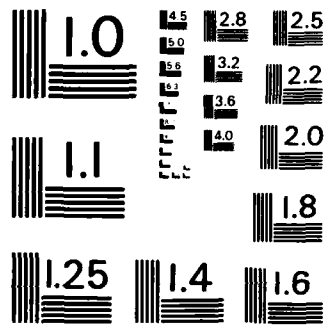
UNCLASSIFIED

ARO-17752.3-MS DAAG29-81-K-0052

F/G 11/6

NL





MICROCOPY RESOLUTION TEST CHART
NATIONAL BUREAU OF STANDARDS-1963-A

E

AGE HARDENING OF BINARY IRON-NICKEL MARTENSITES

FINAL REPORT

J.T. CARTER, ZHANG GUOSHENG* AND W.C. LESLIE

JULY 1985

U.S. ARMY RESEARCH OFFICE

CONTRACT NO. DAAG29-81-K-0052

MATERIALS AND METALLURGICAL ENGINEERING
THE UNIVERSITY OF MICHIGAN
ANN ARBOR, MICHIGAN

*MECHANICAL ENGINEERING
NANJING MACHINE BUILDING INSTITUTE
NANJING, CHINA

DTIC
ELECTE
NOV 20 1985
S A D

APPROVED FOR PUBLIC RELEASE:
DISTRIBUTION UNLIMITED

AD-A161 407

DTIC FILE COPY

THE VIEWS, OPINIONS, AND/OR FINDINGS CONTAINED IN THIS REPORT
ARE THOSE OF THE AUTHOR(S) AND SHOULD NOT BE CONSTRUED AS AN
OFFICIAL DEPARTMENT OF THE ARMY POSITION, POLICY, OR DECISION,
UNLESS SO DESIGNATED BY OTHER DOCUMENTATION.

-D 4/6/87

REPORT DOCUMENTATION PAGE		READ INSTRUCTIONS BEFORE COMPLETING FORM
1. REPORT NUMBER <i>ARO 17752.3-MS</i>	2. GOVT ACCESSION NO. N/A	3. RECIPIENT'S CATALOG NUMBER N/A
4. TITLE (and Subtitle) AGE HARDENING OF BINARY IRON-NICKEL MARTENSITES	5. TYPE OF REPORT & PERIOD COVERED Final, 2/81 - 5/85 <i>6 Feb 81 - 31 May 85</i>	
	6. PERFORMING ORG. REPORT NUMBER	
7. AUTHOR(s) J.T. Carter, Zhang Guosheng*, and W.C. Leslie *Nanjing Machine Building Institute, Nanjing, China	8. CONTRACT OR GRANT NUMBER(s) DAAG29-81-K-0052	
9. PERFORMING ORGANIZATION NAME AND ADDRESS Materials and Metallurgical Engineering The University of Michigan Ann Arbor, MI 48109-2136	10. PROGRAM ELEMENT, PROJECT, TASK AREA & WORK UNIT NUMBERS N/A	
11. CONTROLLING OFFICE NAME AND ADDRESS U. S. Army Research Office Post Office Box 12211 Research Triangle Park, NC 27709	12. REPORT DATE July 1985	
	13. NUMBER OF PAGES	
14. MONITORING AGENCY NAME & ADDRESS (if different from Controlling Office) Department of The Navy ONR Resident Representative 1314 Kinnear Road Columbus, OH 43121	15. SECURITY CLASS. (of this report) Unclassified	
	15a. DECLASSIFICATION/DOWNGRADING SCHEDULE	
16. DISTRIBUTION STATEMENT (of this Report) Approved for public release; distribution unlimited.		
17. DISTRIBUTION STATEMENT (of the abstract entered in Block 20, if different from Report) NA		
18. SUPPLEMENTARY NOTES The view, opinions, and/or findings contained in this report are those of the author(s) and should not be construed as an official Department of the Army position, policy, or decision, unless so designated by other documentation.		
19. KEY WORDS (Continue on reverse side if necessary and identify by block number) Age Hardening, Precipitation, Fe - Ni Alloys.		
20. ABSTRACT (Continue on reverse side if necessary and identify by block number) Age hardening of binary Fe-Ni martensites was investigated to determine the nature and kinetics of the hardening reaction. Six Fe-Ni alloys containing 24 to 34 wt% Ni were austenitized, quenched, then cooled to either 16°C to retain austenite or to -196°C to promote the transformation to martensite. Specimens were aged at six temperatures between 270 and 450°C for up to 14,000 hr. Four other ferritic/martensitic alloys containing 5 to 30 wt% Ni, previously cold		

20. ABSTRACT CONTINUED

rolled and aged 8000 hr, also were aged. Specimens were studied by hardness and tensile testing, x-ray diffraction, electron microscopy, and Fe-57 Mossbauer spectroscopy.

Age hardening occurred in all of the 24 to 34 wt% Ni martensites and at all of the aging temperatures. The maximum hardening of 270 HV (up to 480 HV) occurred in an Fe-32Ni martensite upon aging 8000 hr at 300°C. Hardening was attributed to Ni-rich, disc-shaped, austenite particles formed on {110} matrix planes during aging. The typical particle in a hardened specimen was 15 nm in thickness by 150 nm in diameter. Ni contents of particles formed at 335 and 370°C were found to be 59 ± 5 and 57 ± 5 wt%, respectively. Ordering was not detected.

The 30 to 34 wt% Ni alloys cooled to 16°C were largely austenite, very soft (100 HV), and not age harden.

TABLE OF CONTENTS

LIST OF TABLES	v
LIST OF FIGURES	vi
LIST OF PUBLICATIONS	ix
LIST OF SCIENTIFIC PERSONNEL AND DEGREES AWARDED . .	x
CHAPTER	
1. INTRODUCTION AND STATEMENT OF PROBLEM	1
2. LITERATURE REVIEW	3
Maraging Steels	3
Ternary and Higher-Order Martensites	3
Binary Fe-Ni Martensites	4
Fe-Ni Alloys: Phase Transformations and Equilibria	7
Diffusionless Phase Transformations	7
Diffusional Phase Transformations	8
Volume Fraction Phase Analysis	20
Quantitative Metallography	21
X-Ray Diffraction	21
Mossbauer Spectroscopy	25
X-Ray Microanalysis	27
Microanalysis	27
Spurious X-Rays	28
Mossbauer Spectroscopy	29
Mossbauer Effect	31
Mossbauer Spectroscopy	34
Applications in Ferrous Metallurgy	36
3. EXPERIMENTAL	37
Materials	37
Composition and History	37
Thermomechanical Treatments	39
Aging	40
Testing and Analysis	41

Hardness Testing	41
Tensile Testing	42
Co K α X-Ray Diffraction	42
Mo K α X-Ray Diffraction	43
Chemical Analysis	44
Electron Microscopy and X-Ray Microanalysis.	44
Mossbauer Spectroscopy.	46
 4. RESULTS AND DISCUSSION	 48
Hardness Testing	48
Tensile Testing	53
Chemical Analysis	59
Co K α X-Ray Diffraction	61
Mo K α X-Ray Diffraction	61
Electron Microscopy	61
X-Ray Microanalysis	76
Mossbauer Spectroscopy	76
 5. SUMMARY OF RESULTS AND CONCLUSIONS	 83
ACKNOWLEDGEMENTS	84
APPENDIX	85
REFERENCES	87

LIST OF TABLES

Table

2.1	Structure of Fe-Ni Alloys Quenched from 1100°C (15)	8
2.2	Energies Associated with the Fe-57 14.4 keV Transition	33
3.1	Compositions (wt%) of the First Group of Alloys	37
3.2	Compositions (wt%) of the Second Group of Alloys	38
4.1	Mechanical Properties of Fe-Ni Martensites . .	59
4.2	O, N, and C Contents of Fe-30Ni Martensites . .	60
4.3	O, N, and C Contents of Fe-30Ni Martensites . .	60
4.4	Hyperfine Parameters for the Subspectra Fitted to the Spectrum in Figure 4.27b and for Various Fe-Ni Phases.	82

Accession For	
NHS - CRA&I	<input checked="" type="checkbox"/>
DTIC TAB	<input type="checkbox"/>
Unannounced	<input type="checkbox"/>
Justification	
By	
Date	
Availability Codes	
Dist	Avail and/or Special
A1	

LIST OF FIGURES

Figure

2.1	Hardness change (indicated by arrows) in Fe-Ni alloys upon aging 96 days at 350°C. The alloys containing 30-40 wt% Ni presumably were austenitic (2).	5
2.2	Age hardening of Fe-Ni martensites at (a) 335°C and (b) 400°C (1).	7
2.3	Proposed Fe-Ni phase diagram based on an x-ray diffraction study of aged specimens (27). . .	10
2.4	Proposed Fe-Ni phase diagram based on analytical electron microscopy of aged specimens (30).	11
2.5	Proposed Fe-Ni phase diagram (33).	12
2.6	Crystal structures of the ordered phases (a) FeNi (L1 ₀) and (b) Fe ₃ Ni and FeNi ₃ (L1 ₂). . .	12
2.7	Proposed Fe-Ni phase diagram based on an x-ray diffraction study of vapor-deposited-and-annealed specimens (35)	14
2.8	Proposed Fe-Ni phase diagram based on magnetization and x-ray diffraction studies, electron microscopy, and Mossbauer spectroscopy of electron-irradiated specimens (40).	16
2.9	Proposed Fe-Ni phase diagram based on electron microscopy of iron meteorites (and aged specimens ?) (50).	18
2.10	Proposed Fe-Ni phase diagram based on electron microscopy, electron microprobe studies, and Mossbauer spectroscopy of iron meteorites (54).	19

2.11	Possible sources of spectral contamination generated in the specimen chamber by x-rays (dashes) and electrons (solid lines) from the specimen.	30
2.12	Energy-level diagrams and γ -ray transmission spectra for nuclear transitions illustrating (a) resonant absorption for the case of source and absorber nuclei in identical environments, (b) isomer shift, (c) magnetic dipole splitting, and (d) electric quadrupole splitting.	32
4.1	Hardness of Fe-Ni specimens as quenched to \approx RT or as cooled to -196°C (1,2, and this work). .	49
4.2	Austenite content of Fe-Ni specimens as quenched to \approx RT or as cooled to -196°C . . .	49
4.3	Age hardening of Fe-Ni alloys cooled to -196°C before aging. (a) Fe-24Ni. (b) Fe-26Ni. . .	50
4.4	Age hardening of Fe-Ni alloys cooled to -196°C before aging. (a) Fe-28Ni. (b) Fe-30Ni. . .	51
4.5	Age hardening of Fe-Ni alloys cooled to -196°C before aging. (a) Fe-32Ni. (b) Fe-34Ni. . .	52
4.6	Age hardening of Fe-Ni alloys cooled to 16°C before aging. (a) Fe-24Ni. (b) Fe-26Ni. . .	54
4.7	Age hardening of Fe-Ni alloys cooled to 16°C before aging. (a) Fe-28Ni. (b) Fe-30Ni. . .	55
4.8	Age hardening of Fe-Ni alloys cooled to 16°C before aging. (a) Fe-32Ni. (b) Fe-34Ni. . .	56
4.9	Strain hardening and age hardening of Fe-Ni alloys initially cooled to -196°C . (a) Fe-5Ni (b) Fe-9Ni.	57
4.10	Strain hardening and age hardening of Fe-Ni alloys initially cooled to -196°C . (a) Fe-21Ni. (b) Fe-30Ni.	58
4.11	Co K α x-ray diffraction pattern from an Fe-32Ni specimen cooled to -196°C then aged 2000 hr at 335°C	62
4.12	Mo K α x-ray diffraction pattern from a rotating-and-tilting Fe-32Ni specimen as cooled to -196°C	63

4.13	Mo K α x-ray diffraction pattern from a rotating-and-tilting Fe-32Ni specimen cooled to -196°C then aged 60 hr at 400°C.	64
4.14	Mo K α x-ray diffraction pattern from a rotating-and-tilting Fe-32Ni specimen cooled to -196°C then aged 1000 hr at 400°C.	65
4.15	Austenite content of Fe-32Ni specimens cooled to -196°C before aging.	66
4.16	TEM images of an Fe-32Ni specimen as cooled to -196°C.	67
4.17	Electron diffraction pattern from the specimen shown in Figure 4.16.	69
4.18	TEM images of an Fe-32Ni specimen cooled to -196°C then aged 250 hr at 335°C.	70
4.19	TEM images of an Fe-32Ni specimen cooled to -196°C then aged 250 hr at 335°C.	71
4.20	Electron diffraction pattern from the specimen shown in Figures 4.18 and 4.19.	72
4.21	TEM image of particles extracted from an Fe-32Ni specimen cooled to -196°C then aged 8000 hr at 335°C.	73
4.22	Electron diffraction pattern from the particles shown in Figure 4.21.	74
4.23	TEM image of an Fe-30Ni specimen cooled to -196°C then aged 60 hr at 450°C.	75
4.24	Energy-dispersive x-ray spectra collected in the TEM/STEM.	77
4.25	Ni content of austenite formed by the decomposition of Fe-Ni martensites as determined by x-ray microanalysis of thin foils (94) and extracted particles (this work).	78
4.26	Mossbauer spectrum from the 12 μ m thick natural-Fe (\approx 2% Fe-57) foil used to calibrate the spectrometer.	79
4.27	Mossbauer spectra from \approx 10- μ m thick foils of Fe-30Ni (a) as cooled to -196°C and (b) cooled to -196°C, cold rolled, and aged 20,000 hr at 335°C.	80

LIST OF PUBLICATIONS

J.T. Carter, Zhang Guosheng, and W.C. Leslie, "Age Hardening of Binary Iron-Nickel Martensites", Proceedings of the 7th International Conference on the Strength of Metals and Alloys, Montreal, 12-16 Aug. 1985.

LIST OF SCIENTIFIC PERSONNEL AND DEGREES AWARDED

J.T. Carter Ph.D. (Metallurgical Engineering)

Zhang Guosheng

W.C. Leslie

CHAPTER 1

INTRODUCTION AND STATEMENT OF PROBLEM

Alloys of iron containing nickel are studied in the diverse fields of meteoritics, geology, and metallurgy. The iron meteorites contain 5 to 35 wt% Ni and are thought to have cooled in the solid state of the parent bodies at about 1°C per million years. Samples of iron meteorites assumed to exhibit at least local chemical and crystallographic equilibrium have been studied, and the results used to construct Fe-Ni phase diagrams. Conversely, such results have been used together with existing diagrams to infer the thermomechanical history of the meteorite and its parent body. Similar work has been done with samples of terrestrial native-metal Fe-Ni deposits to determine their history and that of the surrounding rock.

In metallurgy, Fe-Ni alloys are used as the tough Ni-steels (5% Ni), the hardenable maraging steels (18% Ni), the Invar alloy (36% Ni) which has an anomalously low coefficient of thermal expansion, and the magnetically soft Permalloy (79% Ni). Although these alloys have been used and studied for years, there is not a good consensus on the low-temperature phase equilibria and the physical phenomena responsible for some of the anomalous properties. Determination of the phase equilibria has been hindered by sluggish diffusion in these alloys below 500°C and by the difficulties in distinguishing between phases with similar crystal structures containing elements of comparable atomic number.

To enhance diffusion and thereby speed the approach to equilibrium in Fe alloys containing 5 to 30 wt% Ni, Miller and Leslie (1) quenched and subzero cooled specimens to form bcc martensites, then alternately cold rolled and aged them for 2000 hr at temperatures between 300 and 450°C . Upon aging at temperatures below 400°C the Fe-30Ni specimens became too hard (≈ 530 HV) to roll. Electron microscopy revealed precipitate particles in hardened specimens similar in appearance to those found in iron meteorites. Age hardening of an Fe-25Ni martensite had been reported earlier (2), but the hardening reaction was not determined.

The purposes of this work were (1) to further document the age hardening of binary Fe-Ni martensites, (2) to

determine the nature and kinetics of the age hardening reaction, and (3) to clarify, as possible, the low-temperature Fe-rich portion of the Fe-Ni equilibrium phase diagram. The working hypothesis was that the age hardening was due to precipitation of FeNi having the $L1_0$ structure.

The experimental approach taken was to age specimens for long times, then study them via mechanical testing and various radiative techniques.

CHAPTER 2

LITERATURE REVIEW

Maraging Steels

In this report the term "maraging steel" refers to any of the low-C Fe-rich alloys that are solution treated as austenite, cooled to form martensite, then age hardened.

Ternary and Higher-Order Martensites

Age hardening of Fe-rich martensites is perhaps best illustrated by the commercial maraging steels (3). These steels have a typical composition of 18 wt% Ni, 8 Co, 5 Mo, 0.4 Ti, 0.1 Al, less than 0.03 C, balance Fe. After air cooling from a 900°C austenitizing temperature they have a structure of bcc lath martensite and a hardness of ~300 HV. Upon aging for 3 hr at 480°C the hardness is increased to ~500 HV. The high hardness of maraged steels is attributed to (1) the large number of dislocations that formed during the austenite-to-martensite transformation and, primarily, (2) the large number of zones and/or precipitates that formed during the aging treatment. The zones and/or precipitates are small and closely spaced because the dislocations provide many heterogeneous-nucleation sites per unit volume (4). As would be predicted by this model, cold working of the martensite before aging increases the hardness of the aged material (5).

Numerous ternary and quaternary Fe-rich martensites also age harden considerably (3,6). Speich (7), for example, reported hardening of Fe-20Ni-X martensites where X is 2.7 Al, 11 Cu, 5 Mo, or 1-6 Ti. The Fe-20Ni-6Ti martensite hardened from 370 up to 800 HV upon aging for 8 hr at 500°C. Hardening of this alloy was attributed to the precipitation of Ni₃Ti.

Several types of zones/precipitates cause age hardening in Fe-rich martensites. These include:

1. Solute-rich zones.
Examples: Cu-rich zones formed in the early stages of aging of Fe-Ni-Cu alloys (6); Cr-rich zones in Fe-Co-Cr alloys (6).
2. Metallic or intermetallic precipitates.
Examples: Metallic Cu formed in the later stages of aging of Fe-Ni-Cu alloys (7); Ni_3Mo and FeTi in Fe-Ni-Co-Mo-Ti alloys (4).
3. Ordered zones.
Example: Fe(Co,Ni) (B2 structure) in the early stages of aging of Fe-Ni-Co alloys (8-10).
4. Austenite.
Examples: Austenite formed in the later stages of aging of Fe-Ni-Co alloys (8-11) and, possibly, in Fe-Ni-Co-Ti alloys (11).
5. Solute-lean ferrite.
Example: Ferrite formed in the later stages of aging of Fe-Ni-Co alloys (10).

According to Suzuki (6), maraging steels must contain at least two solutes. One solute is required to stabilize the austenite down to relatively low temperatures so that the fcc-to-bcc transformation is martensitic. A second, he contends, is required for an age-hardening reaction to occur. In some steels, one or more of the solutes may serve as both austenite stabilizer and as hardener. In Fe-Ni-Mn alloys, for example, both of the solutes are austenite stabilizers and both take part in the age-hardening reactions. The hardening precipitates reported for this system are Ni_3Mn (L1_2), NiMn (B2), and NiMn (L1_0) (6,12,13).

Binary Fe-Ni Martensites

In contrast to the large number of papers that address age hardening in Fe-rich ternary and higher-order martensites (Suzuki cites 249 in his review), only two papers address age hardening in Fe-rich, binary, Fe-Ni martensites. Buchwald (2) reported that the hardness of an Fe-25Ni martensite increased from 210 up to 270 HV upon aging for 96 days at 350°C. To explain the hardening, he suggested that "some form of ordering reaction to Fe_3Ni occurs." As shown in Figure 2.1, the hardness of other Fe-Ni alloys changed by less than 10 HV during the same aging treatment.

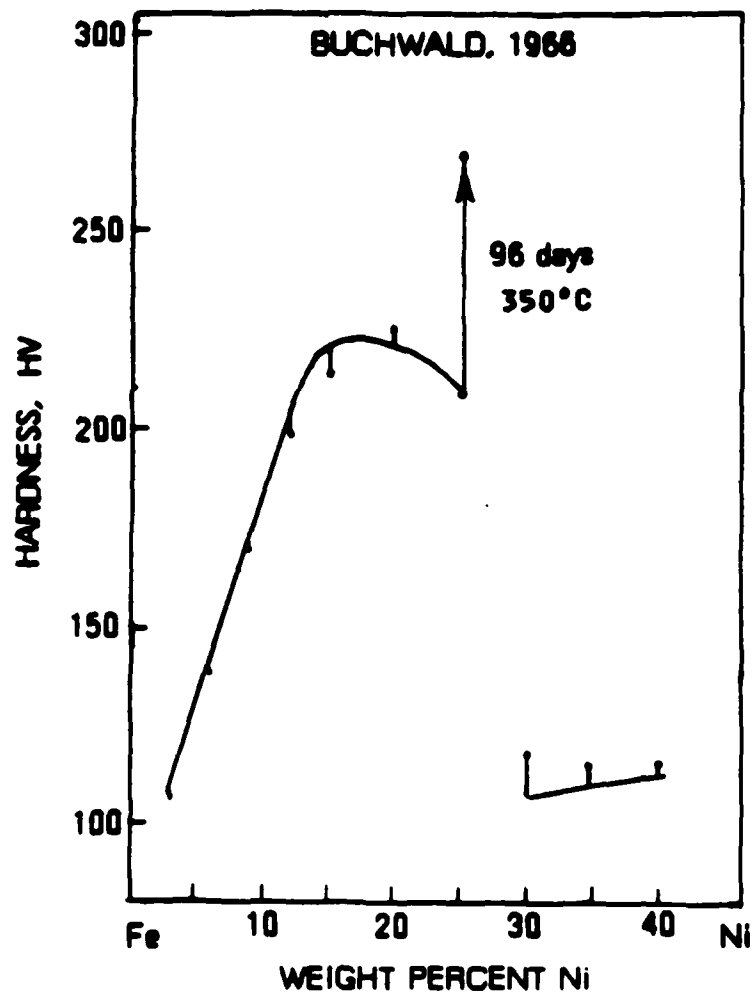


Figure 2.1 - Hardness change (indicated by arrows) in Fe-Ni alloys upon aging 96 days at 350°C. The alloys containing 30-40 wt% Ni presumably were austenitic (2).

Miller and Leslie (1) reported age hardening in a series of Fe-Ni martensites containing 20 to 34 wt% Ni upon aging for hundreds of hours at or below 400°C. As shown in Figure 2.2, the hardness increases were up to 225 HV. Hardening was accompanied by the formation of \approx 100-nm diameter disc-shaped particles in the martensites. Comparing Figures 2.1 and 2.2, the difference in hardness of the as-quenched high-Ni alloys is due to a difference in microstructure. Miller and Leslie's alloys were cooled to -196°C and therefore were martensitic. Buchwald's alloys presumably were cooled only to room temperature and therefore were largely austenitic.

Fe-Ni Alloys: Phase Transformations and Equilibria

Despite many studies of Fe-Ni alloys, there is not a consensus on the correct form of the low-temperature iron-rich portion of the Fe-Ni equilibrium phase diagram. This problem is due to the difficulties in producing equilibrated specimens and in identifying the phases produced. The normally sluggish diffusion in these alloys requires that specimens be aged long times at the temperature of interest or that diffusion be enhanced by some means. (According to Marsh (14), "... at all temperatures below 500°C, atomic diffusion either ceases or becomes negligibly small, consequently equilibrium is either impossible or extremely difficult to attain.") Since Fe and Ni have comparable atomic numbers, and since the phases reported to form have similar structures and may contain many defects, accurate phase identification requires very careful analysis. Phase transformations and phase equilibria in Fe-Ni alloys are discussed in this section.

Diffusionless Phase Transformations

Because of the austenite-stabilizing effect of Ni and the slow diffusion in Fe-Ni alloys, the phases found in most laboratory-prepared specimens as-cooled from an austenitizing temperature are not those found on the phase diagram. Which phases are present depends on the austenitizing temperature, prior austenite grain size, cooling rate, and coolant temperature, but all will have the same composition as the parent austenite. Table 2.1 lists the structures of Fe-Ni alloys quenched from 1100°C (to RT) as reported by Speich (15).

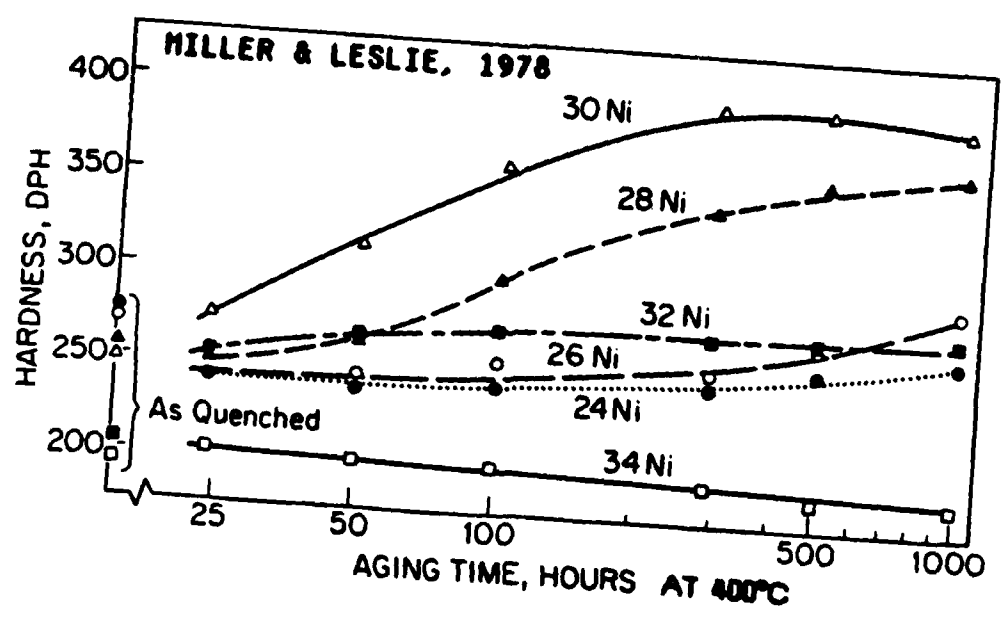
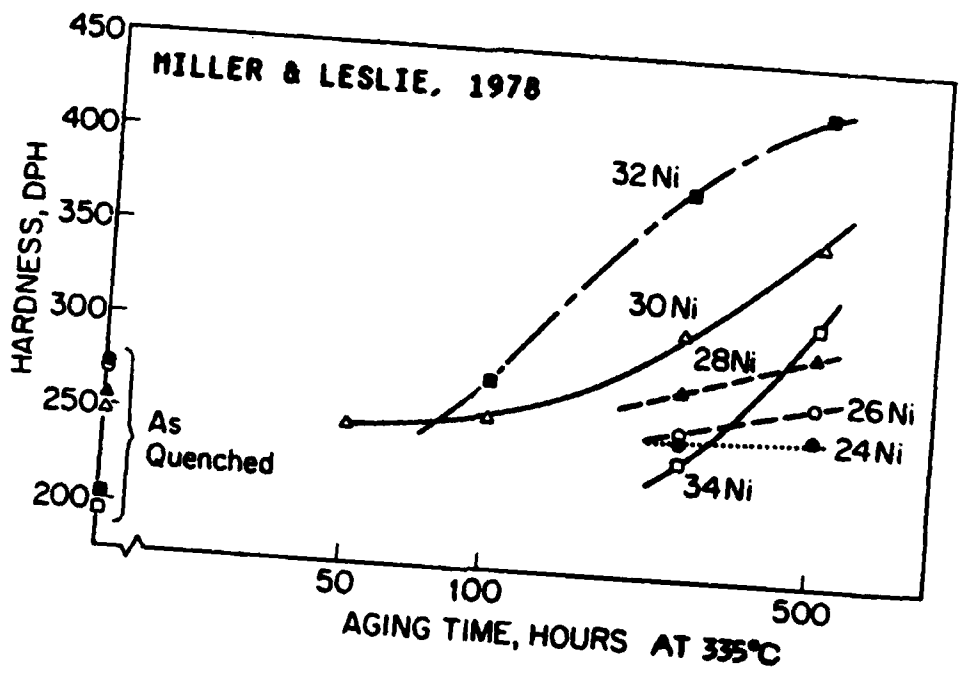


Figure 2.2 - Age hardening of Fe-Ni martensites at (a) 335°C and (b) 400°C (1).

Table 2.1 - Structure of Fe-Ni Alloys
Quenched from 1100°C (15).

<u>Ni content, wt%</u>	<u>Structure</u>
< 5	Massive ferrite
5 - 9	Massive ferrite + lath martensite
9 - 25	Lath martensite
25 - 29	Lath martensite + retained austenite
29 - 33	Plate martensite + retained austenite
33 - 35	Lath martensite + retained austenite
35 - 50	Austenite

The ferrite-martensite-austenite succession in Table 2.1 has been reported by several workers (16-21) with some variation in Ni content at the transitions. For example, Inokuti and Cantor (16) found that for splat-quenched alloys the martensite-austenite succession occurred at Fe-23Ni rather than Fe-35Ni.

Both the "forward" (fcc-to-bcc on cooling) and "reverse" (bcc-to-fcc on heating) transformations can occur martensitically. The M_s temperatures vary from 525°C for an Fe-9.5Ni alloy down to -223°C for an Fe-33Ni alloy (22,23). The corresponding A_s temperatures are 680 and 300°C. The reverse martensitic transformation produces austenite containing many dislocations and occasional twins (24), and has been used to strengthen Fe-32Ni austenites (25,26).

Diffusional Phase Transformations

Many workers have studied the diffusional phase transformations in Fe-Ni alloys using various types of specimens believed to be at least locally equilibrated (i.e., near interphase boundaries). These types include (1) bulk specimens cooled to form martensites, cold worked, then aged; (2) TEM thin foils aged in vacuum; (3) foils formed amorphous by deposition from vapors, then crystallized by annealing; (4) specimens irradiated with neutrons or electrons; (5) pieces of iron meteorites believed to have cooled extremely slowly; (6) pieces of iron meteorites corroded in the laboratory; and (7) terrestrial native-metal Fe-Ni specimens. The analytical techniques employed include polarized-light microscopy, x-ray diffraction, neutron diffraction, electron microscopy, Mossbauer spectroscopy, and thermal expansion, magnetization, and resistivity measurement. Existence of several Fe-Ni phases having different compositions, crystal structures, and magnetic properties has been proposed to

account for anomalies in physical properties; the presence, size, and shape of spectral lines or diffraction spots; and chemical-concentration gradients. Some of these works are discussed below.

Aging Studies

Some workers (1,27-31) have addressed the low-temperature equilibration problem in Fe-Ni alloys by quenching and cooling specimens from $\approx 1100^{\circ}\text{C}$ to 25, 0, or -196°C , then aging them at the temperatures of interest or alternately cold working and aging. The rationale for these treatments is that diffusion should be much faster in a bcc phase having many defects than in an fcc phase. Owen and Sully (27) studied aged alloys via x-ray diffraction, and constructed the phase diagram shown in Figure 2.3. Owen and Liu (28) verified that diagram except for the position of the α solvus below 400°C . They concluded that the solubility of Ni in α continues to increase linearly with decreasing temperature.

Goldstein and Ogilvie (29) studied alloys aged at 500 to 800°C with the electron microprobe. Their measured solubilities of Fe in γ at 500°C and Ni in α were higher than those of Owen and Liu by 4 and $\approx 1-2$ wt%, respectively. They also suggested that the solubility of Ni in α decreases with decreasing temperature below $\approx 400^{\circ}\text{C}$. Romig and Goldstein (30) studied alloys aged at 300 to 700°C with the analytical electron microscope, and constructed the diagram shown in Figure 2.4. Their data verified the earlier work (29), including the suggested retrograde α solvus below 400°C .

Ferro, Griffa, and Ortalli (31) quenched Fe-50Ni specimens from 1000°C to RT at cooling rates faster than $10,000^{\circ}\text{C}/\text{sec}$ to retain many vacancies, aged them for up to 100 hr at temperatures between 100 and 360°C , then collected Mossbauer spectra and resistivity and magnetization data. They suggested that partial ordering (to FeNi?) and some clustering or precipitation of Fe-rich regions occurred upon aging.

Hausch and Warlimont (32), exploiting the faster rate of surface diffusion, aged a TEM foil of slowly cooled Invar (fcc Fe-36Ni) to form an ordered precipitate which, by analogy to the Fe-Pt system, they identified as superparamagnetic Fe_3Ni . They later (33) presented the diagram shown in Figure 2.5, and reported that in a "well annealed, slowly cooled" Fe-31.5Ni specimen, metastable γ decomposed into stable γ plus Fe_3Ni . The structures of the ordered phases are shown in Figure 2.6. Jago (34) detected

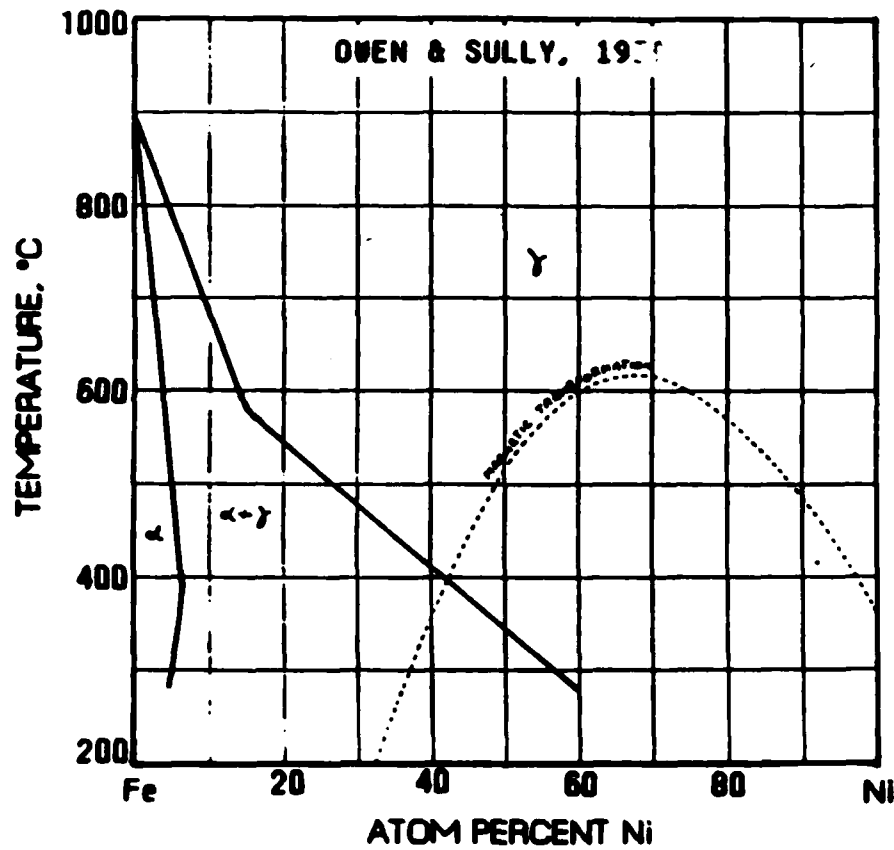


Figure 2.3 - Proposed Fe-Ni phase diagram based on an x-ray diffraction study of aged specimens (27).

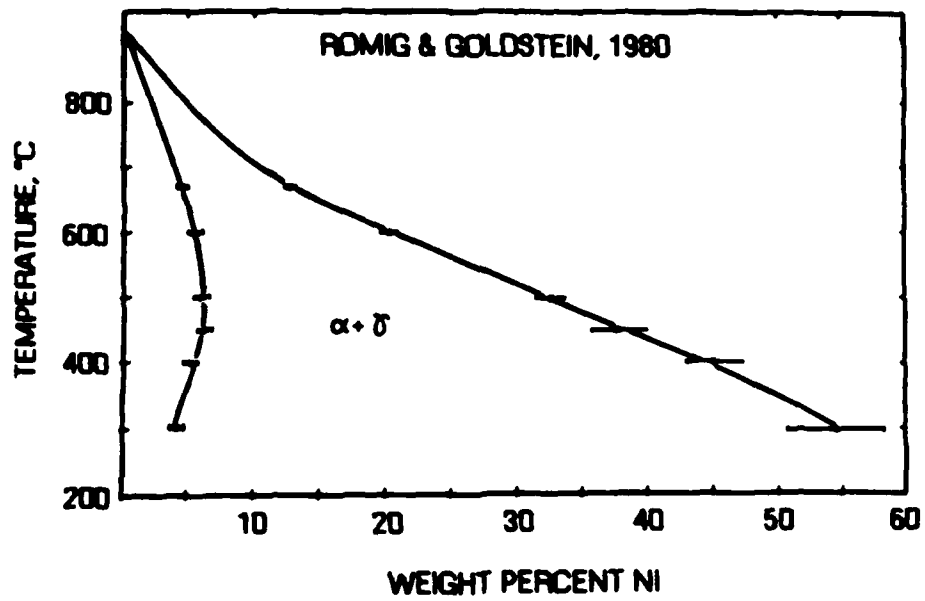


Figure 2.4 - Proposed Fe-Ni phase diagram based on analytical electron microscopy of aged specimens (30).

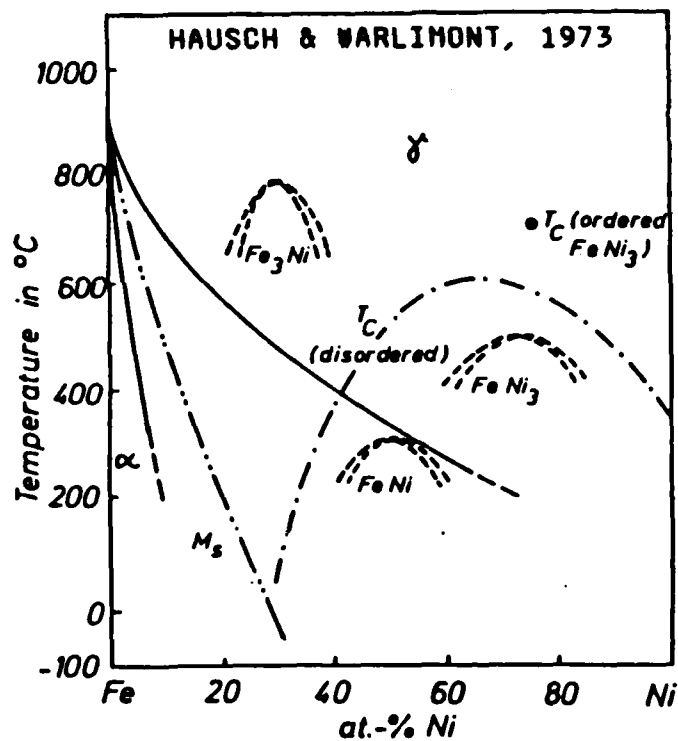


Figure 2.5 - Proposed Fe-Ni phase diagram (33).

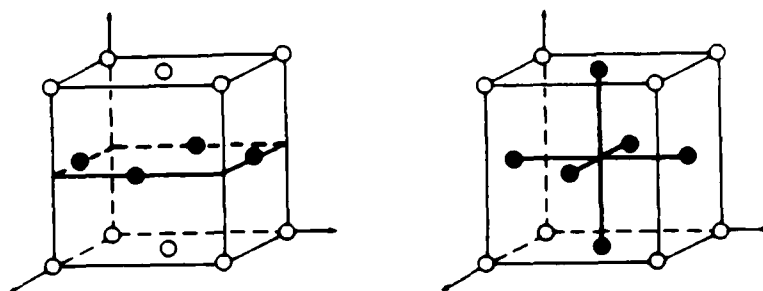


Figure 2.6 - Crystal structures of the ordered phases (a) $FeNi$ ($L1_0$) and (b) Fe_3Ni and $FeNi_3$ ($L1_2$).

the Fe_2NiO_4 spinel in aged TEM foils containing 24 to 34 wt% Ni, and suggested that this phase accounts for what had been attributed to ordering at Fe-25Ni.

Heumann and Karsten (35) studied foils which had been prepared amorphous by co-deposition of Fe and Ni from vapors, then crystallized by annealing. They proposed the diagram shown in Figure 2.7 in which γ decomposes into α plus FeNi_3 at 345°C on cooling. Existence of the FeNi_3 phase had been reported as early as 1932 by other German workers (36), but apparently was not found in the previously mentioned studies by Owen and co-workers. Hansen and Anderko (37) cited twelve other works in which FeNi_3 was detected by x-ray diffraction, dilatometry, and resistivity, magnetization, and specific-heat measurement. More recently, ordering to FeNi_3 in synthetic alloys has been studied using Mossbauer spectroscopy (38).

Irradiation Studies

Irradiation of Fe-Ni alloys at the temperatures of interest with neutrons or electrons has been used to speed the approach to equilibrium. The usually implicit assumption is that the radiation produces cascades and vacancies which enhance diffusion and relax lattice stresses due to phase transformations, but that it does not induce transformations. This assumption seems reasonable for the case of an ordered phase forming under irradiation in alloys that show comparable levels of Ni segregation in the absence of radiation.

Pauleve et al. (39) irradiated Fe-50Ni specimens with fast (>1 Mev) neutrons in a magnetic field. Ordering to FeNi occurred with the c-axis preferentially aligned with the imposed magnetic field. Although this phase has tetragonal symmetry, the unit cell was reported to be nearly cubic; $|c-a|/a < 5 \times 10^{-4}$. The critical temperature of the ordering reaction was established as $320 \pm 2^\circ\text{C}$ by resistivity measurements.

Chamberod, Laugier, and Penisson (40) irradiated alloys containing 28 to 50 wt% Ni with 2-MeV electrons, then analyzed them using Mossbauer spectroscopy, x-ray and electron diffraction, and magnetization measurements. They found that (1) the coefficient of thermal expansion of an Fe-35Ni alloy increased from $\approx 10^{-6}$ to $\approx 10^{-5}$ per $^\circ\text{C}$ upon irradiation (i.e., the Invar alloy lost its characteristic feature) and (2) initially homogeneous material decomposed into the ferromagnetic, ordered, FeNi phase and a paramagnetic, Ni-lean, "fcc" phase with the same lattice

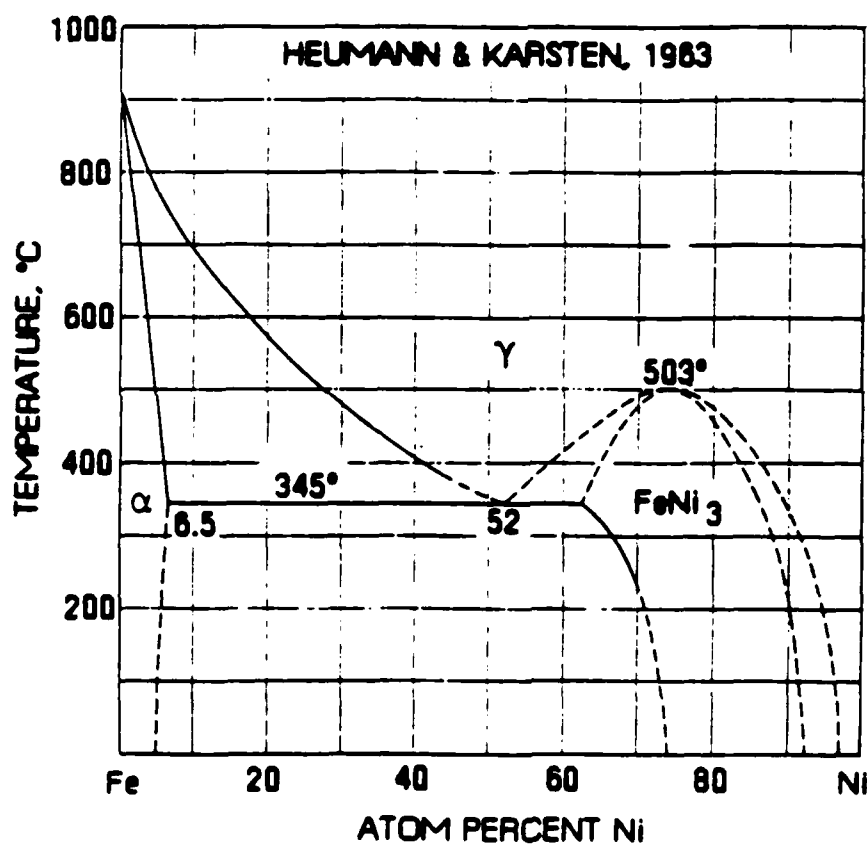


Figure 2.7 - Proposed Fe-Ni phase diagram based on an x-ray diffraction study of vapor-deposited-and-annealed specimens (35).

parameter. The paramagnetic phase formed in an Fe-30Ni specimen under irradiation did not transform to martensite when cooled to -269°C . They suggested that paramagnetic phase was stable because either (1) it was present as very small grains which are known to have a reduced M_s or (2) it had ordered to Fe_3Ni . Their proposed diagram is shown in Figure 2.8.

Gruzin, Rodionov, and Pryakhim (41) also irradiated specimens with high-energy (3-5 MeV) electrons and studied them using Mossbauer spectroscopy. They concluded that γ decomposes into ferromagnetic FeNi plus paramagnetic disordered γ containing ≈ 26 wt% Ni, and placed the critical temperature for ordering to FeNi at $\approx 400^{\circ}\text{C}$.

Silvestre et al. (42) irradiated Fe-Ni specimens with fast neutrons at temperatures between 400 and 600°C . For irradiation temperatures up to 500°C , ordering to FeNi_3 occurred in an alloy containing 75 wt% Ni, and precipitation of FeNi_3 occurred in alloys containing 41 to 61 wt% Ni. Ordering did not occur at irradiation temperatures above 500°C .

Iron Meteorites

The average iron meteorite contains 90 wt% Fe, 8 Ni, 0.7 S, 0.5 Co, 0.2 P, 0.04 C, 0.015 Cu, 0.015 Ge and several ppm of about twenty other elements (43). These meteorites are thought to have cooled at a rate of about 1°C per million years (43), and therefore are often assumed to exhibit at least local phase equilibrium. Results of meteorite studies are sometimes used to construct new Fe-Ni phase diagrams, or compared with existing diagrams to determine the meteorite's thermomechanical history.

The coarse structure of iron meteorites is plates of Widmanstätten α containing less than 7.5 wt% Ni in a relatively Ni-rich "matrix" (44). The Ni content of the "matrix" varies from ≈ 50 wt% adjacent to the α plates down to ≈ 10 wt% farther away. This "matrix" is actually a fine-scale mixture of varying proportions of phases with different Ni contents rather than a single phase with a concentration gradient. The phases reported to be present in the "matrix" include α , α_2 (martensite), γ , and FeNi.

Lin, Goldstein, and Williams (44) used electron column instruments to study the Carlton meteorite (13.4 wt% Ni). They concluded that the "matrix" phases are retained γ , α precipitated from γ , and α plus γ formed from the

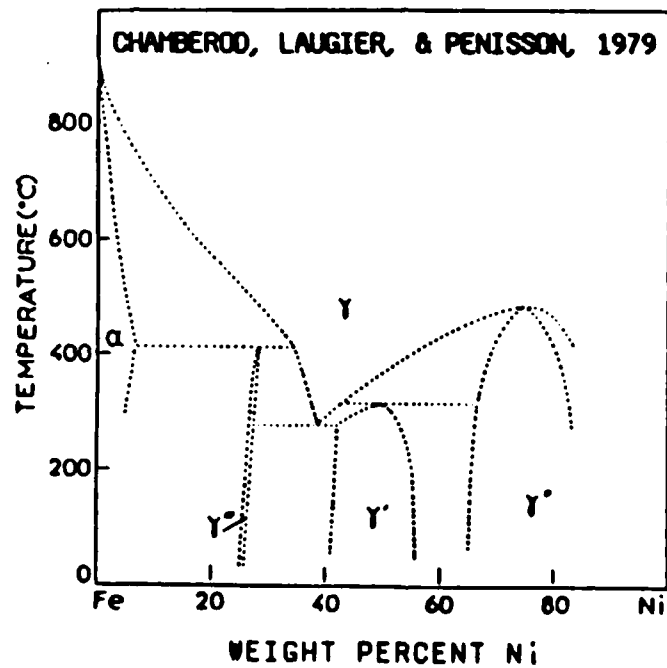


Figure 2.8 - Proposed Fe-Ni phase diagram based on magnetization and x-ray diffraction studies, electron microscopy, and Mossbauer spectroscopy of electron-irradiated specimens (40).

decomposition of α_2 . In the region containing ≈ 20 wt% Ni, the γ rods formed from α_2 were 10 to 30 nm wide. In the region containing ≈ 11 wt% Ni, they were 30-200 nm wide, contained less than 44 wt% Ni, and were conjugated with α containing as little as 3 wt% Ni. Based on the low Ni content of the α , the authors concluded that equilibrium was maintained down to $\approx 200^\circ\text{C}$. Faint superlattice spots were found on electron diffraction patterns at positions corresponding to 100α reflections but were not investigated further.

Other studies have detected the FeNi phase in at least forty iron meteorites by polarized-light microscopy (45,46), x-ray diffraction (47-49), electron diffraction (46,50,54,55), and Mossbauer spectroscopy (39-54). Two of the resulting Fe-Ni phase diagrams are shown in Figures 2.9 and 2.10.

Albertsen, Nielsen, and Buchwald (54) studied iron meteorites by x-ray diffraction, electron microscopy, and Mossbauer spectroscopy, and accounted for some of the structure found between the Widmanstätten α plates as follows. The "cloudy zone" (≈ 30 -40 wt% Ni) forms in two steps. First, the strong dependence of Curie temperature on Ni content in the 30-40 wt% Ni range leads to a magnetically induced spinodal decomposition of the γ into magnetically and atomically ordered FeNi (>41 wt% Ni) plus magnetically and atomically disordered γ (<25 wt% Ni). On further cooling, paramagnetic disordered antiphase boundaries (APBs) (<25 wt% Ni) form in the relatively Ni-rich phase as the solubility of Fe in FeNi decreases. The "outer clear zone" (≈ 40 -50 wt% Ni) does not undergo the magnetically induced transformation, but does order and form the paramagnetic disordered APBs.

The paramagnetic fcc Fe- ≈ 25 Ni phase formed in meteorites (54) and in irradiated specimens (40) does not transform to martensite when cooled to -269°C even though the reported M_s temperature of an Fe-25Ni alloy is $\approx 90^\circ\text{C}$ (22). Albertsen et al. (53) suggested that this Ni-lean γ is stabilized by the FeNi which has the same lattice parameter (0.3582 nm) and shares the same crystallographic axes. They go on to say that "if the interface contribution to the free energy could be neglected, the true equilibrium state below 320°C would be α -phase in equilibrium with ordered FeNi with about 50% Ni", as shown in Figure 2.10. The presence of α (≈ 16 wt% Ni) in the Estherville meteorite (55), which is thought to have cooled slower than others, may corroborate the proposed α plus FeNi equilibrium.

Bowles, Hatherly, and Malin (56) proposed a corrosion-based mechanism for the formation of FeNi in the Santa

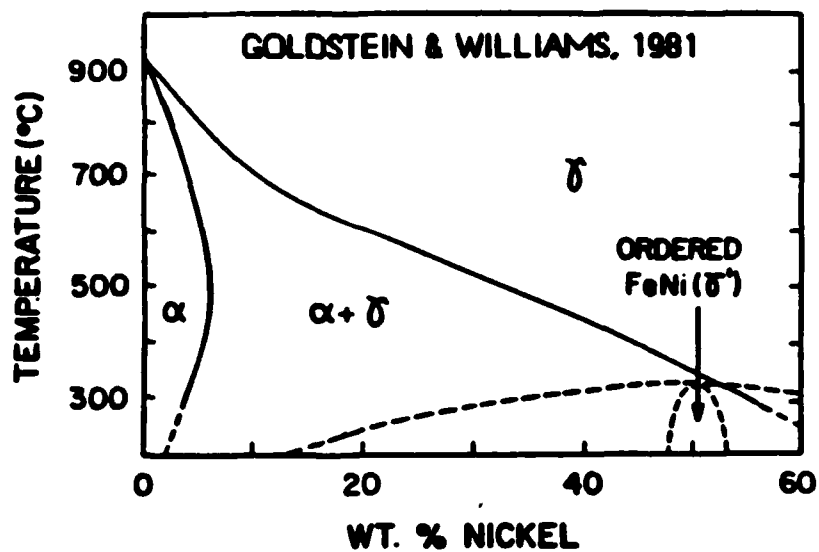


Figure 2.9 - Proposed Fe-Ni phase diagram based on electron microscopy of iron meteorites (and aged specimens ?) (50).

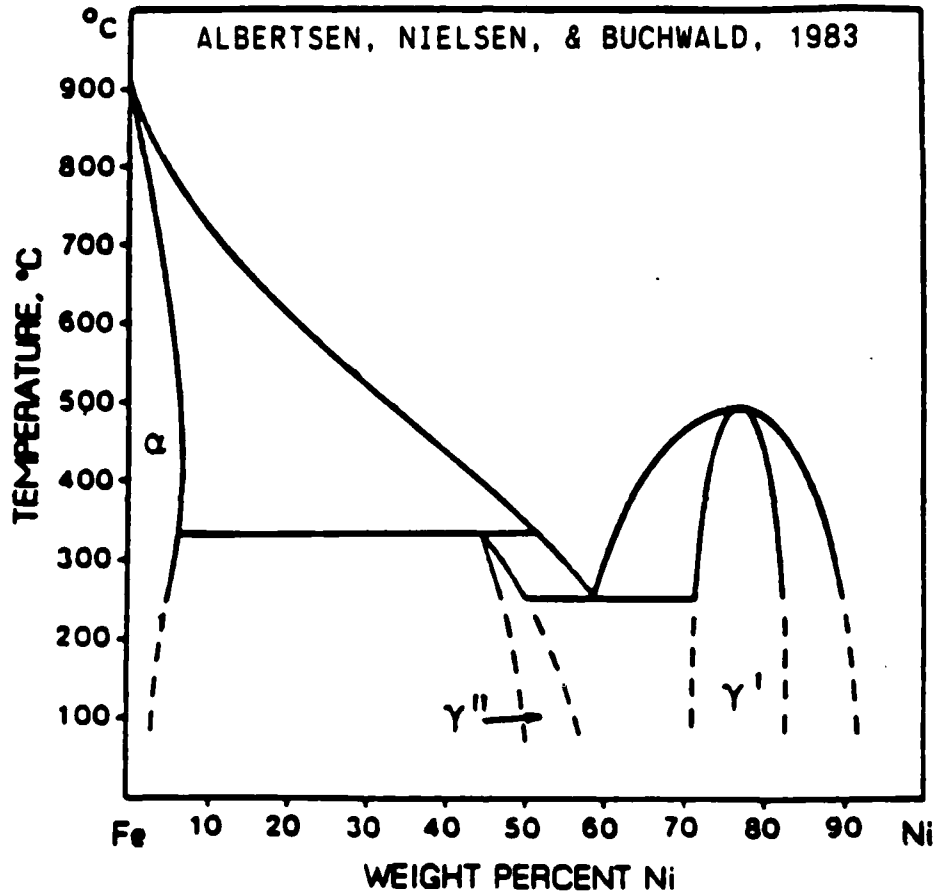


Figure 2.10 - Proposed Fe-Ni phase diagram based on electron microscopy, electron microprobe studies, and Mossbauer spectroscopy of iron meteorites (54).

Catharina meteorite (35 wt% Ni). They reported that preferential corrosion of Fe produces near-surface divacancies which accelerate diffusion enough to allow the formation of FeNi in as little as 5 days at RT.

Terrestrial Native Metal

Alloys of iron and nickel are also found as terrestrial deposits. The native metal constitutes ~90% of the josephinite rock found in southwest Oregon, and contains about 68 wt% Ni, 29 Fe, 0.56 Cu, 0.26 As, 0.26 Co, and 0.04 Si (57). Botto and Morrison (57) studied the metal fraction with the electron microprobe and reported the structure to be γ (61-68 wt% Ni) plus FeNi₃ (72-75 wt% Ni).

Danon et al. (58) studied the metal fraction by Mossbauer spectroscopy and concluded that the relatively Ni-lean phase is FeNi.

Volume Fraction Phase Analysis

Knowledge of the volume fraction of one or more phases in a multi-phase material is often desired in both production and research operations. In the former, the amount of one phase, such as retained austenite in martensitic steels, may have to be controlled because of its influence (either positive or negative) on the material behavior during processing or in service (59). In the latter, volume fraction phase analysis may be used to monitor the extent of phase transformations due to thermal, mechanical, or radiative treatments. The remainder of this section specifically addresses the measurement of austenite content in steels, but most of the concepts are generally applicable.

Numerous techniques have been used to determine the amount of austenite in steels, including quantitative metallography with optical or electron micrographs, x-ray diffraction, Mossbauer spectroscopy, thermal analysis, dilatometry, and measurement of electrical resistivity, magnetic permeability, or density. Each of these techniques has limitations or complications due to the long time or tedium of analysis, specimen size, shape, or finish requirements, size or shape of grains, etching behavior, additional phases such as carbides, phase transformations during specimen preparation, crystallographic texture, magnetic texture, need for standards, and lack of knowledge of the composition, structure, and properties of the individual phases present. Quantitative metallography with

optical micrographs and x-ray diffraction are the most commonly used techniques for austenite-content determination. Three techniques are discussed below.

Quantitative Metallography

Quantitative metallography (60) with optical or electron micrographs is probably the most straightforward technique for volume fraction phase analysis. The primary requirement is that micrographs be prepared such that the different phases are readily identifiable. The actual analysis may be done by tedious manual methods, such as point counting, or by automatic image analyzers. This technique is popular because (1) no calibration standards are needed, (2) many combinations of thermal treatment, etching procedure, and illumination are available for imaging different phases or different orientations of a single phase, and (3) the type of specimen required may also be used for other metallographic work. Accurate austenite-content measurement by quantitative metallography is difficult for amounts below 10-15 vol%. Even when present in greater amounts, measurement may be difficult if the austenite is present as thin films or small grains, or has the same morphology as the martensite (61). Since this technique samples only the surface of the specimen, care should be taken to avoid inducing phase transformations during specimen preparation. As noted by Eldis (62) however, if such transformations are unavoidable, this technique may be more accurate than other surface-sensitive techniques provided that the investigator knows the parent phase of the transformation and can identify regions of the product phase in the specimen. His particular work dealt with untempered martensite formed from austenite in a tempered martensitic steel during specimen preparation.

X-Ray Diffraction

Volume fraction phase analysis by x-ray diffraction involves collecting a diffraction pattern from a suitably prepared specimen, then comparing the intensities of several peaks with one another or with those from a reference material (63). In calculating the amount of a phase present in a specimen, it is usually assumed that (1) the intensity of a peak is proportional to the irradiated volume of the associated phase, (2) the volume fraction of each phase in the irradiated volume is the same as that in the bulk of the specimen, and (3) peak broadening due to small grain size and nonuniform microstrain does not affect the relative peak intensities. The commonly used techniques are of the direct comparison type, in which the intensity of one or more

austenite peaks is compared with that of one or more martensite peaks. The ratio of volume fractions of two phases is taken to be proportional to the ratio of peak intensities. The techniques differ primarily in choice of radiation and peaks, specimen motion, and determination of proportionality constants (59). Time required for one analysis ranges from ≈ 24 hr for Averbach and Cohen's (64) camera technique down to ≈ 20 sec for Cohen and James' (65) position-sensitive-detector technique.

Camera Technique

Early retained austenite measurements were made using microphotometer traces of films exposed in x-ray diffraction cameras. Sekito (66) attached a strip of Au foil to each cylindrical steel specimen, then collected a pattern from the rotating composite specimen. The height of the 200 austenite peak was measured relative to that of the 111 Au peak on the same trace. This relative peak height was then divided by that from an austenitic Mn steel to obtain the volume fraction of austenite.

Averbach and Cohen (64) also used microphotometer traces, but they worked with peak areas rather than peak heights. In this direct comparison technique, measured peak areas were adjusted to account for multiplicity, structure, polarization, temperature, and absorption factors, then austenite peak areas were compared with martensite peak areas to obtain the volume fraction of austenite. With monochromated Co K α radiation and a 24 hr exposure time, the accuracy and minimum detectability limit were reported as $\pm 5\%$ of the amount of austenite present and 0.5 vol% austenite, respectively. The necessary exposure time was later reduced by a factor of six to eight by the use of a focussing rock salt monochromator instead of a flat one (67). Beu (68) improved the accuracy and reduced the calculation time by calculating an absorption factor for each peak rather than using the graphical method of Averbach and Cohen. He also reported that the exposure time could be reduced by a factor of two to five if quartz was used instead of rock salt for the monochromator.

Diffraction Technique

Dietche (69) and Miller (61) developed a relatively fast (less than 1 hr per specimen) technique that employs a diffractometer, Mo K α radiation, a flat metallographic specimen, and an empirically determined proportionality constant. This direct comparison technique involves measuring the areas under the 220 and 311 austenite peaks and the 211 martensite peak, then calculating the volume

fraction of austenite using equation 3.2 on page 44. The use of two austenite peaks (rather than one) reduces the effect of preferred crystallographic orientation on the analysis. Also, a large difference in the areas under the austenite peaks indicates that a strong preferred orientation is present, and that a different specimen and/or technique should be used. The accuracy and minimum detectability limit of this technique were reported as $\pm 5\%$ of the amount of austenite present and 2 vol% austenite, respectively. Dietche noted that "due to the proximity of the atomic scattering factors of the principal elements in alloy steels and the displacement of the wavelength of the characteristic molybdenum ($K\alpha$) x-radiation from the absorption edges of these elements", chemical composition has little effect on the intensity of diffraction. Therefore, it appears to be unnecessary to calculate a proportionality constant for each steel examined.

Preferred Orientation

The primary sources of error in x-ray diffraction volume fraction phase analysis are preferred crystallographic orientation and large grain size of the specimen. Both conditions may cause peak intensities (heights or areas) to be much greater or much smaller than those from a randomly oriented fine-grained specimen. As a result the apparent austenite content of a specimen having preferred orientation and/or coarse grains will vary with the plane of section and the orientation of the specimen relative to the incident x-ray beam.

To minimize the error due to preferred orientation, investigators have (1) rotated and tilted the specimen while collecting a pattern, (2) calculated an average peak intensity for each peak to be used in the austenite analysis based on the corresponding pole figure (70,71), (3) used five or more peaks per phase in the analysis (72), and (4) used knowledge of the phase orientation relationship (ex. Kurdjumov-Sachs) in a specimen to determine the proportionality constant in the volume-fraction austenite calculation (73). Work done with rotating-and-tilting specimens is discussed below.

Miller (74) described a specimen holder that rotates a flat metallographic specimen about its normal and asynchronously tilts it $\pm 56^\circ$ about an axis perpendicular to both the rotation and diffractometer axes. Using this holder, a horizontal incident-beam slit, and a vertical diffracted-beam slit on a vertical-axis diffractometer, he obtained consistent accurate results from three orthogonal faces of a specimen having preferred orientation due to rolling. Since a vertical diffracted-beam slit was used

(presumably to maintain 2θ angular resolution), a narrow, horizontal, incident-beam slit was used to minimize the effect of defocussing due to tilting on the diffracted-beam intensity (75,76). Miller noted that the accompanying reduction in incident-beam intensity increased the minimum detectability limit to 5 vol% austenite. Kim (77) successfully applied Miller's rotating-and-tilting technique to cast irons having "very coarse microstructures, with grain diameters 1 to 5 mm and very strong preferred orientation". Fillit et al. (78) modified the technique by (1) increasing the tilt range to $\pm 60^\circ$ and (2) using a computer to control the specimen rotation, specimen tilt, and 2θ -scan motions. They determined correction factors to account for defocussing and absorption at each 2θ of interest by measuring the intensity of a beam diffracted from a randomly oriented fine-grained specimen as a function of tilt angle. Their technique reportedly can be used "... to make absolute (austenite content) measurements, regardless of the texture." It is interesting to note here that Schulz (75) apparently eliminated the need for defocus and absorption corrections (in pole-figure work) for tilt angles up to 75° by using horizontal slits on a vertical-axis diffractometer.

Specimen Preparation

Commonly used metallographic specimen-preparation techniques may cause phase transformations in material near the specimen surface. These induced transformations may then lead to erroneous austenite-content measurements if (1) a surface-sensitive technique such as Mo K α x-ray diffraction (sampling depth of $\approx 10 \mu\text{m}$) is used and (2) the austenite content in the bulk of the specimen is assumed equal to that of the surface.

Near-surface phase transformations during specimen preparation are due to (1) the metastable nature of the austenite and martensite, (2) heating and deformation, and (3) release of mechanical constraint as material in the bulk is exposed by sectioning, polishing, etc.

Eldis (62) reported that the austenite content determined by x-ray diffraction was ≈ 5 vol% lower than that determined by quantitative optical metallography of high-carbon regions (20-40% austenite) of carburized-and-tempered steels. He explained that the x-ray technique could not distinguish between the surface martensite formed during specimen preparation and the tempered martensite formed earlier. Careful optical metallography could make the distinction, thereby allowing the surface martensite to be properly counted as austenite.

Beu and Koistinen (79) studied the effects of surface preparation techniques, including sanding, polishing, etching, and electrolytic dissolution, on the austenite content of hardened carbon steels as measured by x-ray diffraction. Whereas fast dry sanding increased the surface austenite content of a 12 vol% austenite steel by 6 vol% (i.e. from 12 to 18), the other techniques reduced the surface austenite content of 5-27 vol% austenite steels by up to 4.5 vol%. The conventional sequence of wet-sanding, polishing, and etching caused a reduction of 1.5 vol% or less. Electrolytic dissolution caused no change. Austenite-content reductions were attributed to the austenite-to-martensite decomposition induced by heating and/or tensile loading in the near-surface region during wet sanding, slow dry sanding, and polishing. Increases were attributed to re-austenitization during fast dry sanding, followed by partial decomposition to martensite. Earlier they reported that, for their camera technique, variation in specimen surface roughness from 3 to 250 microinches and variation in surface curvature from 21.0 mm convex radius to 6.4 mm concave radius had no effect on retained austenite measurements.

In summary, the primary effect of specimen preparation on austenite-content measurements made by x-ray diffraction is due to induced phase transformations. Specifically, the induced austenite-to-martensite decomposition may cause an error of ≈ 5 vol%.

Mossbauer Spectroscopy

Volume fraction phase analysis by Mossbauer spectroscopy is similar to the x-ray diffraction technique in that first a spectrum is collected, then peak areas are compared, with or without the use of correction factors. Since (1) the form of the Fe-57 Mossbauer spectrum is determined directly by the electromagnetic environment of the Fe-57 nuclei and only indirectly by crystal structure and (2) the area of each peak is proportional to the irradiated volume, Fe-57 content, and recoilless fraction in the associated phase, some knowledge of the hyperfine parameters, chemical compositions, and lattice parameters of the phases present is required for the analysis. Data collection usually takes several hours and data analysis (spectrum deconvolution) often requires a computer. The positive features of the Mossbauer technique are (1) its ability to examine surface layers or foils of ≈ 0.1 to $\approx 100 \mu\text{m}$ thickness and (2) its reported insensitivity to preferred crystallographic orientation and grain size (80).

Austenite-content measurement by Fe-57 Mossbauer spectroscopy has been done using both the transmitted and

the backscattered radiations. Balestrino and Cavallini (81) measured the retained paramagnetic-austenite content of 50- μm foils of ferromagnetic SAE 4340 steels using the transmitted 14.4-keV gamma rays. In calculating phase volume fractions they corrected the spectra for specimen-thickness effects, assumed equal recoilless fractions and Fe-57 contents in the austenite and martensite, and used known values of the lattice parameters.

Schwartz and Kim (82) measured the paramagnetic-austenite content at the surface of ferromagnetic AISI 1095 steel specimens using both the backscattered 6.4 keV x-rays and the backscattered 5.4- and 7.2-keV electrons. They too assumed equal recoilless fractions and iron contents in the phases present. For an oil-quenched specimen, the austenite content of the ≈ 25 μm thick surface region was found by Mossbauer x-ray spectroscopy to be 28% whereas that of the ≈ 0.3 μm surface region was found by Mossbauer electron spectroscopy to be only 16%. Since similar values were measured for a surface created by electropolishing off 1.0 mm of material, the 12% discrepancy was considered not to be due to local differences in M_s or cooling rate.

Techniques that utilize the Mossbauer effect, but not conventional Mossbauer spectroscopy, have been developed for phase-content measurement. Huggins and Huffman (83) described a method that requires only a few minutes per specimen because data are collected in just two velocity ranges rather than the conventional 512 ranges. The ranges are chosen such that, in one, resonant absorption by the phase of interest is occurring most of the time, and in the other, non-resonant absorption is occurring most of the time. The measured resonant absorption is normalized (divided) by the non-resonant absorption and multiplied by an experimentally determined proportionality constant to determine how much of the phase of interest is present. This technique works best when (1) the peak from the phase of interest is isolated from other peaks and (2) the peak occurs near 0 mm/s source velocity. The use of stainless steel as a source matrix was recommended for austenite-content measurement. A technique requiring a calibration curve and knowledge of the areal density of the absorber that was developed by the same investigators (84) for work with coal might be adapted for austenite-content measurement.

Accurate volume fraction phase analysis by Mossbauer effect techniques of slowly cooled or aged steels may be difficult, especially if there is a preferred crystallographic orientation or the grains are large. First, diffusion will change the Fe-57 contents of the phases, thereby requiring the use of composition-dependent constants in the calculations. Second, phases formed during

aging may complicate the deconvolution process by adding peaks to the spectrum. Examples include ferromagnetic iron carbide formed in SAE 4340 steel (81) and ferromagnetic austenite formed in Fe-30Ni alloys (this work). In both cases the six-line subspectrum of the new phase at least partially overlaps that of the parent martensite. Finally, since the relative intensities of the peaks in a six-line spectrum depend on the angle between the local axis of magnetization and the incident gamma-ray beam, the subspectrum may be altered by preferred magnetic orientations, further complicating the deconvolution. It seems therefore that if the axes of magnetization in a specimen do lie along the crystallographic directions of easy magnetization, then a preferred crystallographic orientation or large grain size will affect the Mossbauer spectrum. Also, Stevens and Preston (85) noted that, due to spontaneous magnetization of thin iron foils, the ideal intensity ratios of 3:2:1:1:2:3 for peaks in the magnetically split six-line subspectrum are rarely observed.

X-Ray Microanalysis

Microanalysis by x-ray spectrometry in electron column instruments is a technique for in-situ determination of the chemical composition of microscopic volumes in suitably prepared specimens. Microanalysis of electron-transparent specimens by energy-dispersive x-ray spectrometry (EDS) in the scanning transmission electron microscope (STEM) is discussed qualitatively in this section. Detailed quantitative discussions may be found in the works by Williams (86), Goldstein (87), and Zaluzec (88).

Microanalysis

Electron irradiation of specimens in the STEM produces x-rays having energies characteristic of the elements present. X-ray microanalysis is based on the fact that the generated intensity of any characteristic x-radiation (ex. Fe K α) is proportional to the number of atoms of the associated element in the irradiated volume. If the generated intensities could be measured, analysis of specimens for all elements would be very simple. Unfortunately, due to absorption and fluorescence effects in the specimen and in the EDS detector, the detected intensities may be quite different from the generated intensities. Absorption of the characteristic x-rays from elements lighter than C is usually strong enough to prevent their detection.

Thin specimens are often analyzed for elements heavier than C by using the Cliff-Lorimer (89) equation:

$$\frac{C_A}{C_B} = k_{AB} \frac{I_A}{I_B} \quad (2.1)$$

where C_A and C_B are the concentrations of elements A and B in the volume analyzed, I_A and I_B are the simultaneously measured intensities of selected characteristic x-radiations (ex. A K α and B K α), and k_{AB} is a constant whose value depends on the selected characteristic x-radiations, the microscope and detector geometries, and the microscope operating conditions. Although accurate values of k_{AB} have been calculated from first principles for certain microscopes and pairs of elements (87,90), it seems safer to determine the values empirically.

Equation 2.1 is rigorously correct only if the region of the specimen being analyzed is of infinitesimal thickness (and even then only if k_{AB} was determined using a standard of infinitesimal thickness). In thicker regions, due to absorption and fluorescence effects, I_A/I_B will vary with thickness. It is common practice to choose a tolerable error in the analysis, calculate the specimen thickness that would produce the tolerable error, then analyze only those regions that are thinner than the calculated critical thickness. Specimens thinner than the critical thickness are said to satisfy a "thin-film criterion", several of which have been proposed in the literature (91-93). Romig (94) used a thin-film criterion that allows for a 10% error due to absorption in I_A/I_B to calculate the critical thickness for a number of Fe-Ni alloys. For a 36° take-off angle, the results ranged from 235 nm for an Fe-2Ni alloy to 490 nm for an Fe-50Ni alloy. Since foils of these alloys are transparent to 100-keV electrons only if they are less than \approx 200 nm thick, electron-transparent foils are suitable for x-ray microanalysis.

Spurious X-Rays

Even though the incident electron beam is focussed to a \approx 10 nm diameter spot on the specimen, due to scattering of electrons and x-rays, characteristic x-rays generated 0.5 mm or farther from the beam spot may enter the detector.

First, electrons in the incident beam are scattered as they pass through the specimen. For 100-keV electrons passing through ≈ 150 -nm thick foils of ferrous materials, scattering is reported to be ≈ 15 nm (87). In other words, a 20 nm diameter incident beam gets spread to ≈ 50 nm diameter before exiting the specimen. Incident electrons may also be scattered by the cone of C contamination before entering the specimen.

Second, stray electrons and x-rays generated in the upper column may strike remote regions of the specimen, the specimen holder, and other components and generate characteristic x-rays. Allard and Blake (95) documented this phenomenon, then installed thick apertures and a detector collimator in the University of Michigan's JEOL 100CX TEM/STEM to eliminate this cause of spurious x-rays.

Finally, electrons and x-rays scattered from the specimen may generate characteristic x-rays in remote regions of the specimen and nearby components. Four possibilities are shown in Figure 2.11. Allard and Blake (95) replaced some specimen-chamber components with similar ones made of C or Al and covered others with Be foil to eliminate this cause of spurious x-rays. They reported that the effects of specimen self fluorescence (Figure 2.11d) can be avoided only by analyzing crushed grains, extracted particles, or uniformly thin films. Romig (90) reported that these effects can be minimized by working on the half of the foil that is rotated below the tilt axis. Williams (86) noted another possible cause of spurious x-rays; electrons backscattered from the specimen will follow a spiral path due to the objective lens field. This path may cause the electron to strike a remote region of the specimen or nearby components.

Specimen-preparation artifacts may cause errors in microanalysis. Williams (86) reported examples of X-rich surface layers formed on thin foils of Al-X alloys during preparation by electropolishing or ion thinning, where X is Cu, Zn, or Ag. In one case, surface layer contamination was found to be a problem only when the electrolyte had been used several times. Lorimer reportedly (86) said that "... in most steels, a routine dusting in the ion thinner is all that is required" to remove surface layers. Others reportedly (86) concluded that the cleaning of specimens by sputtering in an ultra-high vacuum is the only way to eliminate the effect of surface layers.

Mossbauer Spectroscopy

Rudolph Mossbauer discovered the effect that now bears

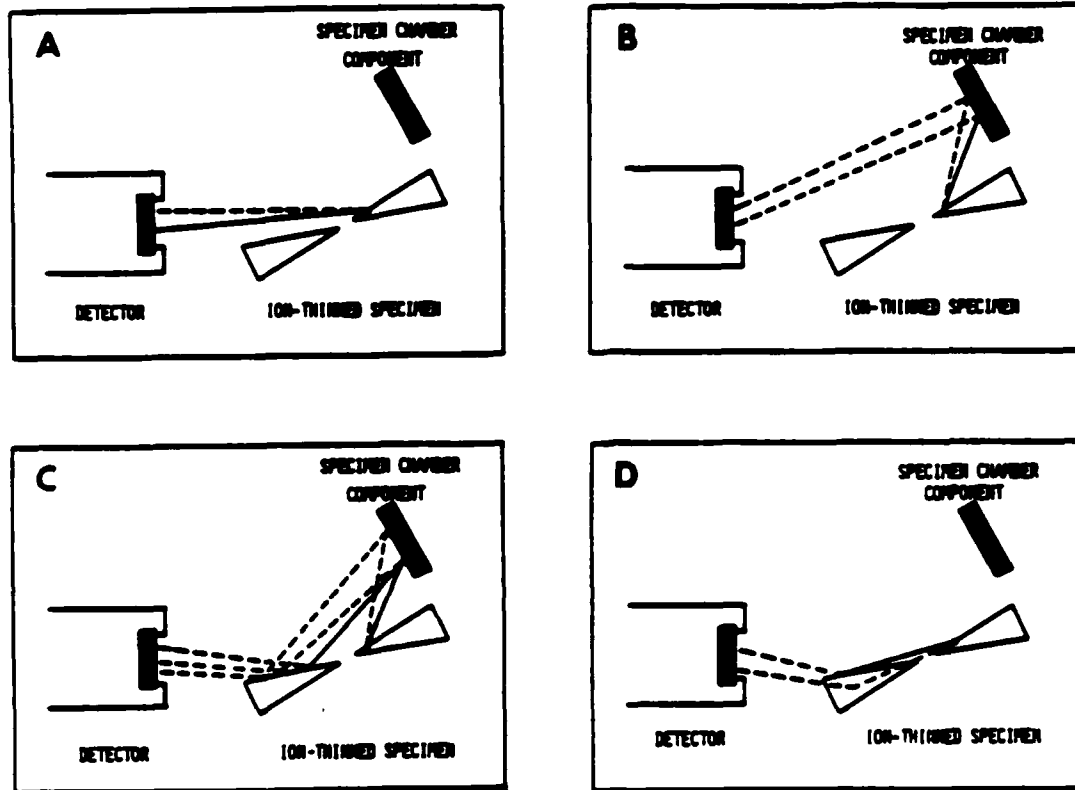


Figure 2.11 - Possible sources of spectral contamination generated in the specimen chamber by x-rays (dashes) and electrons (solid lines) from the specimen. (a) characteristic and continuum x-rays from the point of analysis, as well as backscattered electrons; (b) sample-generated radiation fluoresces x-rays from chamber components; (c) sample-generated x-rays and electrons interact with chamber components to produce x-rays and electrons, which in turn fluoresce bulk areas of the specimen away from the point of analysis; (d) sample-generated x-rays and electrons fluoresce bulk areas of specimen away from the point of analysis (94).

his name during his graduate studies in 1957 (96). Since then the effect has been observed in at least eighty isotopes of forty-three elements (97). Several spectroscopies which exploit the effect have been developed and used extensively to study materials containing Fe-57 or Sn-119 (97-101). Mossbauer effect, Mossbauer spectroscopy, and their applications in ferrous metallurgy are discussed in this section.

Mossbauer Effect

"Mossbauer effect" refers to the emission or absorption of a γ -ray during a nuclear transition in which the energy of the γ -ray is equal to the energy difference between the excited and ground states of the nucleus. This effect can occur only if the nucleus is bound as in a solid or some liquids.

Consider first an unbound nucleus which can undergo a transition between two energy levels that differ by an amount E_0 , emitting a γ -ray with energy $E_{\gamma e}$. See Fig 2.12a. (For the Fe-57 14.4 keV transition, the "linewidth" or scatter in E_0 , shown as Γ in Figure 2.12a, is actually fourteen orders of magnitude smaller than E_0 .) Conservation of momentum requires that the nucleus recoils in the direction opposite that of the γ -ray with a velocity v_r such that

$$m_r v_r = E_{\gamma e} / c \quad , \quad (2.2)$$

where c is the speed of light and m_r is the mass of the nucleus. The recoiling nucleus thus acquires a kinetic energy

$$E_r = m_r v_r^2 / 2 \quad , \quad (2.3)$$

limiting the energy of the γ -ray to

$$E_{\gamma e} = E_0 - m_r v_r^2 / 2 \quad . \quad (2.4)$$

Similarly, the energy required of a γ -ray incident on an

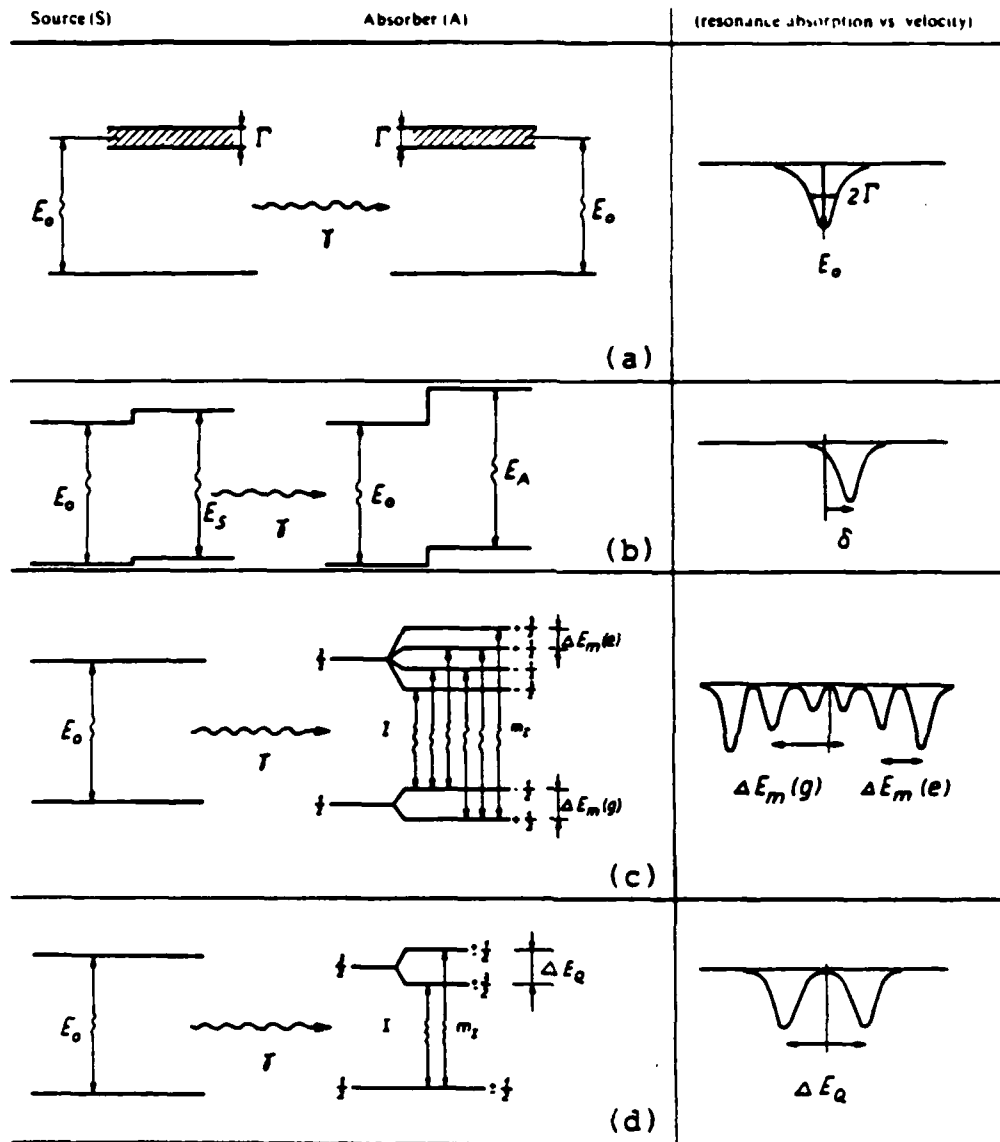


Figure 2.12 - Energy-level diagrams and γ -ray transmission spectra for nuclear transitions illustrating (a) resonant absorption for the case of source and absorber nuclei in identical environments, (b) isomer shift, (c) magnetic dipole splitting, and (d) electric quadrupole splitting.

unbound nucleus to effect a transition of energy E_0 is

$$E_{\gamma a} = E_0 + m_r v_r^2 / 2 \quad . \quad (2.5)$$

Now consider an emitting nucleus which is bound in a crystal lattice. Conservation of momentum requires that either the crystal or the nucleus recoils. If the crystal recoils as a rigid structure, the recoil mass m_r in equation 2.2 is large, v_r is small, E_r is small, and $E_{\gamma e} = E_0$. For the Fe-57 14.4 keV transition and a crystal containing only $\approx 10^6$ atoms, $E_0 - E_{\gamma e} = \Gamma$, the inherent scatter in E_0 .

If the nucleus recoils, it must either leave its lattice site with velocity v_r or remain on its lattice site and excite lattice vibrations. Displacement of the nucleus is not possible because, as shown in Table 2.2, the atomic binding energy is much greater than the recoil energy. Since both the γ -ray emission and the lattice vibrations are quantum mechanical events, a fraction of the γ -rays are emitted without causing lattice vibrations. These γ -rays have an energy $E_{\gamma e} = E_0$. Similarly, a fraction of the γ -rays with energy E_0 incident on a bound nucleus will excite the nucleus without causing lattice vibrations. The recoilless fraction of the Fe-57 14.4 keV transition for Fe in various host materials is 0.78 for Rh, 0.72 for Pt, and 0.66 for Pd.

Table 2.2 - Energies Associated with the
Fe-57 14.4 keV Transition.

<u>Item</u>	<u>Symbol</u>	<u>Energy, J (eV)</u>	
Recoilless γ -ray	E_γ	2.3×10^{-15}	(14.4×10^3)
Atomic binding	E_b	4.8×10^{-18}	(3.0×10^1)
Free-nucleus recoil	E_r	3.1×10^{-22}	(2.0×10^{-3})
Hyperfine interactions	E_h	3.8×10^{-26}	(2.4×10^{-7})
Natural linewidth	E_w	7.3×10^{-28}	(4.6×10^{-9})

The energy levels of a nucleus are determined in part

by interactions of the nucleus with its environment. Interaction of the positive charge of the finite-radius nucleus with the negative charge of the s-electrons increases both the ground- and excited-state energy levels relative to those of a hypothetical point nucleus as shown in Figure 2.12b. Interaction of a nuclear magnetic moment with a local magnetic field splits both levels as shown in Figure 2.12c. Interaction of a nuclear quadrupole moment (non-spherical nucleus) with a local electric-field gradient splits the excited-state energy level as shown in Figure 2.12d. For the Fe-57 14.4 keV transition, these energy changes, E_h , are eleven orders of magnitude smaller than E_0 . Although small, they are key to Mossbauer spectroscopy because their magnitudes depend on the atomic environment (near neighbors, host-material crystal structure, etc.) of the Mossbauer isotope atom.

Mossbauer Spectroscopy

Mossbauer spectroscopy typically involves recoilless emission of monochromatic γ -rays from a cubic nonmagnetic source of known composition, recoilless absorption of these γ -rays by a specimen, and detection of photons or electrons either transmitted through or backscattered from the specimen. Since the atomic environment of the Mossbauer isotope in the source is usually different from that/those in the specimen, $E_{\gamma e}$ must be varied slightly for recoilless absorption to occur. This variation is achieved by vibrating the source with respect to the specimen, thereby changing $E_{\gamma e}$ by an amount

$$\Delta E_{\gamma e} = E_0(v/c)\cos \theta, \quad (2.6)$$

where v is the instantaneous velocity of the source toward the specimen, and θ is the angle between the vibration axis and the direction of γ -ray emission. The variation of $\Delta E_{\gamma e}$ with θ generally requires that the beam be collimated, especially for high-resolution work. (Bonazzola et al. (103) described a spectrometer having a multiwire proportional counter and a foil specimen as sectors of cylinders with a vibrating source at the common center. This arrangement eliminated the need for collimation and reduced the data collection time). The intensity of transmitted or backscattered photons or electrons is recorded as a function of source velocity. γ -ray transmission spectra which exhibit the hyperfine interactions discussed above are shown in Figure 2.12.

Backscattered-photon spectra look like the corresponding transmission spectra reflected across the velocity axis (i.e., maxima in backscattered intensity occur at the same velocities as do minima in transmitted intensity). Backscattered-electron spectra may look different because the only electrons detected are those that originated in a near-surface region of the specimen.

A Mossbauer spectrum is actually a superposition of subspectra due to Mossbauer isotope atoms in various atomic environments in the specimen. (The source is usually a dilute solution of the isotope in a cubic, nonmagnetic, host material, and therefore is assumed to emit monochromatic γ -rays.) For the simple case of a specimen of infinitesimal thickness comprising two, cubic, nonmagnetic, stoichiometric phases having different isomer shifts, the spectrum consists of two peaks having widths of $\approx 2\Gamma$. A mechanical mixture of two cubic, nonmagnetic, dilute, binary solutions produces a similar spectrum since almost all of the Mossbauer isotope atoms in each solution have only solvent atoms as near neighbors. In non-dilute solutions, the probability of a solute atom having one or more solute atoms as near neighbors is increased, effectively increasing the number of atomic environments. Peaks appear broadened if (1) the isomer shift varies with the number of near-neighbor solute atoms or (2) the loss of cubic symmetry due to a near-neighbor solute atom causes quadrupole splitting. Mixtures of non-cubic and/or magnetic phases produce spectra containing two-peak and six-peak subspectra whose peaks may appear broadened for the reasons given above. Additional peak broadening in all spectra is due to (1) vibration of the spectrometer, (2) a necessarily finite range of θ values (equation 2.6), (3) the finite thickness of source and specimen, and (4) the finite temperature of source and specimen causing atomic vibration.

Mossbauer spectra are usually deconvoluted by computer into sums of Lorentzian functions (99,122). Sums of Gaussian-Lorentzian convolution functions (104) and stored reference spectra (105) have been fitted to spectra with broadened or non-Lorentzian peaks. Deconvolution of overlapping subspectral peaks requires that constraints be imposed on the theoretical subspectra so that the final results are physically meaningful, not just statistically well fitting. Peak widths may be required to equal those in a reference standard spectrum. The relative peak intensities in a six-peak magnetically split Fe-57 subspectrum may be constrained to be 3:2:1:1:2:3, the ratios expected for a cubic magnetic specimen having no preferred orientation of the local magnetic fields (97). The relative peak intensities of a quadrupole-split peak may be constrained to be 1:1, the ratio expected for a specimen having no preferred orientation of the electric-field gradients (97).

Applications in Ferrous Metallurgy

Applications of Fe-57 Mossbauer spectroscopy in ferrous metallurgy include studies of atom-clustering, precipitation, order-disorder reactions, phase transformations, phase identification, volume fraction phase analysis, magnetic transformations, diffusion, and texture determination (98-102,106,85). Although x-ray diffraction and electron microscopy are often faster and more accurate techniques for these kinds of work, Mossbauer spectroscopy is the preferred technique in some cases. For example, Schwartz and Kim (82) were able to measure the austenite content of a 0.3 μm thick surface layer on bulk steel specimens via Mossbauer spectroscopy with backscattered electrons. X-ray diffraction sampled a 25 μm thick surface layer.

Several investigators (39,40,41,47-54) have used Mossbauer spectroscopy to detect the ordered FeNi ($L1_0$) phase. Even though this structure is ordered and has tetragonal symmetry, most x-ray diffraction results would show that it is face-centered cubic because (1) the edges of the unit cell are very nearly equal in length and (2) the difference in scattering factor of Fe and Ni for most x-rays is too small to produce detectable superlattice reflections. This phase is readily detectable by Mossbauer spectroscopy because the non-cubic environment of the Fe-57 atoms produces a measurable quadrupole splitting ($\approx 0.2\text{mm/s}$).

Since the Mossbauer techniques do not require interference of waves, they may detect atom clusters or particles that are too small to diffract x-rays coherently.

Finally, since transmission Mossbauer spectroscopy specimens can be much thicker than TEM specimens ($\approx 100 \mu\text{m}$ vs. $0.2 \mu\text{m}$), the effects of near-surface phase transformations can be reduced.

CHAPTER 3

EXPERIMENTAL

Materials

Two groups of laboratory-prepared, Fe-rich, Fe-Ni alloys were used in this study. Their compositions and thermomechanical treatments before aging are described below.

Composition and History

The first group comprised four Fe-Ni alloys with nominal Ni contents of 5, 9, 21, and 30 wt%. The compositions of these alloys are listed in Table 3.1.

Table 3.1. - Compositions (wt%) of the First Group of Alloys

<u>Alloy</u>	<u>Ni</u>	<u>C</u>	<u>Fe</u>
5R	5.05	0.009	bal.
9R	8.9	0.002	bal.
21R	20.9	0.022	bal.
30R	30.0	0.045	bal.

In an earlier study by Miller and Leslie (1), specimens of these four alloys were treated in the following manner:

1. Sealed in quartz capsules back-filled with a partial pressure of argon.
2. Heated to 1150°C, held for 7 days, air cooled, removed from capsules.
3. Heated to 1000°C, quenched in brine, refrigerated to -196°C.
4. Heated to 1000°C, quenched in brine, refrigerated to -196°C.

5. Cold rolled to 50% reduction in thickness, with reductions of 0.10 mm per pass, from an initial thickness of approximately 17 mm.
6. Wrapped in stainless-steel foil, heated to 300, 335, 400, or 450°C, held for 2000 hr, air cooled, removed from foils.
7. Cold rolled to 5-50% reduction in thickness.*
8. Wrapped in stainless-steel foil, heated to 300, 335, 400, or 450°C, held for 2000 hr, air cooled, removed from foil.
9. Cold rolled to 0-60% reduction in thickness.*
10. Wrapped in stainless-steel foil, heated to 300, 335, 400, or 450°C, held for 2000 hr, air cooled, removed from foil.
11. Cold rolled to 0-50% reduction in thickness.*
12. Wrapped in stainless-steel foil, heated to 300, 335, 400, or 450°C, held for 2000 hr, air cooled, removed from foil.

*It was originally intended to cold roll every specimen to 50% reduction in thickness in each of the four steps of rolling and aging. However, some specimens were cold rolled to lesser reductions either because they split upon rolling or because they became too hard to roll. The actual reductions and hardnesses are shown in Figures 4.9 and 4.10.

The second group comprised six Fe-Ni alloys with nominal Ni contents of 24, 26, 28, 30, 32, and 34 wt%. The compositions of these alloys, as hot rolled to 25-mm thick slabs, are listed in Table 3.2.

Table 3.2 - Compositions (wt%) of the Second Group of Alloys

<u>Alloy</u>	<u>Ni</u>	<u>C*</u>	<u>P</u>	<u>N*</u>	<u>O</u>	<u>Fe</u>
24	24.45	0.025	0.010	0.001	0.007	bal.
26	25.96	0.027	0.010	0.001	0.005	bal.
28	28.27	0.020	0.010	0.001	0.009	bal.
30	30.06	0.020	0.011	0.001	0.008	bal.
32	32.46	0.017	0.010	0.001	0.004	bal.
34	33.76	0.016	0.011	0.001	0.006	bal.

These alloys also contained approximately 0.01 Mo, 0.01 Co, 0.008 Zr, and 0.006 Cu.

Chemical analyses were done by Met-Chem Testing Laboratories, Inc., Dearborn, Michigan, using the following techniques:

Ni: Dimethylgloxime (gravimetric)
C: Leco Molecular Sieve (WR-12)
P: Phospho-Vanadate (colorimetric)
N and O: Leco Nitrogen-Oxygen Determinator (TC-36).

* The C and N concentrations were later reduced to ≈ 5 ppm during homogenization in Ar + 3 vol% H₂.

Thermomechanical Treatments

First Group of Alloys

Specimens of the first group of alloys which had been cold rolled twice and aged a total of 4000 hr at 335°C (alloys 5R, 9R, and 21R) or 450°C (alloy 30R) were treated in the following manner:

1. Heated to 950°C for 15 min, quenched in brine, cooled in liquid nitrogen (-196°C) for 25 min, warmed to RT.
2. Heated to 950°C for 15 min, quenched in brine, cooled in liquid nitrogen (-196°C) for 25 min, warmed to RT.
3. Cold rolled to 0, ≈ 25 , or ≈ 50 % reduction in thickness, with reductions of 0.013 mm per pass, from an initial thickness of approximately 4.5 mm.

These specimens were not subsequently aged at elevated temperatures.

Specimens of the first group of alloys which had been cold rolled four times and aged a total of 8000 hr were sectioned with a water-cooled abrasive saw, rinsed in water, rinsed in acetone, then allowed to dry before further aging.

Second Group of Alloys

Slabs of the second group of alloys were heated to

1100°C in a gas-fired furnace, then rolled to a thickness of 4 mm in eight passes of 20% reduction at the Climax Molybdenum Company of Michigan.

The hot-rolled sheets were cut into strip specimens ($\approx 100 \times 10 \times 4$ mm) with a water-cooled power hacksaw. The strips were cut so that the long edges were parallel to the rolling direction. After cutting, the strips were ground lightly to remove burrs, sandblasted to remove oxide scale, rinsed in water, rinsed in acetone, then allowed to dry.

Strip specimens were homogenized in two batches at 1200-1250°C for 250 hr, then furnace cooled, in flowing (2-2.5 l/hr) Ar + 3 vol% H₂. Homogenization was done in a mullite tube with the specimens separated by alumina powder to prevent welding. The temperature in the tube was measured with type K (chromel-alumel) and type S (Pt-Pt 10%Rh) thermocouples.

In order to reduce the austenite grain size and to produce uniform martensites, the homogenized strips were austenitized at 1000°C in air for 15 min, quenched in iced brine for 3 min, cooled in liquid nitrogen (-196°C) for 15 min, warmed in 45°C water for 15 min, cooled in iced water for 15 min, cooled in liquid nitrogen (-196°C) for 15 min, warmed in iced water for 15 min, then warmed in RT air.

The homogenized strips were divided into two groups which, because of subsequent heat treatments, would contain different amounts of austenite. One group was austenitized then twice cooled in liquid nitrogen as described above, then cooled in liquid nitrogen for 2.5 hr to promote the austenite-to-martensite transformation. The other group was austenitized at 1000°C in air for 15 min, quenched in RT water, then cooled to 16°C for 4 hr to produce structures with relatively high austenite contents that would be stable at RT.

The homogenized and heat-treated strips were cut into specimens of 2, 5, 10, 30, or 100 mm in length with a water-cooled abrasive saw, rinsed in water, rinsed in acetone, and allowed to dry.

Aging

Specimens were aged at 270, 300, 335, 370, 400, or 450°C for 0.1 to 14,000 hr. For aging times of 10 hr or less, small specimens ($\approx 2 \times 4 \times 10$ mm) were immersed in Pb or Pb + Bi baths. For aging times of 25 hr or greater, specimens were sealed in stainless-steel foil envelopes then

aged in electric resistance-heated furnaces.

Bath and furnace temperatures were measured with type K thermocouples. One Al-foil-wrapped thermocouple was placed near the specimens in each bath; two were placed between the envelopes in each furnace. The output from each of the twelve furnace thermocouples was recorded every ten minutes on a multi-point chart recorder. Furnace temperatures were usually maintained within 2°C of the desired values by three-mode controllers. Occasional power interruptions caused temperature deviations of ≈15°C downward.

After aging, the small specimens and envelopes containing specimens were quenched in RT water.

Testing and Analysis

Hardness Testing

Specimens for hardness testing were typically prepared by cutting ≈2 mm off one end of the original specimen with a water-cooled abrasive saw, mounting the remainder in polyester casting resin, then wet-grinding the newly exposed surface on SiC paper, finishing with 600-grit abrasive.

Indentations were made with a 136° diamond pyramid (Vickers) indenter and either a 10 or 30 kg load. The 10 kg load was used on specimens that were relatively thin (<2 mm) or relatively soft (≈100 HV). Indentations were made along the centerline of the 4 x 10 mm surface at approximately 3 mm intervals. Calibration of the hardness testing machine was checked before and after each session using two steel test blocks having hardnesses of 45.0 ± 1.0 HRC (446 ± 12 HV) and 23.4 ± 1.0 HRC (257 ± 6 HV) as standards.

Vickers hardness numbers (HV) were calculated as:

$$HV = 2P/d^2 \times \sin(\theta/2), \quad (3.1)$$

where P is the applied load, in kg; d is the mean diagonal length of the indentation, in mm; and $\theta = 136^\circ$ (107). The hardness of each specimen was calculated as the mean value of three or more measurements. Typical confidence intervals were calculated using the t statistic and unbiased estimates of population standard deviations (108).

Tensile Testing

Tensile testing was done to determine the yield strength, tensile strength, ductility, and strain-hardening exponent (uniform elongation) of several specimens.

Subsize strip specimens having a gage section of 2.5 x 6.25 x 25 mm (ASTM A 370) were used in tensile testing. Specimens were pulled with a crosshead speed of 0.02 mm/s. Elongation of the gage section was measured with a knife-edge extensometer. Applied load was measured with a 250 kN capacity load cell. Load and elongation data required to calculate tensile properties were read from the chart recording. Approximate RA values were calculated from carefully made measurements at the necked failure.

Co K α X-Ray Diffraction

X-ray diffraction using Co K α radiation was done to determine if the FeNi ordered phase was present in aged specimens. This radiation was chosen because, due to anomalous dispersion (109), it should produce stronger FeNi superlattice reflections than should other radiations. Danish (47), French (110), and Brazilian (49) workers have detected the FeNi 001 superlattice reflection using Co K α radiation.

Specimens for Co K α x-ray diffraction work were prepared by cutting \approx 2 mm off one end of the original specimen with a water-cooled abrasive saw, mounting the remainder in polyester casting resin, wet grinding the 4 x 10 mm newly exposed surface on SiC paper through 600-grit abrasive, polishing with 15, 6, and 1 μ m diamond paste, polishing with 0.05 μ m alumina slurry, then etching lightly with 5% nital to remove disturbed metal.

A horizontal-axis Philips diffractometer, a graphite monochromator, and a solid-state detector were used in this work. The operating conditions were: 35 kV tube voltage, 10 mA tube current, 0.5° slit size, 78 rpm specimen rotation, 0.125°/min 2θ scan speed, and 4 sec ratemeter time constant. The following ranges of 2θ were scanned to find the indicated reflections: 27-31° (001 FeNi superlattice), 50-52° (111 γ), 51.5-53.5° (110 a/a_2), 59.0-60.5° (200 γ), and 75.5 -79.0° (200 a/a_2).

Mo Ka X-Ray Diffraction

Volume fraction phase analysis was done by Miller's (61,74) technique to determine the relative amounts of bcc and fcc phases in several specimens.

Specimens for Mo Ka x-ray diffraction were prepared by sectioning the original specimen on a water-cooled, slow-speed, diamond saw to expose the midplane, mounting one half in polyester casting resin, wet grinding the 10 x 10 mm surface on SiC paper through 600-grit abrasive, polishing with 15, 6, and 1 μm diamond paste, polishing with 0.05 μm alumina slurry, then etching lightly with 5% nital to remove disturbed metal.

A horizontal-axis Philips diffractometer, a rotating-and-tilting specimen holder (111), and a scintillation counter were used in this work. The operating conditions were: 45 kV tube voltage, 20 mA tube current, 33 rpm specimen rotation, 23 cpm specimen tilt rate through $+60^\circ$, $0.25^\circ/\text{min}$ 2θ scan speed, 20 sec ratemeter time constant, 176 mm radius diffractometer circle, 0.25 mm wide vertical slit over tube window, and a 1.0 mm wide horizontal slit and a Zr foil filter over the detector window. The length of the vertical slit was adjusted so that the entire length of the specimen (parallel to the tilt axis) was irradiated when $2\theta=40^\circ$. The range of $30-40^\circ$ 2θ was scanned to detect the 220γ , $211a/a_2$, and 311γ reflections.

The volume fraction of austenite was calculated as

$$f = \frac{0.70(I_{220} + I_{311})}{I_{211} + 0.70(I_{220} + I_{311})}, \quad (3.2)$$

where I_{220} , I_{211} , and I_{311} are the integrated intensities (above background) of the 220γ , $211a/a_2$, and 311γ reflections. Background levels under the peaks were approximated with smooth curves drawn continuous with background levels on either side. Each peak was approximated with a smooth curve and then the integrated intensities (areas) were measured with a planimeter. The mean value of two measurements on each peak was used in the f calculation.

The conversion constant of 0.70 was calculated as the

ratio I_a/I_γ , where I_a is the intensity of the 211a reflection from a decarburized low-C bcc steel, and I_γ is the sum of the intensities of the 220 and 311 reflections from an fcc stainless steel. See the appendix for a derivation of equation 3.2.

Chemical Analysis

The C, N, and O contents of two series of specimens were measured to see if they changed significantly during aging.

Specimens for C, N, and O analysis were prepared by cutting ≈ 2 gm pieces from the original specimens, wet-grinding all surfaces on 240-grit SiC paper, ultrasonic cleaning for 15 min in ethanol, rinsing in ethanol, then drying in hot air. Carbon analyses were done using pre-baked crucibles in a Leco CS-244 (infra-red spectrometry) instrument reported accurate to ± 2 ppm C (112). Calibration was done with 470- and 99-ppm C standards.

Nitrogen analyses were done in a Leco TN-114 (thermal conductivity) instrument reported accurate to ± 1 ppm N (113). Calibration was done with 29-ppm N standards.

Oxygen analyses were done by Met-Chem Testing Laboratories, Inc., Dearborn, Michigan, in a Leco TC-36 instrument reported accurate to ± 2 ppm O.

Electron Microscopy and X-Ray Microanalysis

Transmission electron microscopy (TEM) was done to determine the size, shape, crystallography, and habit plane of precipitate particles. X-ray microanalysis by energy-dispersive x-ray spectrometry (EDS) in the scanning transmission electron microscope (STEM) was done to determine the composition of the particles.

Self-supporting thin foils for TEM/STEM work were prepared by cutting wafers ($0.3 \times 10 \times 10$ mm) from the original specimens with a water-cooled, slow-speed, diamond saw, wet grinding the wafers to 75 μm thickness on SiC paper through 600-grit abrasive, punching out 3.18 mm discs from the wafers with a shim stock punch and die, chemically thinning the discs to 25 μm thickness in 6 ml hydrofluoric acid (48%) + 150 ml hydrogen peroxide (30%), then electrochemically thinning to perforation in a single-jet thinner (114). Electrochemical thinning was done with

either of two electrolytes: 50 ml perchloric acid (70%) + 100 ml glycerol + 350 ml methanol (-45°C, 150 volts), or 100 gm anhydrous sodium chromate + 500 ml glacial acetic acid (20°C, 35 volts). Foils for x-ray microanalysis were "cleaned" for 10 min in an ion mill using argon, a 14° incidence angle, 6 kV, and 500 μ A/gun.

Precipitate-containing extraction replicas were prepared by sectioning the original specimen on a water-cooled, slow-speed, diamond saw to expose the midplane (10 x 10 mm), mounting one half in polyester casting resin, wet grinding on SiC paper through 600-grit abrasive, polishing with 15, 6, and 1 μ m diamond paste, polishing with 0.05 μ m alumina slurry, ultrasonic cleaning for 3 min in ethanol, rinsing in ethanol, etching by immersion in 2% nital for \approx 30 sec, rinsing with methanol, and drying in hot air. A piece of acetone-softened, 100 μ m thick, replicating tape was placed on the etched specimen, allowed to dry for 15 min, peeled off, carbon coated, then cut into 1.5 mm squares. Squares were placed on 180-mesh, C-coated, nylon grids. The replicating tape was dissolved away with acetone, leaving behind precipitate particles embedded in a carbon film supported on a grid.

Microscopy was done at 100 kV in a Hitachi 123E TEM and in a JEOL 100CX TEM/STEM modified by Allard and Blake (95) to produce "clean" x-ray spectra. A LaB₆ filament was used in the 100CX. EDS data were collected for 100 or 200 sec using the STEM in point mode with an estimated beam diameter of 15 nm. Specimens were held in a C holder in an Al stage tilted 35°. At least five spectra were collected per specimen.

EDS data were translated into chemical composition data using the Cliff-Lorimer (89) equation,

$$\frac{C_{Fe}}{C_{Ni}} = k_{FeNi} \frac{I_{Fe}}{I_{Ni}}, \quad (3.3)$$

where C_{Fe} and C_{Ni} are the concentrations of Fe and Ni in the volume analyzed, I_{Fe} and I_{Ni} are the measured intensities of the Fe Ka (6.40 keV) and Ni Ka (7.47 keV) characteristic x-rays, and k_{FeNi} is a constant. A foil of Fe-34Ni (not aged) and a specimen of Fe₂NiO₄ particles on a C film on a nylon grid were used to determine $k_{FeNi} = 0.793 \pm 0.012$. Characteristic x-ray intensities were obtained by fitting

the relatively flat spectrum from a carbon specimen to the background level near the Fe K α and Ni K α peaks, subtracting this fitted spectrum, fitting Gaussian peaks to the characteristic peaks, then integrating the characteristic peaks over the range of 180% FWHM of the corresponding Gaussians.

For statistical analyses, the integrated x-ray intensities were considered to have Gaussian distributions with mean $x = n$ and standard deviation $s = \sqrt{n}$, where n is the number of counts in the peak of interest. The standard deviation of any quantity that is a function of measured quantities, $y = f(x_1, x_2, \dots, x_n)$, was calculated from

$$s_y^2 = \sum (\partial y / \partial x_i)^2 s_{x_i}^2 \quad (3.4)$$

An average value of I_{Fe}/I_{Ni} for each specimen was calculated as the sum of the individual ratios, each weighted to reflect the uncertainty due to counting statistics (115).

Mossbauer Spectroscopy

Fe-57 Mossbauer spectroscopy was used to see if either the FeNi or FeNi₃ ordered phases formed during aging.

Foil specimens for transmission Mossbauer spectroscopy were prepared by cutting wafers (0.3 x 10 x 10 mm) from original specimens with a water-cooled, slow-speed, diamond saw, wet grinding the wafers to 75 μ m thickness on SiC paper through 600-grit abrasive, then chemically thinning to 7-12 μ m thickness in 6 ml hydrofluoric acid (48%) + 150 ml hydrogen peroxide (30%).

The spectrometer consisted of a MFG-N-5 function generator, a MDF-N-5 driver/amplifier, and a MVT-4 linear motor from Elscint (116); a PA-700 Kr + 3 vol% CO₂ filled proportional counter with pre-amplifier from Ranger (117); a TC-241 linear amplifier from Tennelec (118); and an ND62 multi-channel analyzer/computer terminal from Nuclear Data (119). The radioactive source was 25 mCi of Co-57 diffused into a 6 mm diameter spot on a 6 μ m thick Rh foil (120). Source-to-absorber and source-to-detector dimensions were 30 mm and 160 mm. Four layers of high purity (m5N5), 0.025 mm thick, Al foil (121) were placed 15 mm in front of the detector window to filter out the 6.4 keV Fe x-rays. Lead

shields were placed around the 3.2, 4.8, or 6.4 mm diameter exposed portion of the absorber to reduce the amount of extraneous radiation entering the detector. Single channel analyzer discriminators were set on either side of the 14.4 keV gamma-ray peak.

Mossbauer spectra were collected at RT using the transmitted 14.4-keV gamma rays, a source vibration frequency of 3 Hz, a triangular velocity waveform, a -7 to +7 mm/s velocity range, and 1024 channels of MCA memory. The MCA was operated as a multi-channel scaler controlled by clock signals from the function generator. Data were typically collected for 24 hr, accumulating about 200,000 counts per channel, then transferred to a computer for analysis.

Mossbauer data were analyzed by fitting six-line and single-line subspectra to the data, then comparing the hyperfine parameters of the fitted subspectra with those in the literature. A program by Wilson and Swartzendruber (122) was used to least-squares fit a function of the following form to the data:

$$F(x) = A+Bx+Cx^2 - \sum_{j=1}^n \frac{I_j (\Gamma_j/2)^2}{(x-x_j)^2 + (\Gamma_j/2)^2}, \quad (3.5)$$

where A, B, and C are constants; x is an MCA channel number; n is the number of spectral lines in the fitted spectrum; and I_j , Γ_j , and x_j are the intensity, width (FWHM), and position (MCA channel number) of the j^{th} line. Peak widths were constrained to equal that of the outermost peaks of the natural-Fe spectrum, 0.277 mm/s. Intensity ratios of lines in six-line subspectra were constrained to be 3:2:1:1:2:3. The program was calibrated (i.e., source velocities were assigned to MCA channels) using the six-line spectrum from a 12 μm thick natural-Fe ($\approx 2\%$ Fe-57) absorber and these hyperfine parameter values: isomer shift (relative to $\alpha\text{-Fe}$) = 0.0 mm/s, quadrupole splitting = 0.0 mm/s, and magnetic field strength = -330 kOe (123,124).

CHAPTER 4

RESULTS AND DISCUSSION

Hardness Testing

Figure 4.1 shows the variation in hardness with Ni content for Fe-Ni specimens as quenched to \approx RT and as cooled to -196°C . The hardness of the martensitic specimens varies little with Ni content, even when the structure changes from lath to plate at ≈ 29 wt% Ni. Similar data reported by Radcliff and Schatz (125) showed the hardness of Fe-Ni alloys containing 9 to 31 wt% Ni to be 260-265 HV. Inokuti and Cantor (16) found the hardness of specimens quenched in iced brine to increase from 200 HV at 10 wt% Ni to ≈ 250 at 20 wt% Ni, then remain constant out to 29 wt% Ni. (Their data for splat-quenched lath-martensite specimens showed a plateau at ≈ 700 HV for alloys containing 0 to 20 wt% Ni.) The difference in hardness between the data sets shown in Figure 4.1 for specimens cooled to -196°C is probably due to a difference in interstitial-solute content, the softer specimens having lower C and N concentrations.

The hardness of specimens quenched to \approx RT varies little with Ni content except near 29 wt% Ni. The abrupt decrease in hardness with increasing Ni content at 29 wt% Ni corresponds with an abrupt increase in retained-austenite content. See Figure 4.2. The specimens containing less than 29 wt% Ni were martensitic whereas those containing more than 29 wt% Ni were largely austenitic.

Figures 4.3-4.5 show the age hardening of Fe-Ni alloys cooled to -196°C before aging. Hardening occurred in all of the alloys and at all of the aging temperatures. As in other age-hardenable alloys, both the maximum hardness attainable and the time required to reach maximum hardness increased with decreasing aging temperature. A typical 95% confidence interval for the hardness values is given for each data set.

Age hardening increased with increasing Ni content up to 32 wt% Ni, then decreased. The maximum age hardening of 270 HV occurred in the Fe-32Ni martensite upon aging 8000 hr at 300°C . The lower-Ni alloys hardened less presumably because of their reduced Ni supersaturation increasing the

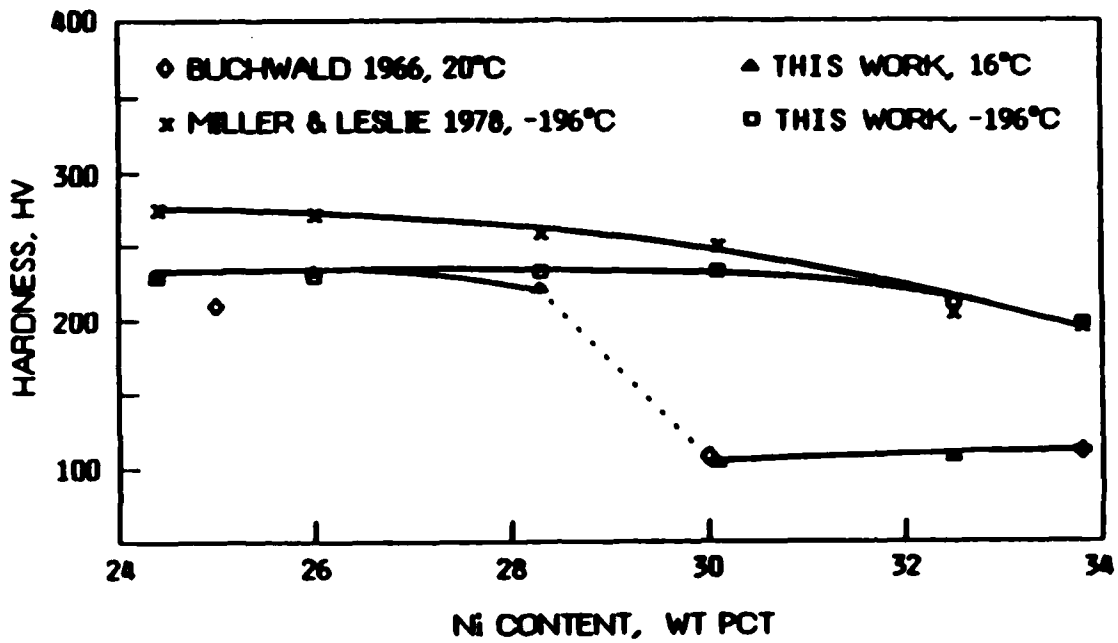


Figure 4.1 - Hardness of Fe-Ni specimens as quenched to \approx RT or as cooled to -196°C (1,2, and this work).

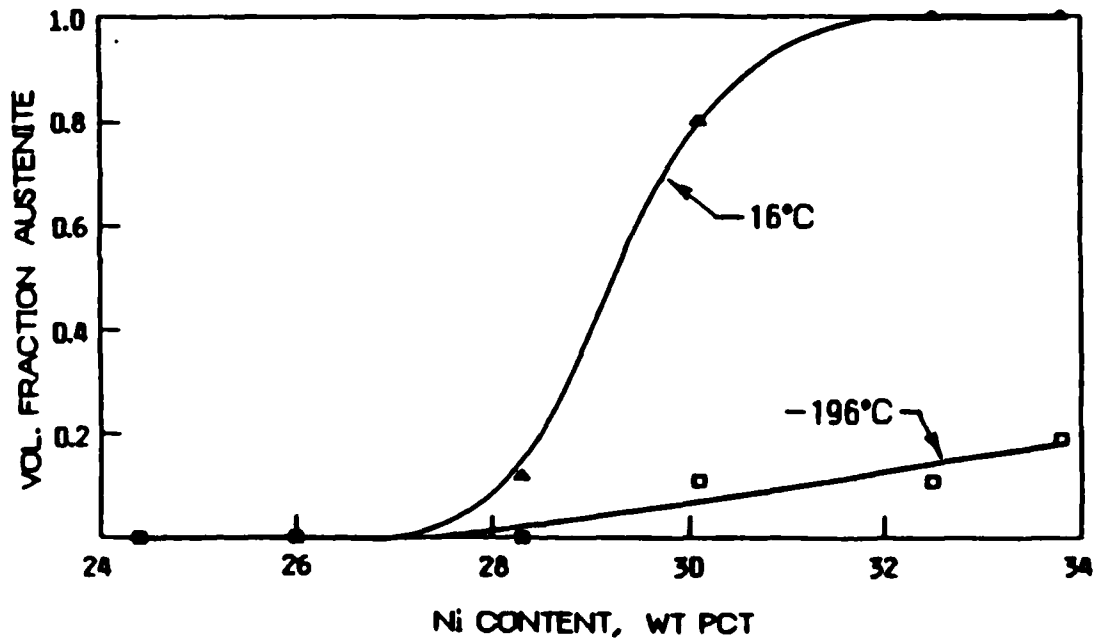


Figure 4.2 - Austenite content of Fe-Ni specimens as quenched to \approx RT or as cooled to -196°C .

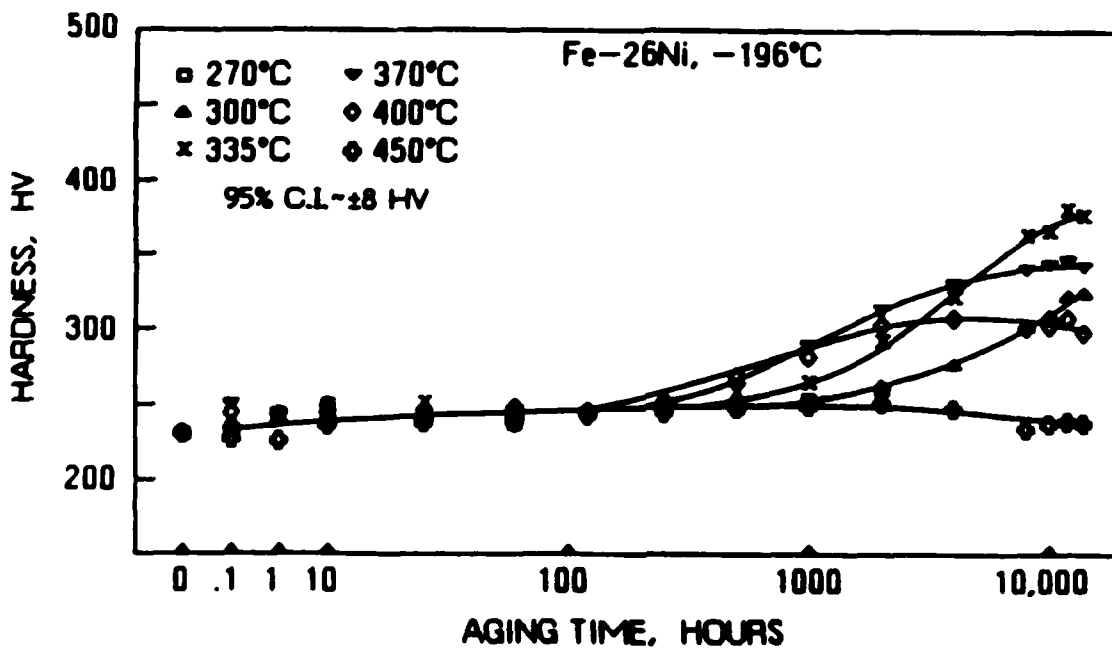
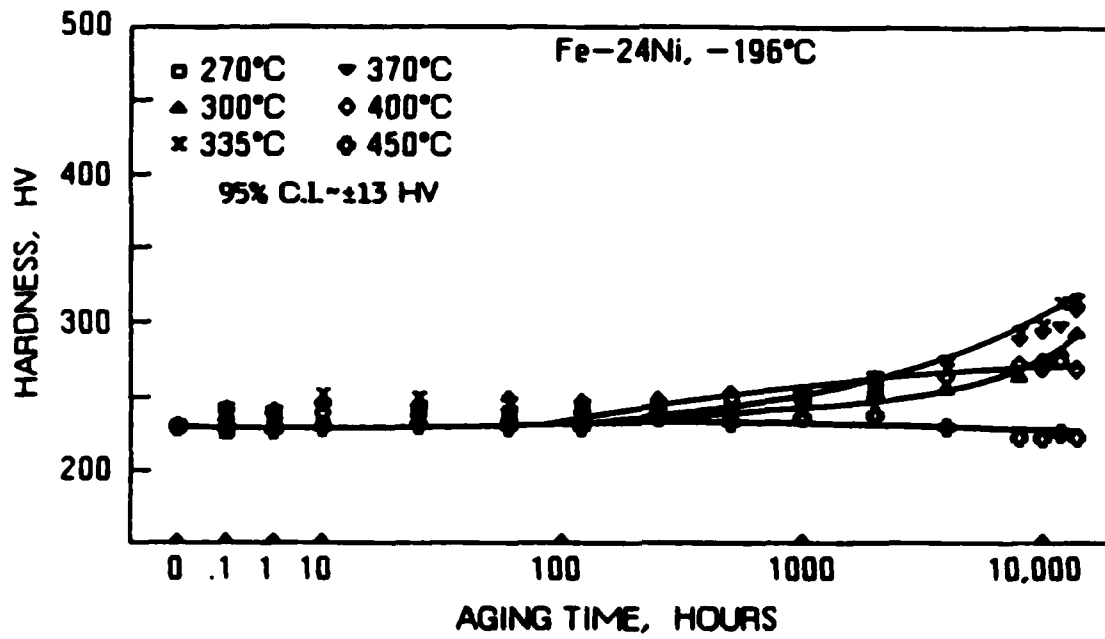


Figure 4.3 - Age hardening of Fe-Ni alloys cooled to -196°C before aging. (a) Fe-24Ni. (b) Fe-26Ni.

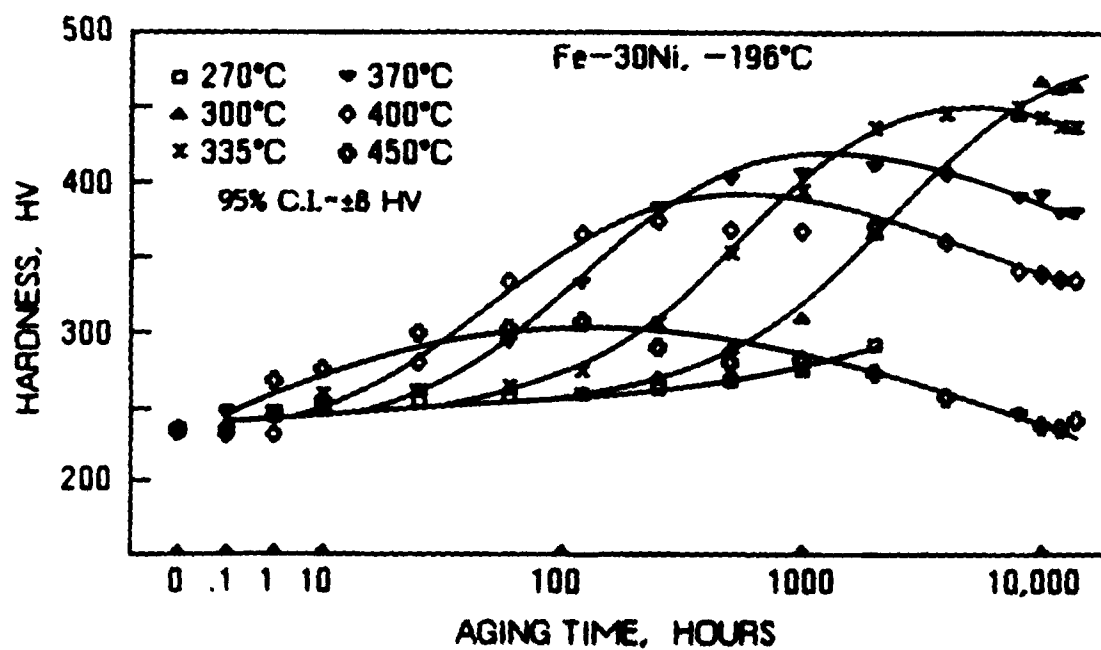
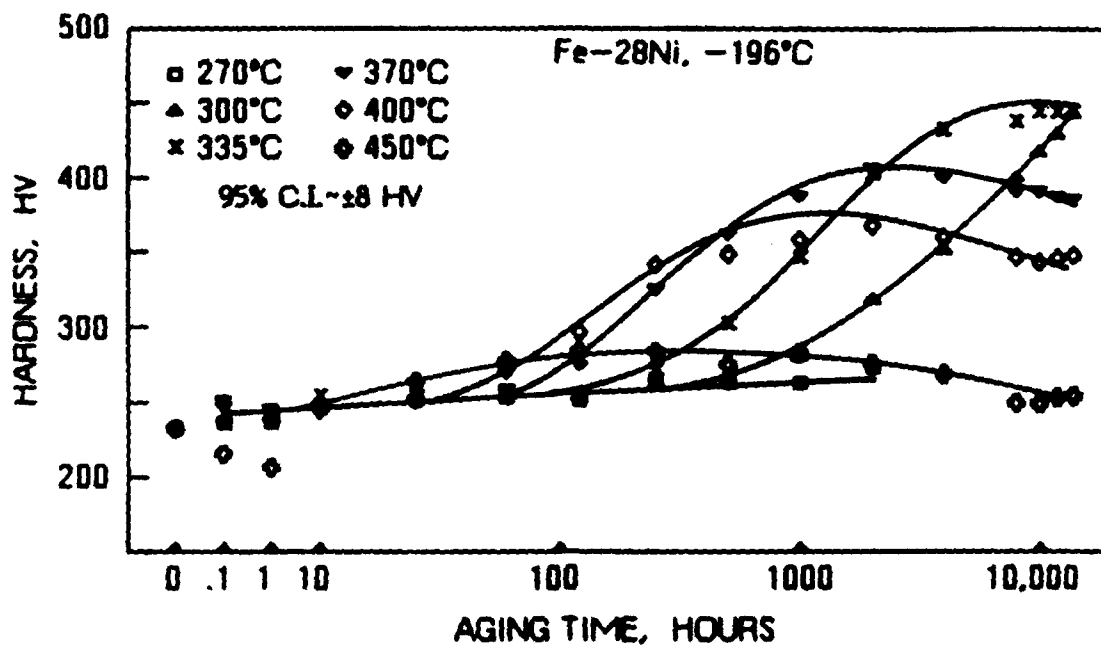


Figure 4.4 - Age hardening of Fe-Ni alloys cooled to -196°C before aging. (a) Fe-28Ni. (b) Fe-30Ni.

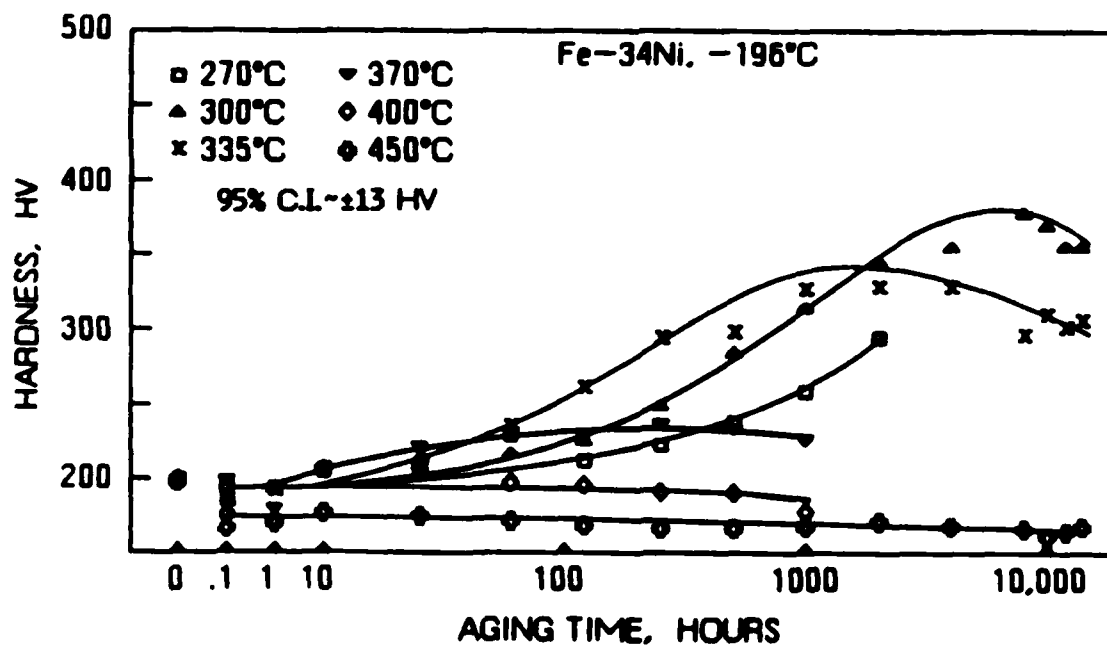
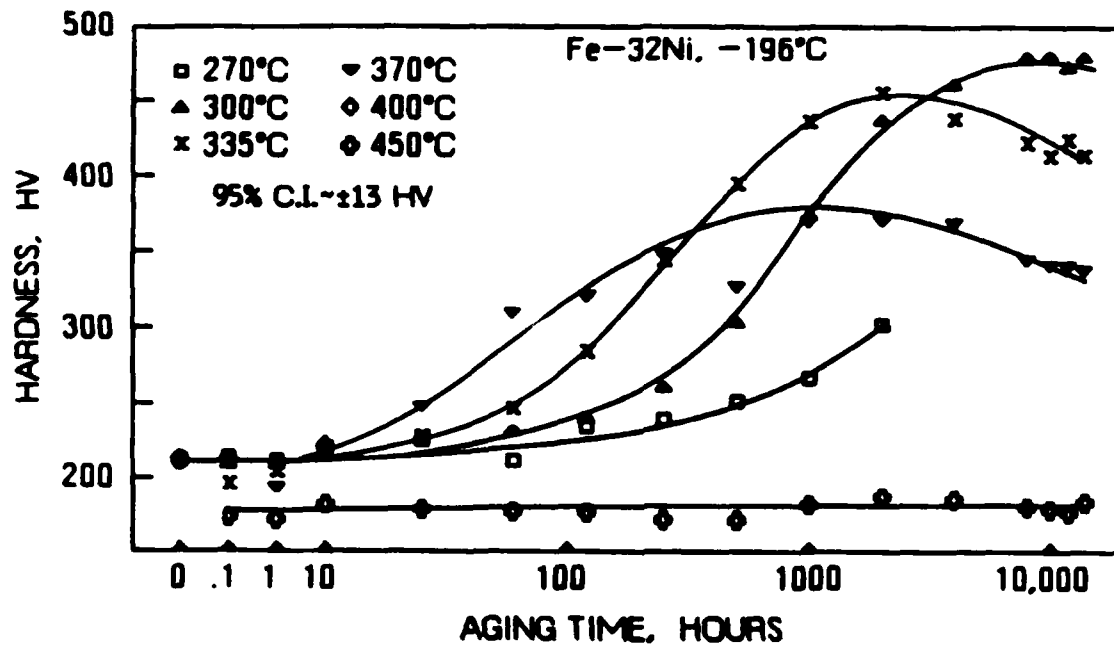


Figure 4.5 - Age hardening of Fe-Ni alloys cooled to -196°C before aging. (a) Fe-32Ni. (b) Fe-34Ni.

critical nucleus size and/or requiring more Ni diffusion to form a Ni-rich precipitate. The high-Ni alloy hardened less presumably because of its relatively high retained-austenite content. These regions of austenite do not harden and might grow during aging at the expense of austenite particles that would otherwise have formed in a fine dispersion.

The hardness data for aged specimens in Figures 4.3-4.5 are in good agreement with those of Miller and Leslie (1) with the following exceptions. The hardnesses of the 32 and 34 wt% Ni alloys aged 250 hr at 300°C and that of the 34 wt% Ni alloy aged 250 hr at 335°C in this work are ≈ 50 HV higher than those in (1). The hardness of the 30 wt% Ni alloy aged 120 hr in this work is ≈ 100 HV higher than that in (1).

Figures 4.6-4.8 show the age hardening of Fe-Ni alloys cooled to 16°C before aging. Compared to the hardness data for the same alloys cooled to -196°C before aging, these data are identical for the 24 and 26 wt% Ni alloys, and ≈ 20 HV lower across the board for the 28 wt% Ni alloy. The alloys containing 30 to 34 wt% Ni were largely austenitic, very soft, and did not age harden.

Figures 4.9 and 4.10 show the effects of cold rolling and aging on the hardness of four Fe-Ni alloys initially cooled to -196°C. Only the 30 wt% Ni alloy age hardened significantly. The increment of hardening due to aging at 300°C is slightly less than that for specimens aged without cold rolling, ≈ 200 vs. ≈ 230 .

Tensile Testing

Table 4.1 lists the mechanical properties of six Fe-Ni martensites both as cooled to -196°C and as aged. The yield strength of the as-cooled specimens decreases from 512 to 484 MPa as the Ni content increases from 24 to 34 wt%. Since the solid-solution strengthening should increase with increasing Ni content, the decrease in yield strength is probably due to the increase in retained-austenite content. The yield strengths listed here are about 60 MPa lower than those reported by Speich and Swann (18), perhaps due to lower C contents (≈ 5 vs. 17-38 ppm). The maximum yield and tensile strengths attained upon aging were 1134 and 1294 MPa, respectively.

The rather low values of uniform elongation listed for the as-cooled specimens are comparable to those reported for unhardened maraging steels (4). The ductility (%RA) of as-cooled specimens increases from $\approx 5\%$ to $\approx 75\%$ with increasing Ni content at 27 wt% Ni. A good explanation for this abrupt change is not available, but the low ductility of the low-Ni

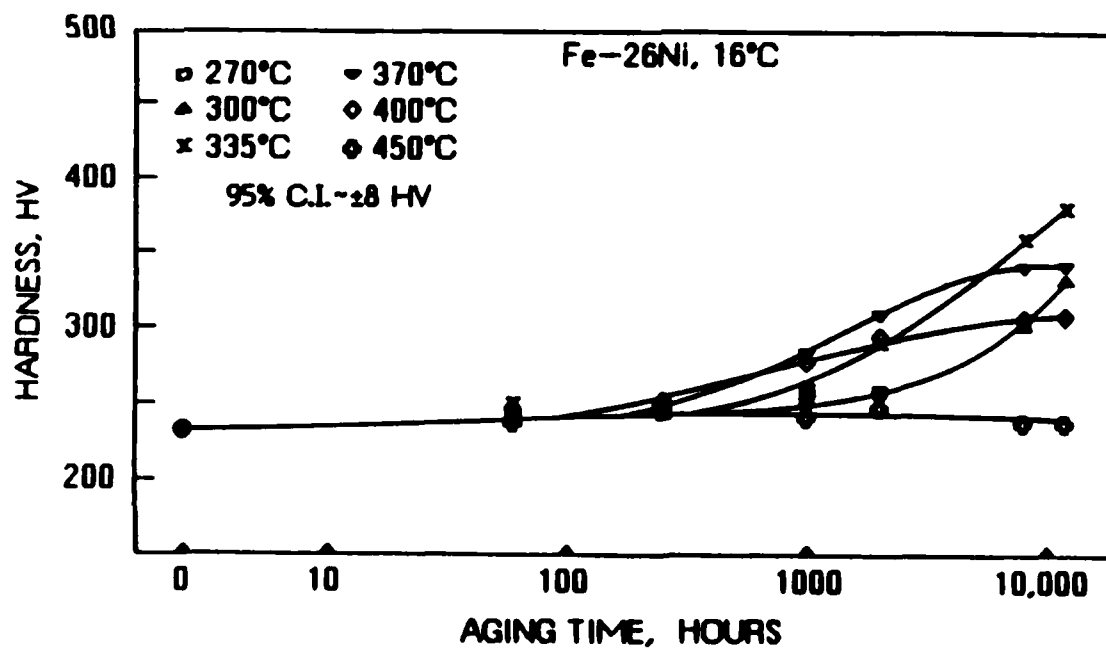
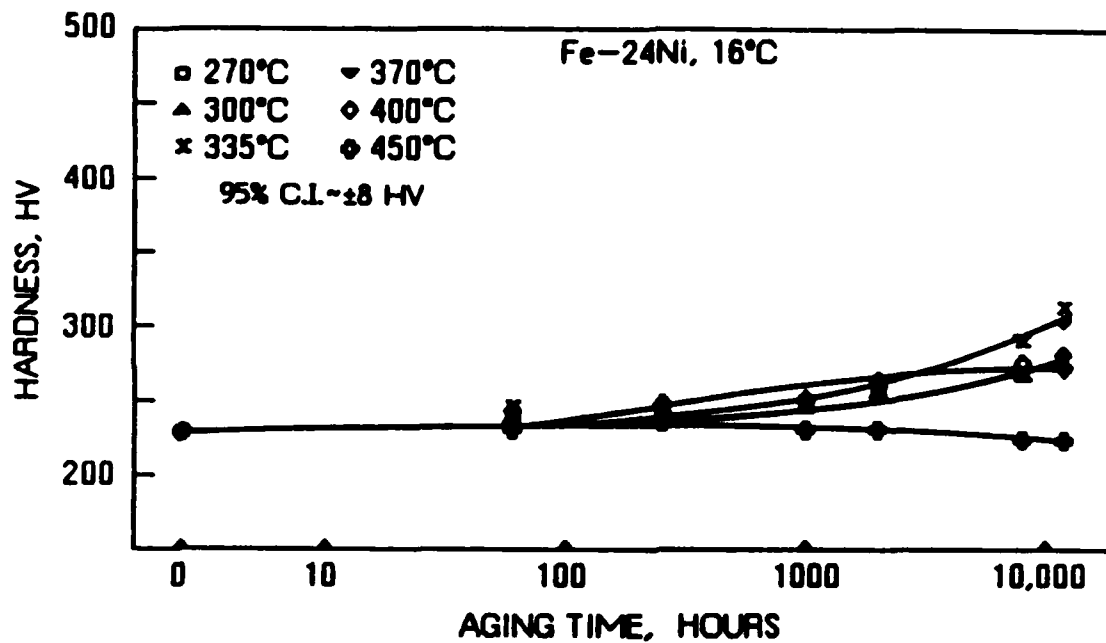


Figure 4.6 - Age hardening of Fe-Ni alloys cooled to 16°C before aging. (a) Fe-24Ni. (b) Fe-26Ni.

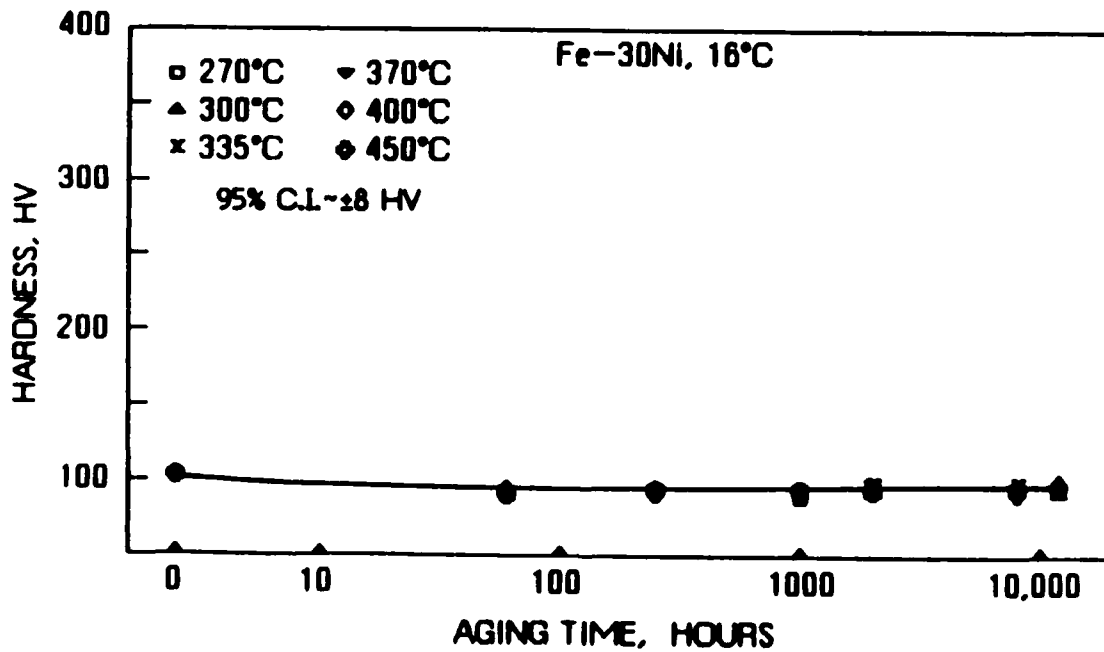
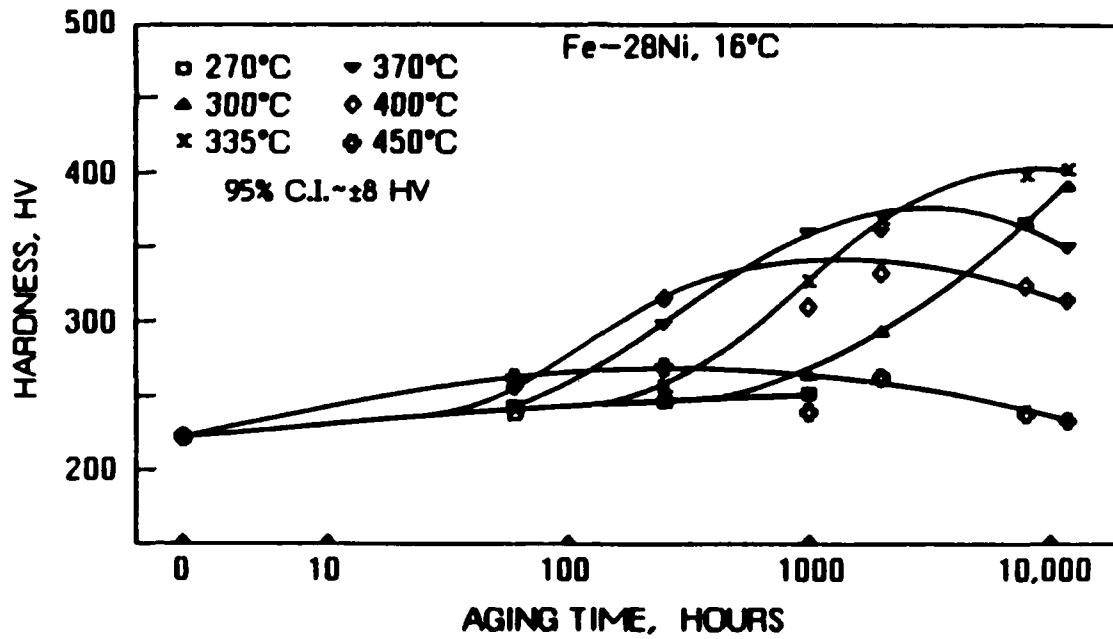


Figure 4.7 - Age hardening of Fe-Ni alloys cooled to 16°C before aging. (a) Fe-28Ni. (b) Fe-30Ni.

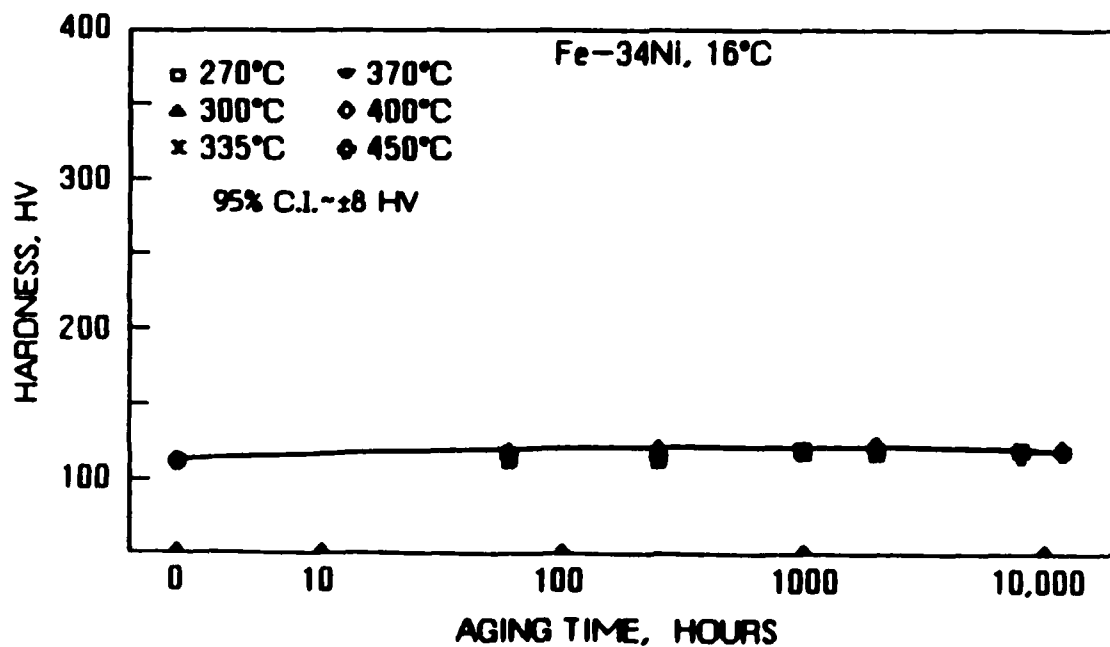
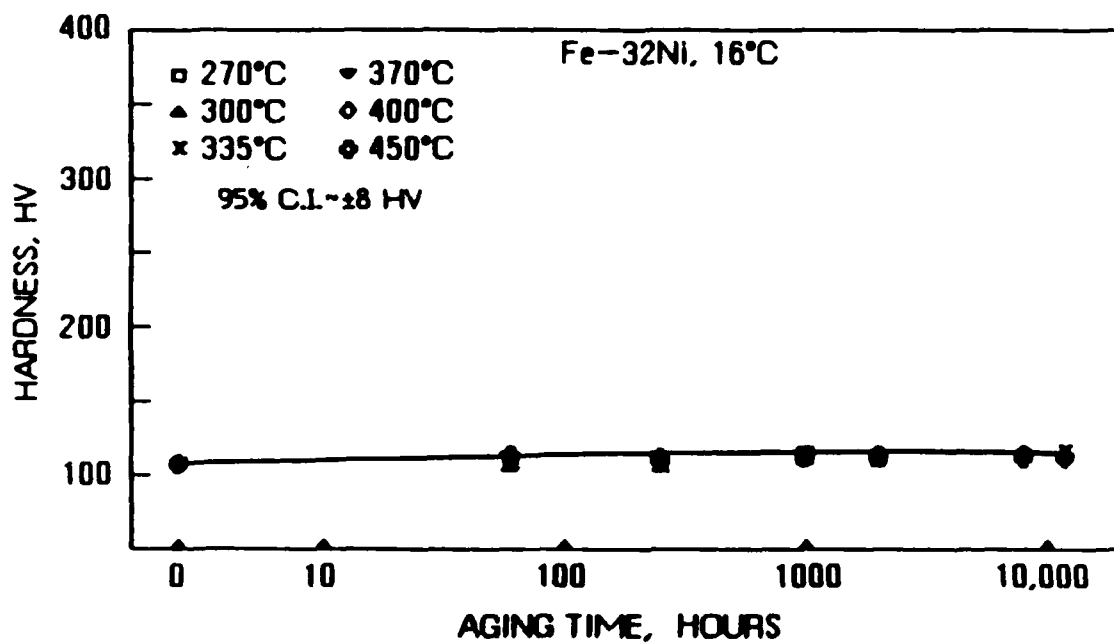


Figure 4.8 - Age hardening of Fe-Ni alloys cooled to 16°C before aging. (a) Fe-32Ni. (b) Fe-34Ni.

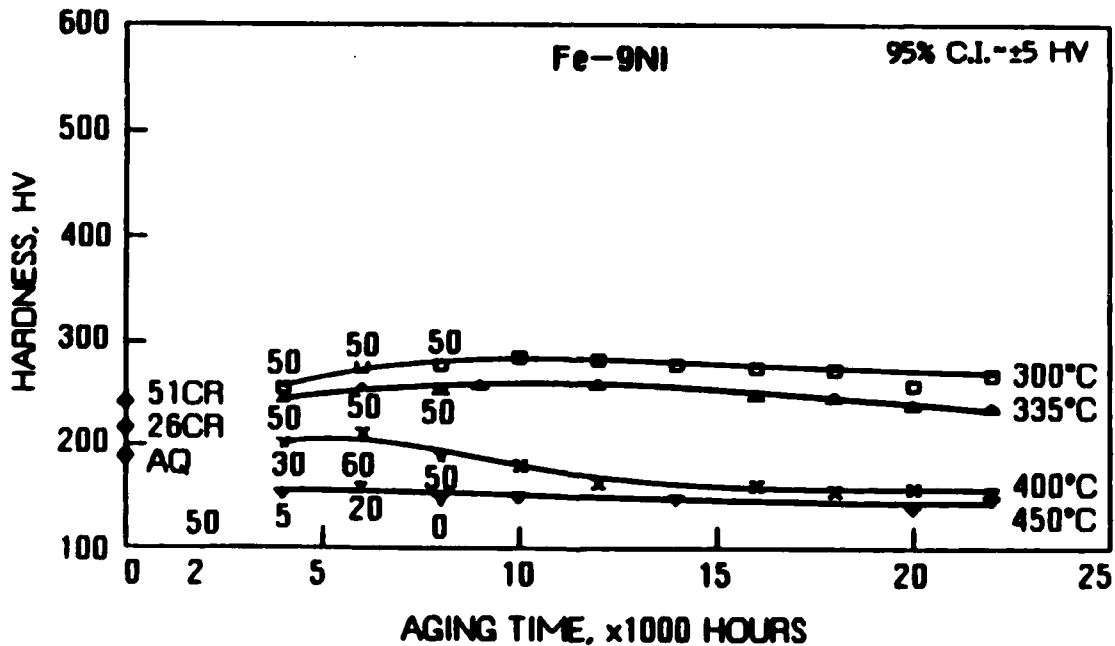
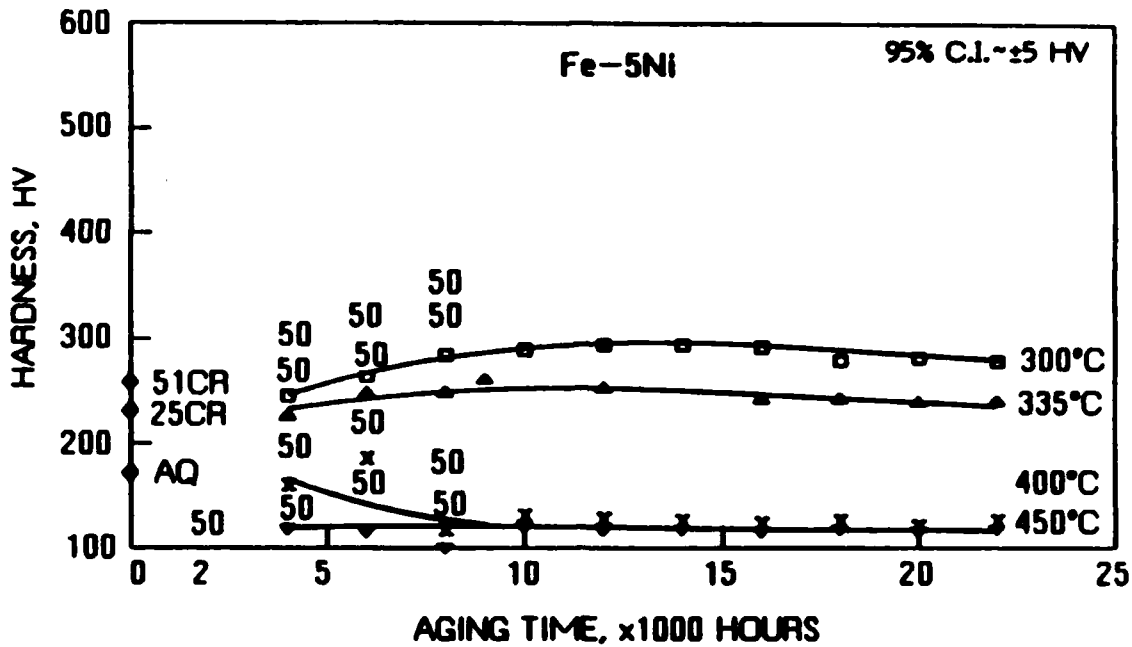


Figure 4.9 - Strain hardening and age hardening of Fe-Ni alloys initially cooled to -196°C . (a) Fe-5Ni. (b) Fe-9Ni. The number near each of some of the data points indicates the percentage reduction in thickness received by cold rolling prior to the 2000 hr increment of aging. Data for specimens aged 4000 to 8000 hr are from (1).

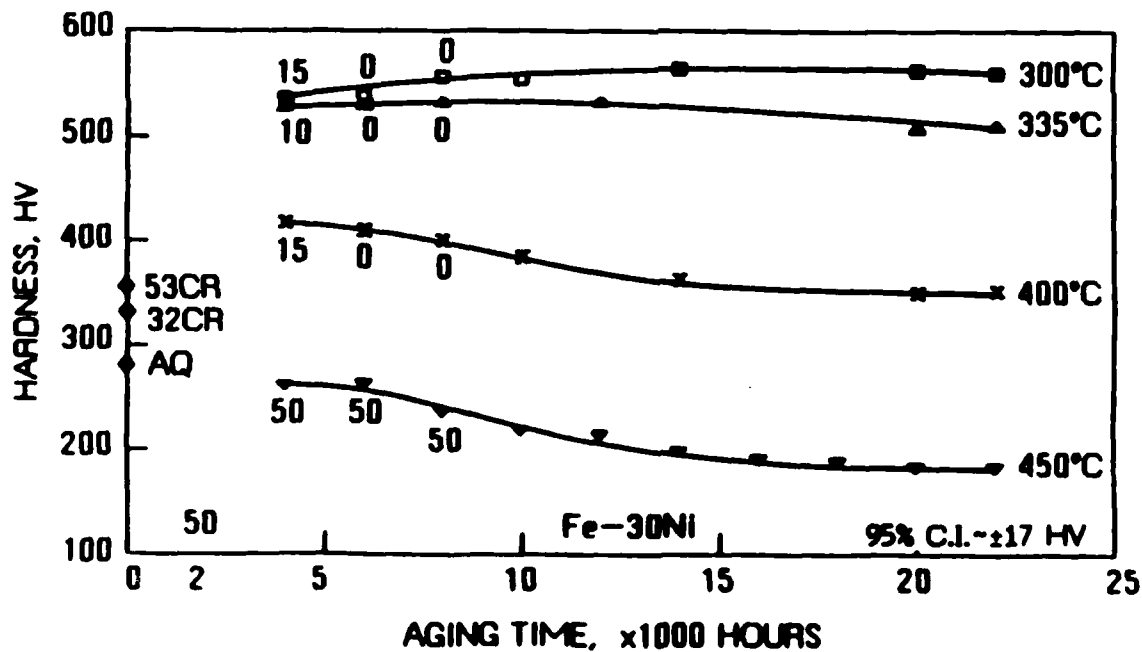
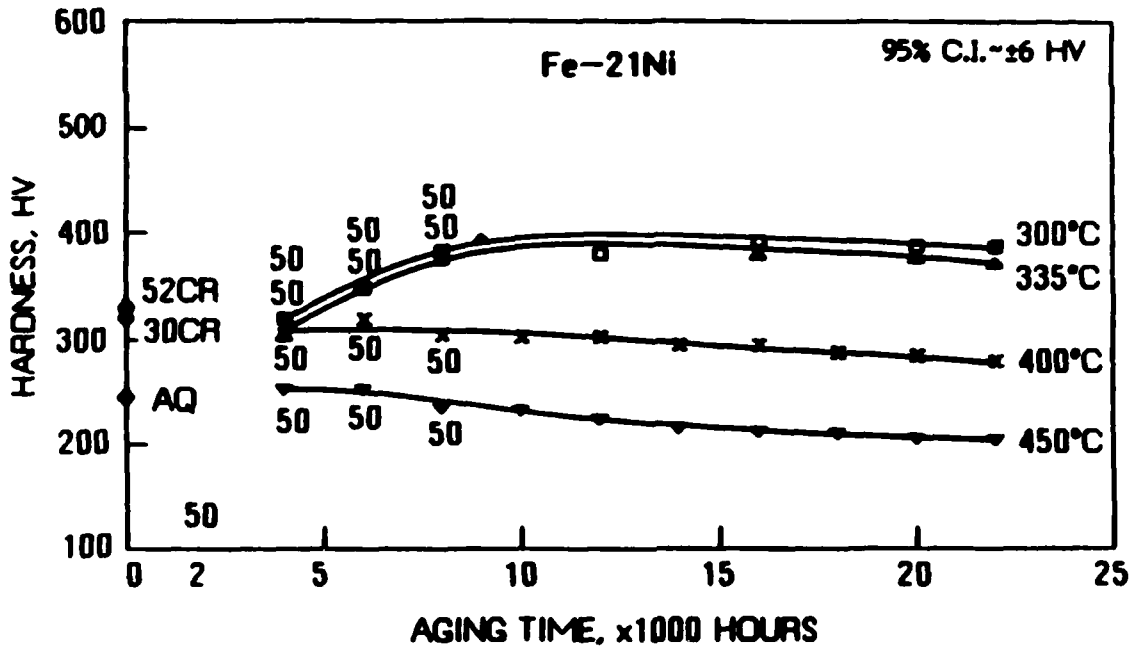


Figure 4.10 - Strain hardening and age hardening of Fe-Ni alloys initially cooled to -196°C . (a) Fe-21Ni. (b) Fe-30Ni. The number near each of some of the data points indicates the percentage reduction in thickness received by cold rolling prior to the 2000 hr increment of aging. Data for specimens aged 4000 to 8000 hr are from (1).

alloys is not surprising in light of two other observations. First, as-homogenized specimens of these two alloys were prone to cracking when stamped with identification marks. Second, an Fe-22Ni specimen solidified as a 6 mm diameter rod fractured when cold rolled to $\approx 20\%$ reduction in thickness.

Table 4.1 - Mechanical Properties of Fe-Ni Martensites

<u>Specimen</u>	<u>HV</u>	<u>YS, MPa</u>	<u>TS, MPa</u>	<u>UNIFORM ELONG., %</u>	<u>RA, %</u>
Fe-24Ni	229	512	645	1.0	2.2
Fe-26Ni	230	496	577	0.7	5.2
Fe-28Ni	231	497	720	2.9	78.
Fe-30Ni	230	496	723	4.4	72.
Fe-32Ni	211	484	640	4.4	73.
Fe-34Ni	195	484	593	5.5	73.
Fe-24Ni 500 hr 300°C	253	659	702	0.8	7.0
Fe-26Ni 1000 hr 370°C	289	726	778	0.8	4.8
Fe-28Ni 1000 hr 370°C	385	1095	1217	2.2	6.6
Fe-30Ni 1000 hr 370°C	403	1134	1294	1.8	4.9
Fe-32Ni 1000 hr 335°C	411	1024	1024	0.6	2.6
Fe-34Ni 1000 hr 300°C	305	644	1012	3.4	3.9

Chemical Analysis

Tables 4.2 and 4.3 list the measured O and C contents of Fe-30Ni specimens cooled to -196°C then aged at 300°C or 400°C . Estimated N contents are listed because the N contents indicated by the analyzer were negative. Since the analyzer was calibrated at 29 ppm N, and since the indicated

N contents were the same whether or not there was a specimen in the crucible, the negative readings were probably due to non-linearities in the calibration curve at low N contents. Because the O, N, and C contents are low and do not correlate well with specimen hardness, these elements must not be important in the hardening reaction.

Table 4.2 - O, N, and C Contents of Fe-30Ni Martensites

<u>Specimen</u>	<u>O</u>	<u>N</u>	<u>C</u>
As Cooled to -196°C	23 ppm	5 ppm	2.3 ppm
60 hr at 300°C		5	6.6
120 hr at 300°C	25		
1000 hr at 300°C		5	4.5
2000 hr at 300°C	34		
10,000 hr at 300°C	23		
12,000 hr at 300°C		5	1.7

Table 4.3 - O, N, and C Contents of Fe-30Ni Martensites

<u>Specimen</u>	<u>O</u>	<u>N</u>	<u>C</u>
As Cooled to -196°C	23 ppm	5 ppm	2.3 ppm
60 hr at 400°C		5	8.1
120 hr at 400°C	15		
1000 hr at 400°C		5	2.0
2000 hr at 400°C	19		
10,000 hr at 400°C	34		
12,000 hr at 400°C		5	2.9

Co Ka X-Ray Diffraction

Co Ka x-ray diffraction data were collected for specimens aged up to 2000 hr. Figure 4.11 shows two portions of the diffraction pattern from an Fe-32Ni specimen cooled to -196°C then aged 2000 hr at 335°C . The 200 fcc line appears relatively strong at $2\theta = 59.8^{\circ}$. The 001 FeNi ($L1_0$) superlattice line, if present, should appear at $2\theta = 28.9^{\circ}$, but was not visible on any of the diffraction patterns.

Mo Ka X-Ray Diffraction

Mo Ka x-ray diffraction data were collected for specimens aged up to 8000 hr. Figures 4.12-4.14 show the diffraction patterns from Fe-32Ni specimens cooled to -196°C then aged 0, 60, or 1000 hr at 400°C . The pattern from the unaged specimen consists of a strong 211 bcc line from the martensite and weak 220 and 311 fcc lines from the retained austenite. Decomposition of the martensite upon aging results in a weaker bcc line and stronger fcc lines. After 60 hr at 400°C , the lines are of comparable strength. After 1000 hr at 400°C , the bcc line from the remaining martensite and/or newly formed ferrite is much weaker than the fcc lines from the reverted austenite.

Austenite contents were calculated using the Mo Ka x-ray diffraction data and equation 3.2. Figure 4.15 shows the austenite content of Fe-32Ni specimens cooled to -196°C before aging. As expected, austenite content increases with aging time and aging temperature. For the specimens aged at 400°C or 450°C for 1000 hr, the austenite contents in Figure 4.15 are about 20 vol% higher than those calculated using the inverse-lever law and the proposed phase diagrams in Figures 2.3 and 2.4 (no corrections made for density difference). An error of 20 vol% seems too high for the volume-fraction austenite measurements. These high austenite contents might be rationalized by assuming that (1) the Ni-lean phase formed in the martensite decomposition is Fe_3Ni (Figure 2.8) and that (2) the Fe_3Ni phase appears as austenite in the diffraction patterns.

Electron Microscopy

TEM images of an Fe-32Ni specimen as cooled to -196°C are shown in Figure 4.16. The sets of fine dark lines are twins formed during the austenite-to-martensite

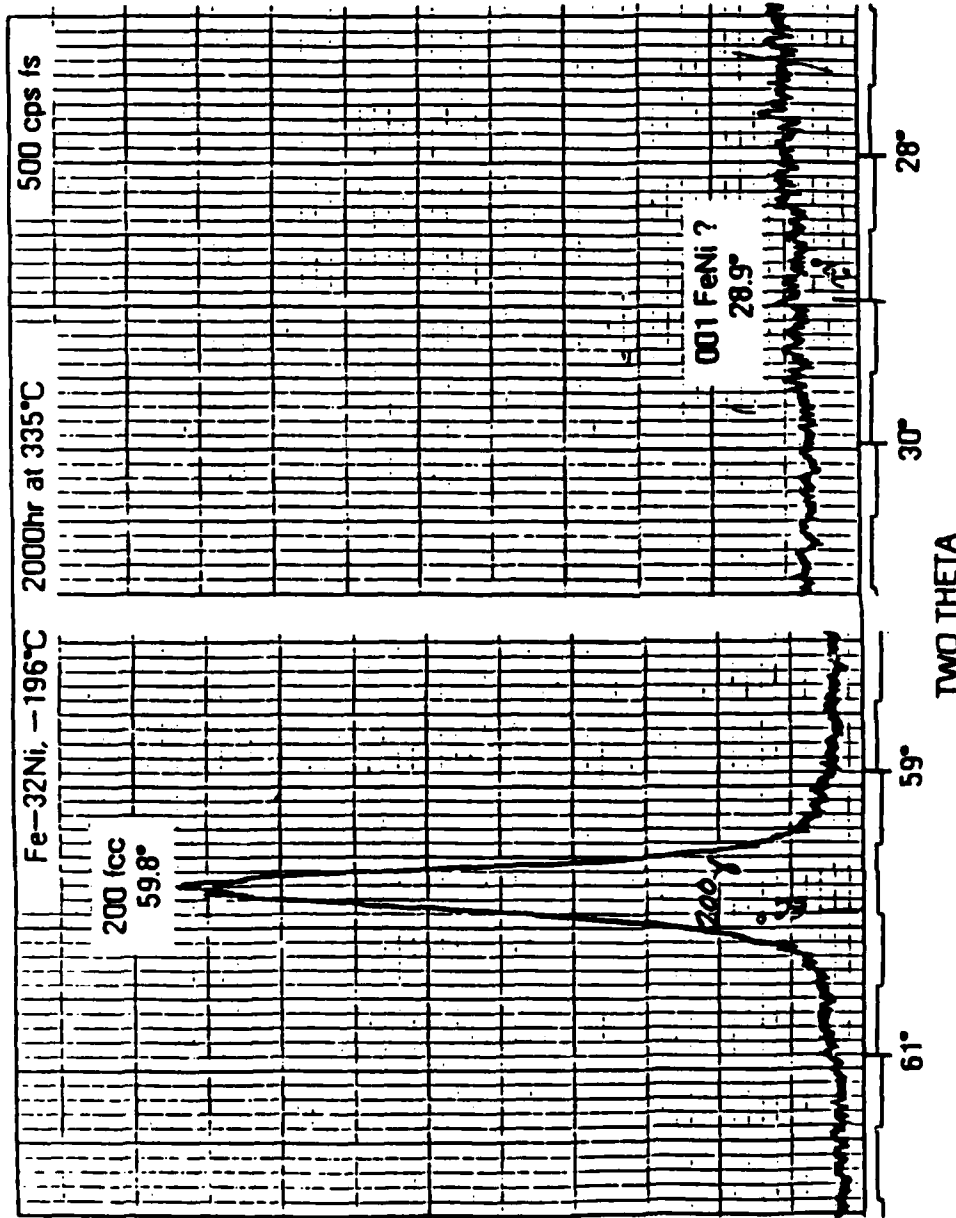


Figure 4.11 - Co K α x-ray diffraction pattern from an Fe-32Ni specimen cooled to -196°C then aged 2000 hr at 335°C.

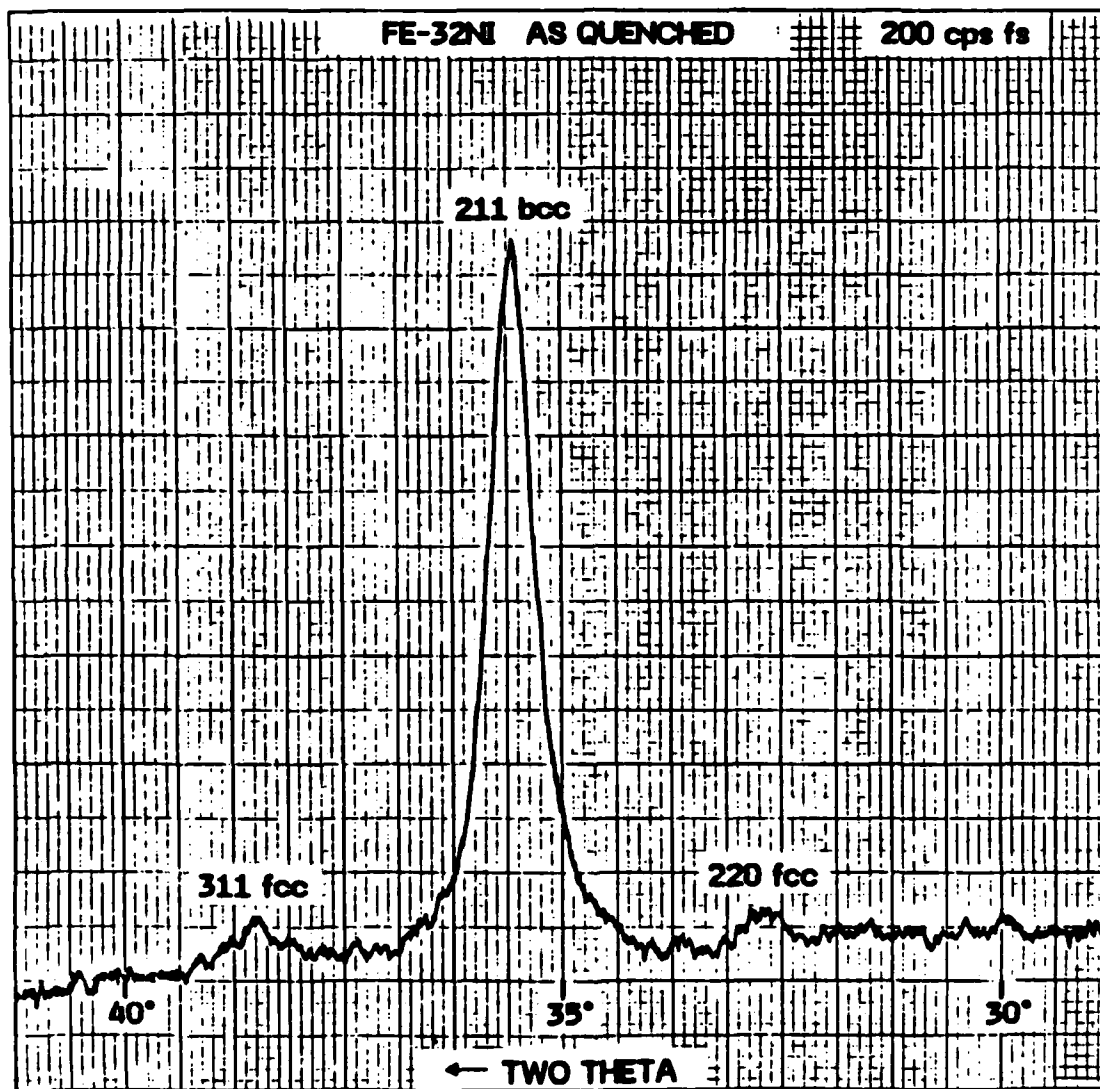


Figure 4.12 - Mo K α x-ray diffraction pattern from a rotating-and-tilting Fe-32Ni specimen as cooled to -196°C.

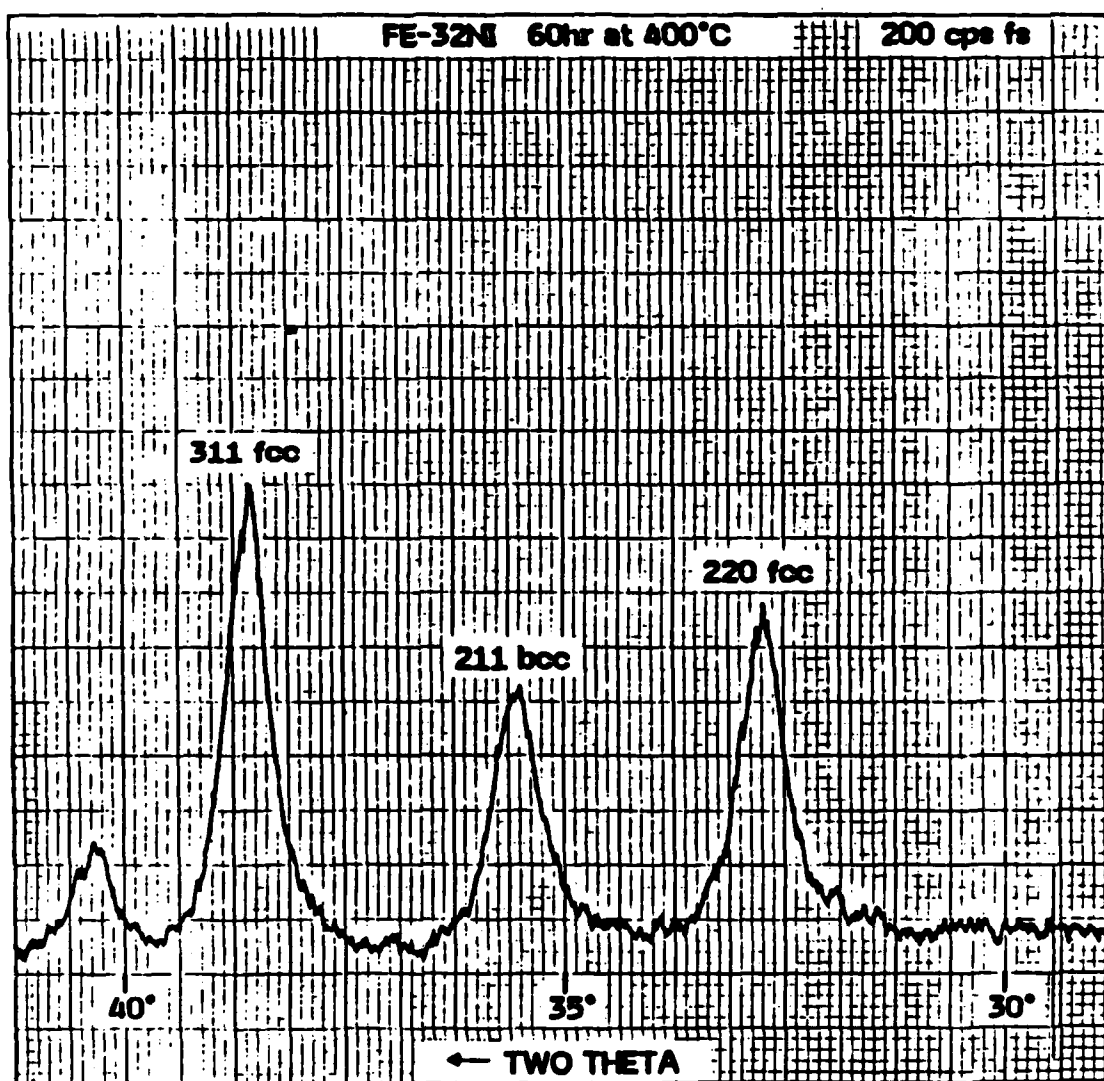


Figure 4.13 - Mo K α x-ray diffraction pattern from a rotating-and-tilting Fe-32Ni specimen cooled to -196°C then aged 60 hr at 400°C.

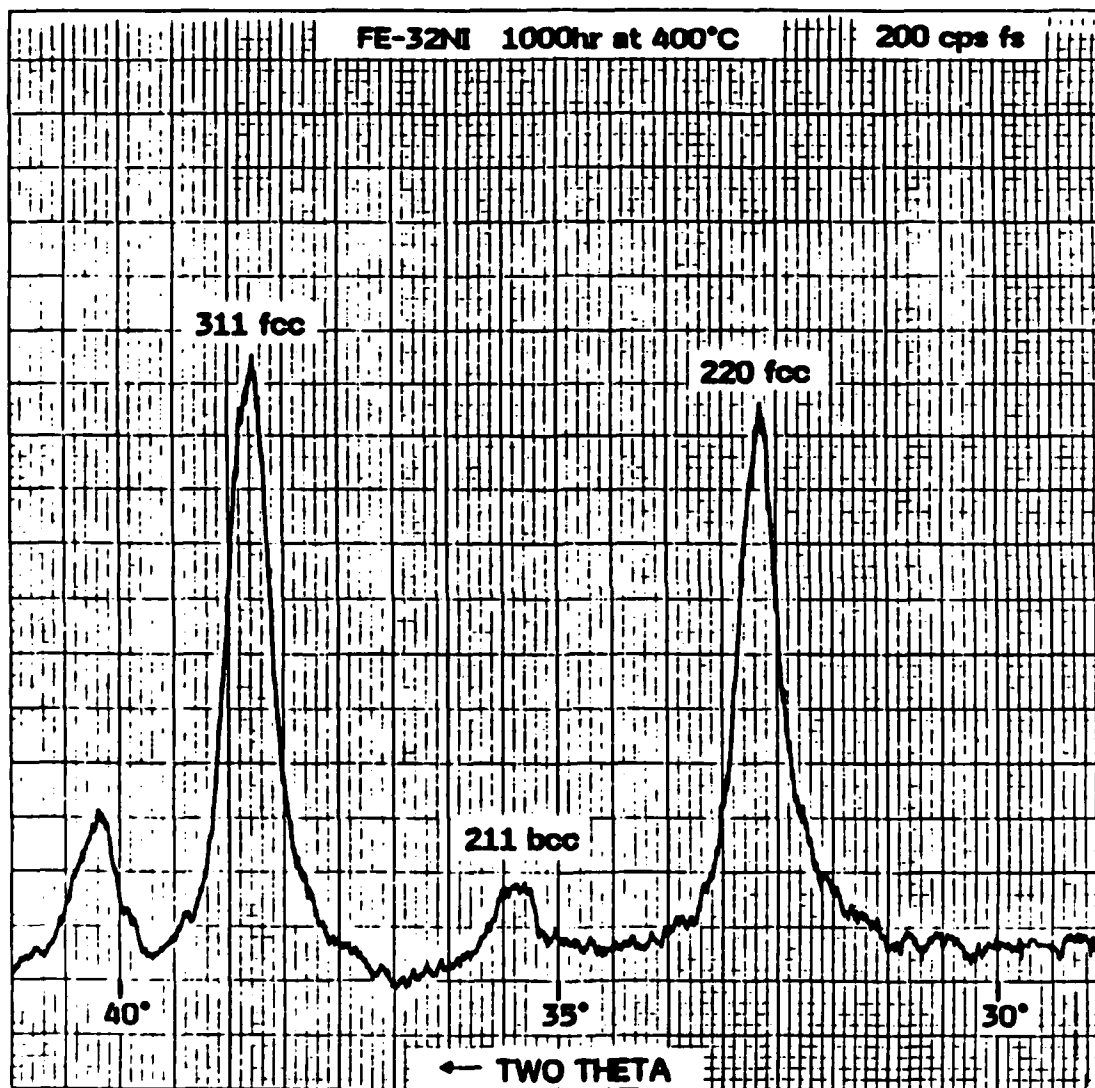


Figure 4.14 - Mo K α x-ray diffraction pattern from a rotating-and-tilting Fe-32Ni specimen cooled to -196°C then aged 1000 hr at 400°C.

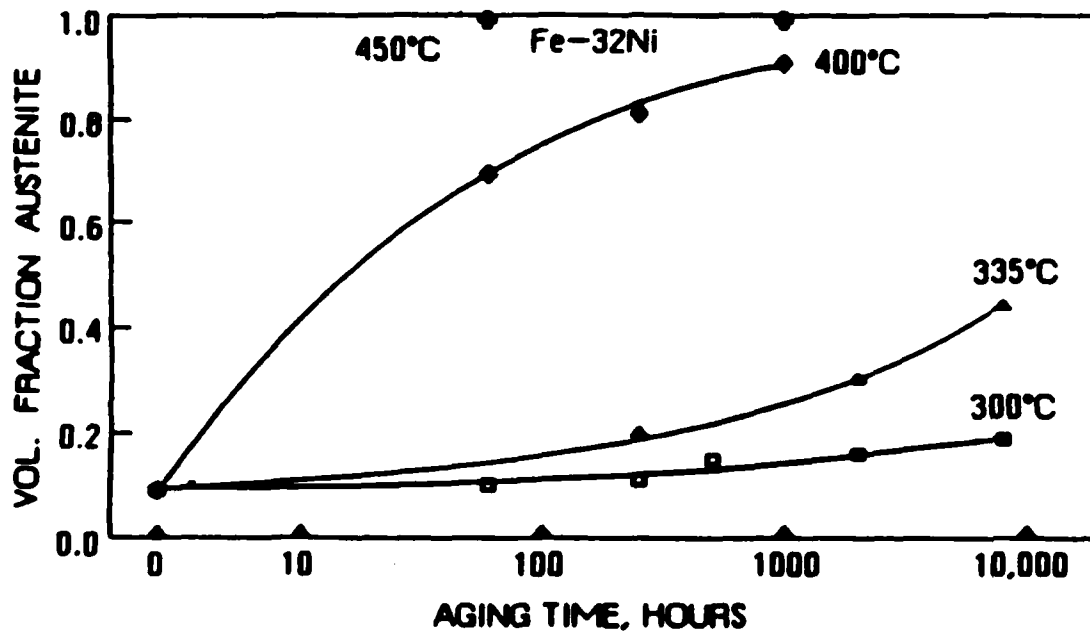


Figure 4.15 - Austenite content of Fe-32Ni specimens cooled to -196°C before aging.



Figure 4.16 - TEM images of an Fe-32Ni specimen as cooled to -196°C .

transformation. These are characteristic of ferrous alloys having low M_s temperatures. Spots on the corresponding diffraction pattern, shown in Figure 4.17, are streaked along $\langle 112 \rangle_{a_2}$ as a result of the fine twins on $\{112\}_{a_2}$ (126).

TEM images of an Fe-32Ni specimen cooled to -196°C then aged 250 hr at 335°C are shown in Figures 4.18 and 4.19. The long features crossing Figure 4.18 are remains of the twins evident in unaged specimens. They exhibit secondary twinning. The shorter features which are roughly parallel to or perpendicular to the primary twins are disc-shaped precipitates. They are similar in appearance to those found previously in these alloys (1), and to those found in the Carlton iron meteorite (44). Four orientations of the discs are evident in Figure 4.19. Three are roughly perpendicular to the foil and therefore appear as needles having some internal fine structure. The fourth is approximately parallel to the foil and appears as streaked dark regions in Figure 4.19a, and as more distinct dark regions in Figure 4.19b. The fcc spots on the corresponding diffraction pattern in Figure 4.20 are streaked along $\langle 111 \rangle_\gamma$, indicating that there are thin planar features in the austenite parallel to $\{111\}_\gamma$. These features may be twins or thin strained regions within the discs, probably near the disc/matrix interface. The bcc spots are streaked along $\langle 110 \rangle_{a_2}$ indicating that there are thin planar features in the bcc material parallel to $\{110\}_{a_2}$. These streaks are attributed to thin strained regions of the bcc matrix adjacent to the precipitate discs. Considering the bright-field images of the discs and the direction of spot streaking, the precipitate habit plane must be $\{110\}_{a_2}$. This is the same as the habit plane for austenite plates forming in Fe-Ni-Co martensites (8).

A TEM image of precipitate particles extracted from an Fe-32Ni specimen cooled to -196°C then aged 8000 hr at 335°C is shown in Figure 4.21. Except for minor distortions of the replicating tape and carbon film, the particles have the same relative positions that they had in the bulk specimen. The corresponding diffraction pattern in Figure 4.22 shows five broken "rings" from the 111, 200, 220, 311, and 222 planes of an fcc material with a lattice constant of 0.358 nm. The three sets of diametrically opposite pairs of intensity maxima (bright arcs) show that the particles have three crystallographic orientations in space.

Figure 4.23 shows the large volume fraction of precipitate present in an overaged specimen.

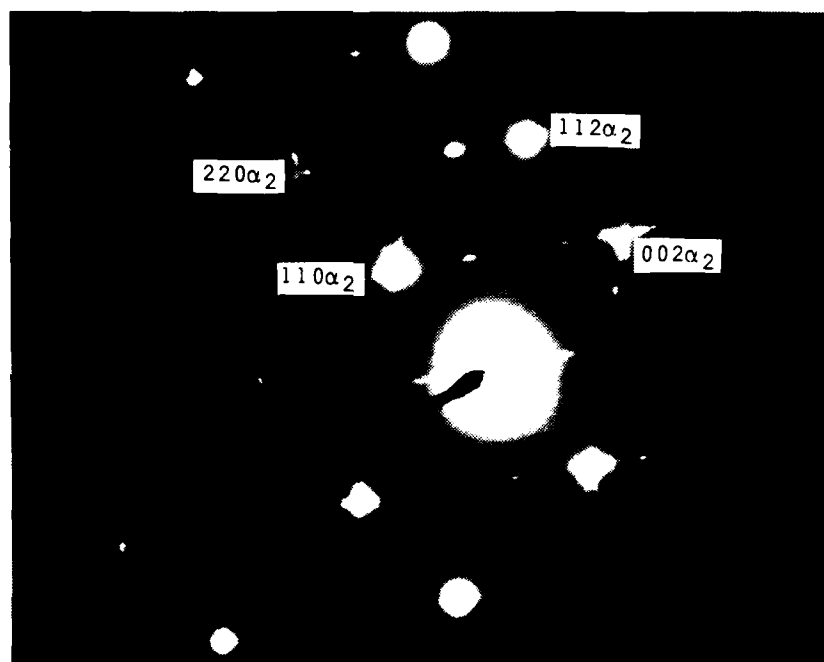


Figure 4.17 - Electron diffraction pattern from the specimen shown in Figure 4.16.



a

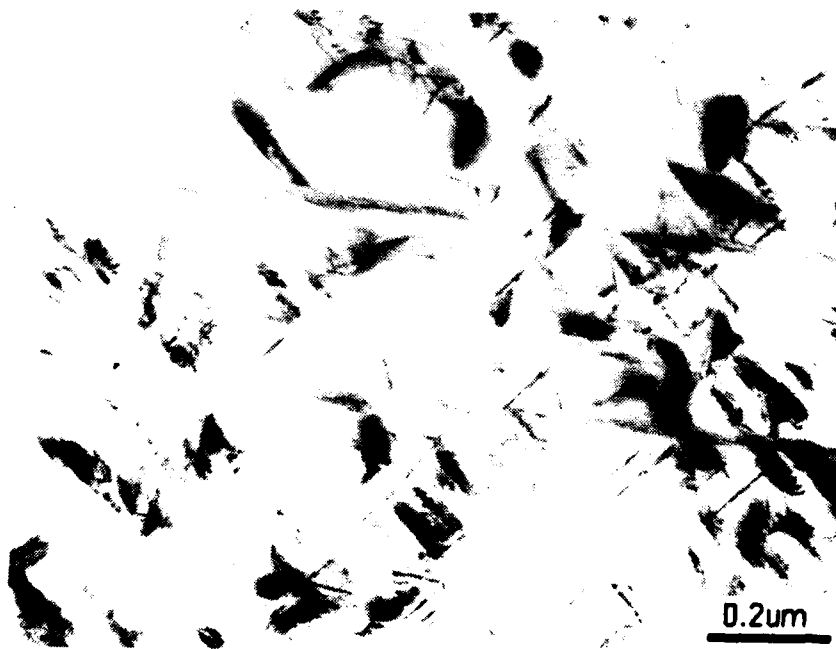


b

Figure 4.18 - TEM images of an Fe-32Ni specimen cooled to -196°C then aged 250 hr at 335°C .



a



b

Figure 4.19 - TEM images of an Fe-32Ni specimen cooled to -196°C then aged 250 hr at 335°C .

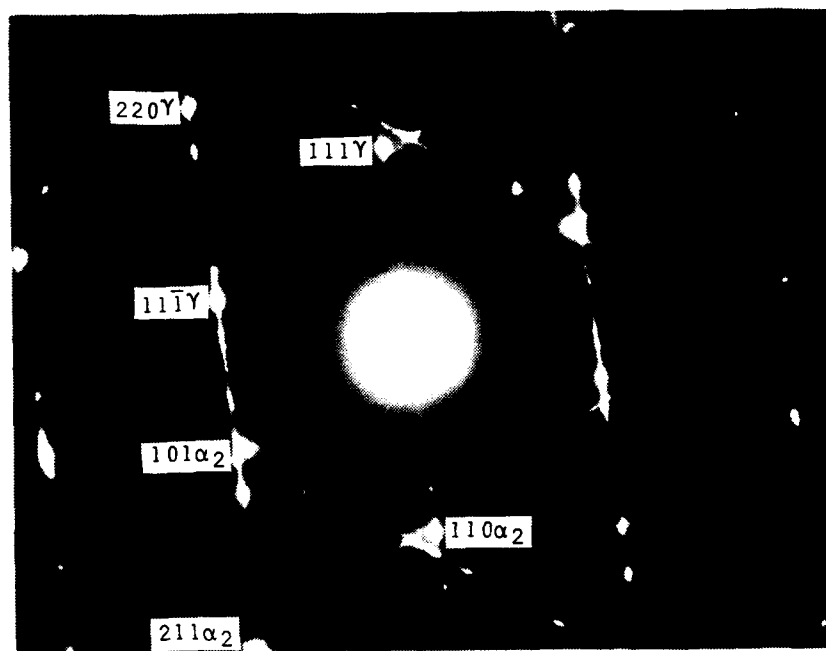


Figure 4.20 - Electron diffraction pattern from the specimen shown in Figures 4.18 and 4.19.



Figure 4.21 - TEM image of particles extracted from an Fe-³²Ni specimen cooled to -196°C then aged 8000 hr at 335°C.

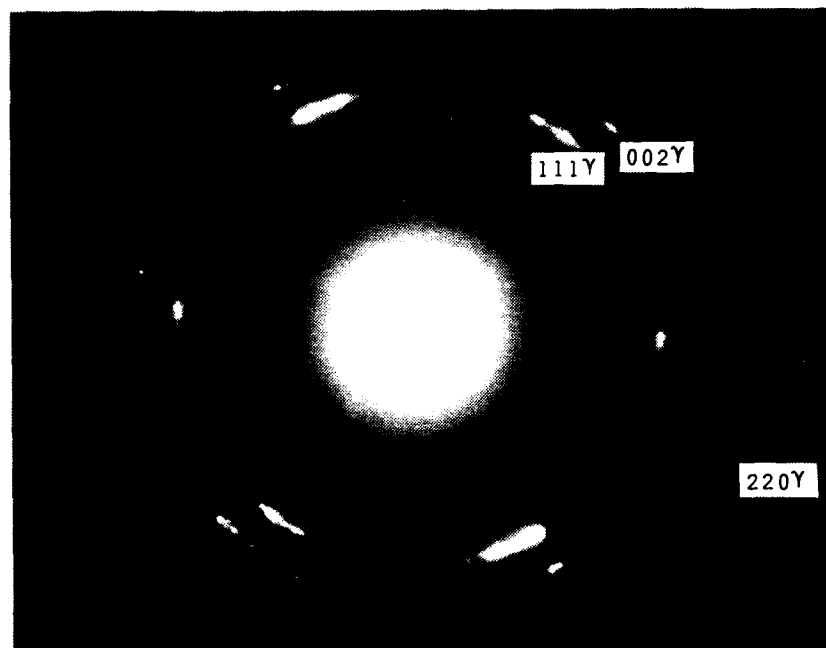


Figure 4.22 - Electron diffraction pattern from the particles shown in Figure 4.21.



Figure 4.23 - TEM image of a Fe-30Ni specimen cooled to -196°C then aged 60 hr at 450°C .

X-Ray Microanalysis

Three energy-dispersive x-ray spectra collected in the TEM/STEM are shown in Figure 4.24. The top spectrum was collected with the beam passing through a hole in an Fe-34Ni foil 1 μm from the edge of the hole. Weak Fe and Ni peaks are visible and are due to stray electrons and/or high-energy x-rays striking the specimen. The middle spectrum is from the Fe-34Ni foil itself. In addition to the Fe K α and Ni K α peaks used in the quantitative analysis, the K β and L peaks and the Al K α peak are visible. The Al K α peak is probably due to electrons and x-rays scattered from the specimen striking the Al stage. The bottom spectrum is from particles extracted from an Fe-30Ni specimen cooled to -196°C then aged 8000 hr at 335°C . Note that (1) the peaks are weaker than those in the middle spectrum due to the reduced amount of material in the beam and that (2) the strength of the Ni K α peak relative to that of the Fe K α peak in the bottom spectrum is greater than that in the middle spectrum. Therefore the particles must contain more than 34 wt% Ni.

Results of the x-ray microanalysis work with extracted particles are superimposed on a proposed Fe-Ni phase diagram in Figure 4.25. The extracted particles appear to have a higher Ni content than do the in-the-foil particles. The difference is probably due to spurious x-rays and specimen-preparation artifacts. First, the apparent Ni-content of in-the-foil particles may have been reduced by scattered electrons and x-rays exciting atoms in the Fe-rich specimen far away from the point of analysis. Second, the apparent Ni content of extracted particles may have been increased by re-deposition of Ni from the 2% nital etchant onto the particles during specimen preparation (127).

Mossbauer Spectroscopy

Figure 4.26 shows the Mossbauer spectrum from the 12 μm thick natural-Fe ($\approx 2\%$ Fe-57) foil used to calibrate the spectrometer. By definition, 0 mm/s velocity coincides with the centroid of this spectrum. The peak intensity ratios are near the ideal 3:2:1:1:2:3 expected for untextured specimens.

Figure 4.27 shows the Mossbauer spectra from $\approx 10 \mu\text{m}$ thick foils of Fe-30Ni. The spectrum from the as-cooled material consists of a single-line subspectrum near 0 mm/s from the paramagnetic retained austenite plus an asymmetric six-line subspectrum from the ferromagnetic martensite. Numbering the peaks of the six-line spectrum from left to

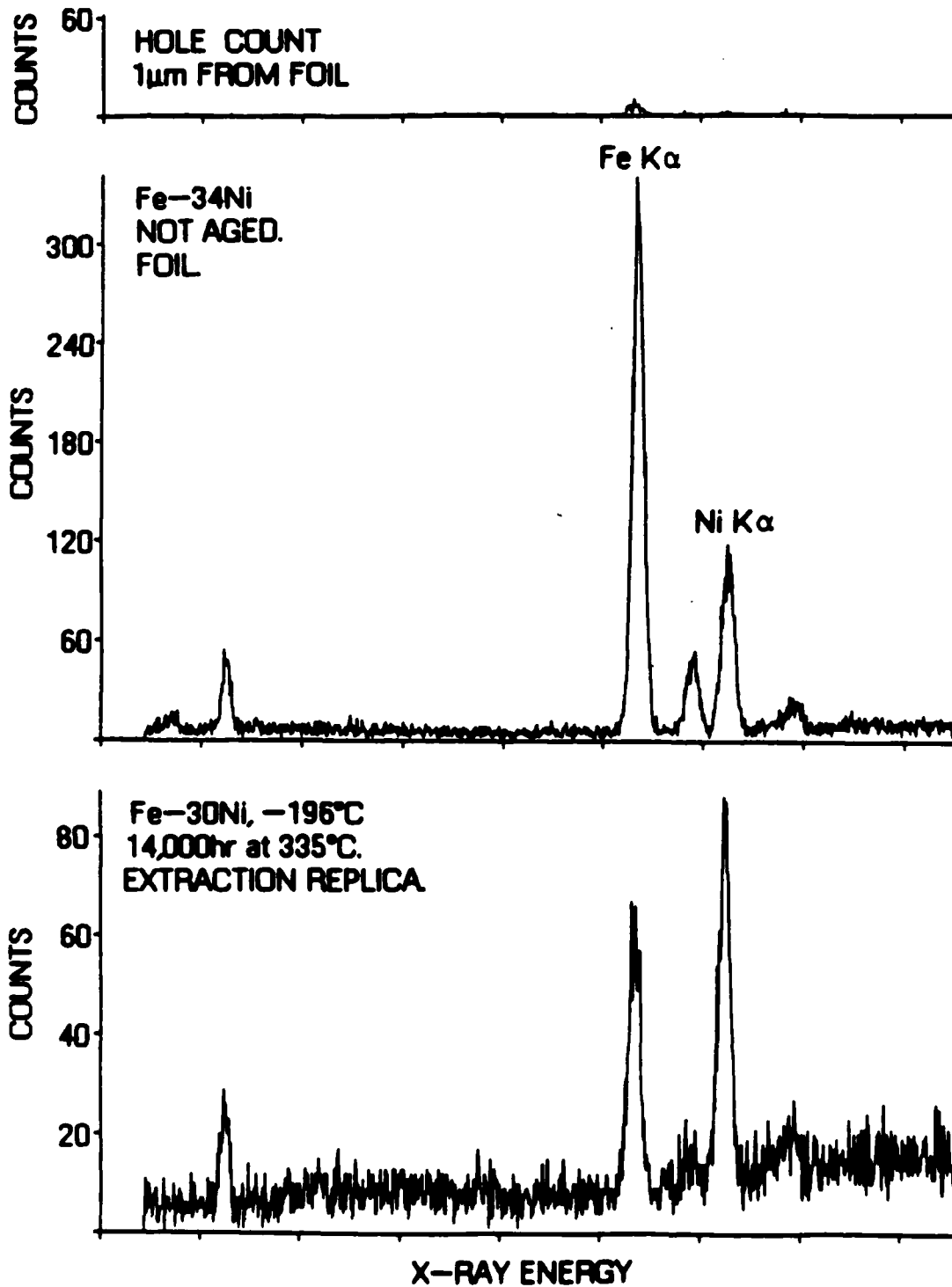


Figure 4.24 - Energy-dispersive x-ray spectra collected in the TEM/STEM. Collection time = 200 sec.

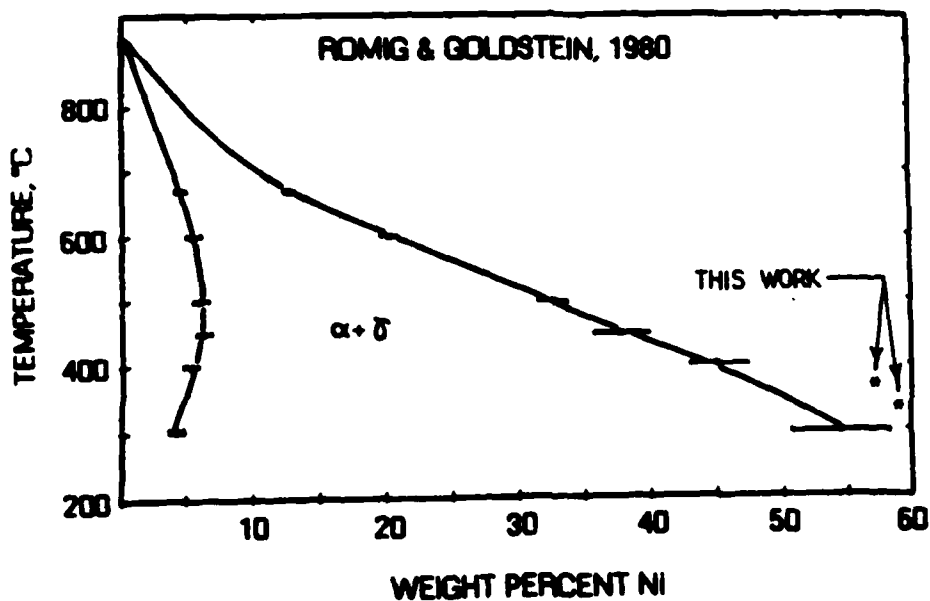


Figure 4.25 - Ni content of austenite formed by the decomposition of Fe-Ni martensites as determined by x-ray microanalysis of thin foils (94) and extracted particles (this work). The error bars for this work are ± 5 wt% Ni.

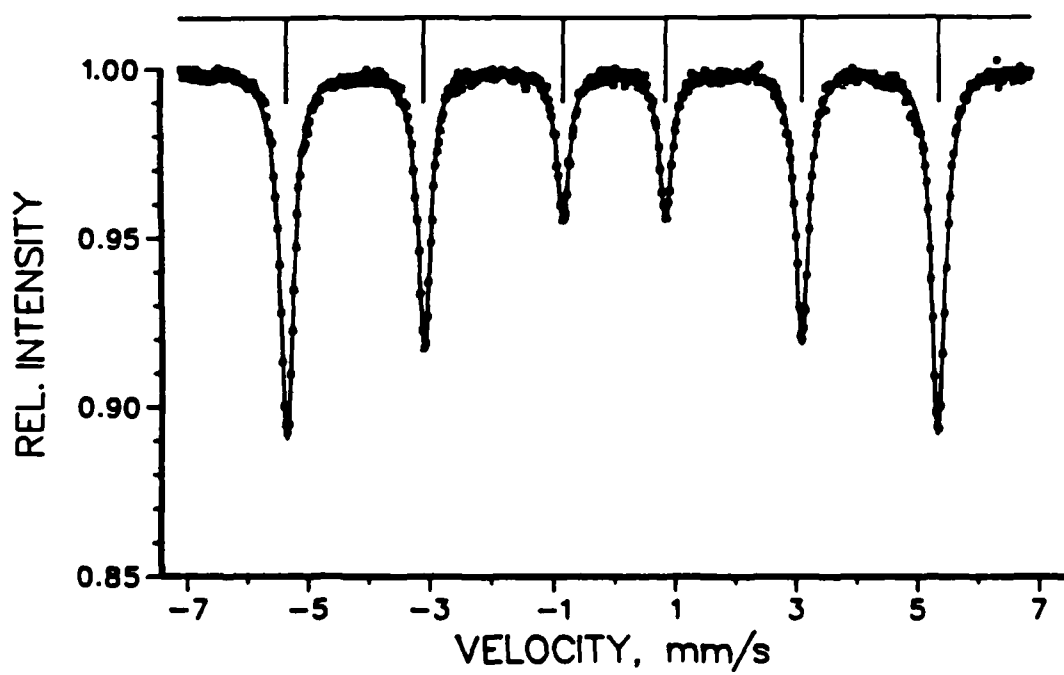
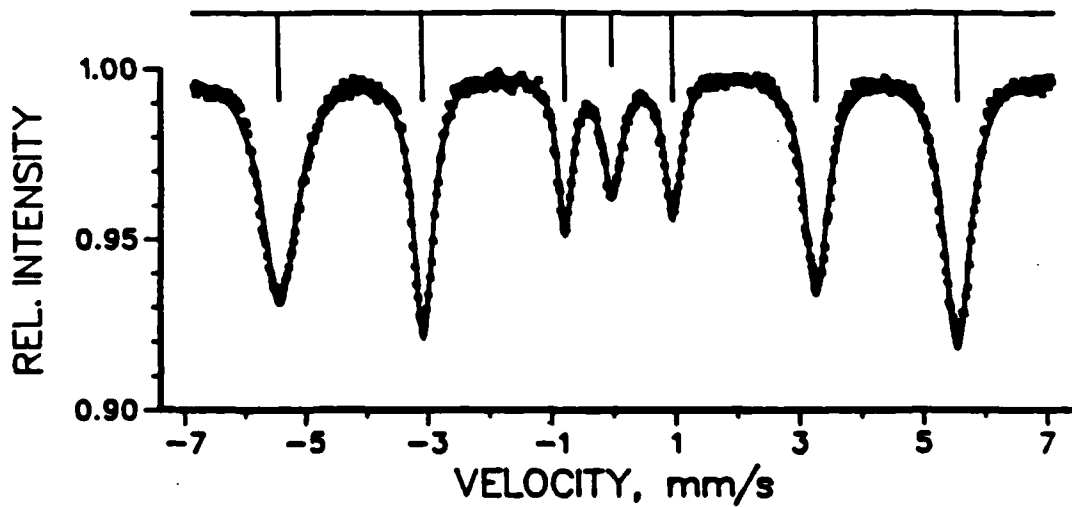
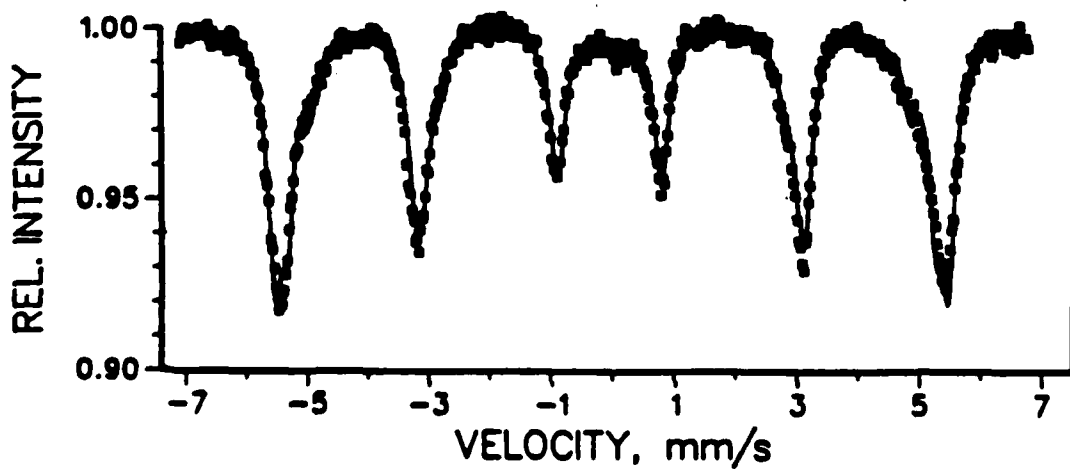


Figure 4.26 - Mossbauer spectrum from the 12 μm thick natural-Fe ($\approx 2\%$ Fe-57) foil used to calibrate the spectrometer.



(a)



(b)

Figure 4.27 - Mossbauer spectra from $\approx 10 \mu\text{m}$ thick foils of Fe-30Ni (a) as cooled to -196°C and (b) cooled to -196°C , cold rolled, and aged 20,000 hr at 335°C .

right, the relative widths are

$$\Gamma_1 > \Gamma_6, \Gamma_2 < \Gamma_5, \text{ and } \Gamma_3 < \Gamma_4.$$

Since the martensite has cubic symmetry the asymmetric subspectra was unexpected. van Deen (128) reported a similar pattern for Fe-Pd alloys and explained it as follows. Even though the crystal symmetry is cubic when averaged over many unit cells, the local symmetry in each unit cell might not be cubic if it contains both solute and solvent atoms. Consider an Fe-57 atom with seven Fe neighbors and one Ni neighbor. This asymmetry changes the electromagnetic environment of the Fe-57 atom, causing an electric quadrupole splitting and a change in the magnetic dipole splitting. Since the magnitude of both splittings is proportional to $3\cos^2\theta - 1$, where θ is the angle between the local direction of magnetization and the line connecting the Fe-57 atom to the Ni neighbor, the apparent relative peak widths are changed as above rather than broadened symmetrically.

The spectrum from the cold rolled and aged specimen is shown in Figure 4.27b. The central peak from retained paramagnetic austenite is gone because (1) cold rolling promoted the transformation to martensite and (2) austenite is enriched with enough Ni at the aging temperature to become ferromagnetic. Peaks 1, 2, 5, and 6 show shoulders and/or broadening on their sides nearest 0 mm/s, indicating that there are overlapping subspectra. This spectrum was deconvoluted by fitting to it three six-line subspectra. The results are listed in Table 4.4 together with hyperfine parameters from the literature (129 and others) for several Fe-Ni phases.

The near-zero quadrupole splittings of the fitted subspectra show that the phases present have cubic symmetry. The magnetic field strength of subspectrum 1 is equal to those for bcc Fe-5Ni and bcc Fe-30Ni phases. Both of these probably are present; the 30 wt% Ni material being the martensite, and the 5 wt% Ni material being ferrite formed from decomposition of martensite. The magnetic field strength of subspectrum 3 is very close to that reported for an fcc Fe-50Ni phase, and therefore must be due to the austenite formed from the decomposition of martensite. The magnetic field strength of subspectrum 2 is close to that of pure iron. It seems highly unlikely however that ferrite containing much less than 5 wt% Ni is present. Subspectrum 2 is also apparently not due to FeNi or FeNi₃. Subspectrum 2 is probably not due to any unique phase, but is a result of the fitting procedure. Recall that the fit subspectra were constrained to be symmetric, have the ideal 3:2:1:1:2:3 peak intensity ratios, and have peak widths of 0.277 mm/s.

Since the peaks of the actual spectrum probably were shifted and broadened as discussed above, a third fit subspectrum was required to achieve a statistically good fit.

Table 4.4 - Hyperfine Parameters for the Subspectra Fitted to the Spectrum in Figure 4.27b and for Various Fe-Ni Phases.

<u>Spectrum</u>	<u>Area</u>	<u>IS,</u> <u>mm/s</u>	<u>QS,</u> <u>mm/s</u>	<u>MF,</u> <u>kOe</u>
Subspectrum 1	0.49	0.025	0.001	-341
bcc Fe-5Ni	-	-	0.0	-340
bcc Fe-30Ni	-	-	0.0	-340
Subspectrum 2	0.36	0.023	0.0	-328
FeNi	-	-	0.1 to 0.2	-285 to -300
FeNi ₃	-	-	0.0	-290
bcc Fe	-	0.0	0.0	-330
Subspectrum 3	0.15	0.032	0.001	-303
fcc Fe-50Ni	-	-	0.0	-305

Several attempts were made to have the program fit asymmetric subspectra to the data. Specifically the parameters for FeNi listed in Table 4.4 were given as starting values in the iterative fitting algorithm. In all cases the program returned subspectra having nearly zero quadrupole splitting.

In summary, the Mossbauer results from an Fe-30Ni martensite cold rolled and aged 20,000 hr at 335°C indicate that the phases present are bcc Fe-5Ni, bcc Fe-30Ni, and fcc Fe-50Ni.

As discussed in Chapter 2, several investigators have detected the FeNi (Ll₀) phase in Fe-Ni alloys. In all of these cases the specimens in which the FeNi formed were austenitic. Therefore, it might not be surprising that FeNi did not form in the martensitic specimens aged in this study. The fact that the austenitic specimens aged in this study did not age harden suggests that FeNi did not form in these specimens either.

CHAPTER 5

SUMMARY OF RESULTS AND CONCLUSIONS

1. Binary Fe-Ni martensites containing 24 to 34 wt% Ni hardened during long-time aging at temperatures between 270 and 450°C. The hardening response was greatest for an Fe-32Ni martensite which hardened by 270 HV up to 480 HV upon aging for 8000 hr at 300°C.

2. Cold rolling of an Fe-30Ni martensite to 50% reduction before aging at 300°C increased the peak hardness from 450 to 565 HV but had little effect on the maximum amount of age hardening.

3. Binary Fe-Ni austenites containing 30 to 34 wt% Ni did not harden upon aging.

4. Age hardening of the martensites was due to the precipitation of Ni-rich, disc-shaped, austenite particles on {110} matrix planes. The typical particle in a hardened specimen was 15 nm in thickness by 150 nm in diameter. Ni contents of particles formed at 335 and 370°C were found to be 59±5 and 57±5 wt%, respectively. Ordering was not detected.

ACKNOWLEDGEMENTS

The authors are grateful to the U.S. Steel Corporation Research Laboratory for supplying the alloys used in this study. We are also grateful to G.J. Brooks and H.G. Hohnke for instruction on the use of the x-ray equipment and the electron microscopes.

AD-A161 407

AGE HARDENING OF BINARY IRON-NICKEL MARTENSITES(U)
MICHIGAN UNIV ANN ARBOR DEPT OF MATERIALS AND
METALLURGICAL ENGINEERING J T CARTER ET AL JUL 85

2/2

UNCLASSIFIED

ARO-17752.3-MS DAAG29-81-K-0052

F/G 11/6

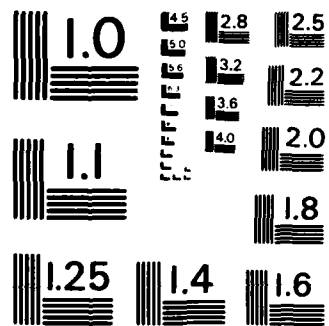
ML



END

FORM

100



MICROCOPY RESOLUTION TEST CHART
NATIONAL BUREAU OF STANDARDS - 1963 - A

APPENDIX

DERIVATION OF EQUATION 3.2

Let I_{220}^f , I_{211}^f , and I_{311}^f be the integrated intensities of the 220γ , $211a$, and 311γ (x-ray) reflections from a specimen having a volume fraction f of the γ phase. Assuming that the intensity of a reflection is linearly proportional to the irradiated volume of the phase producing the reflection, for a two phase mixture of a and γ ,

$$I_{211}^f = C_a(1-f)V \quad \text{and} \quad (I_{220}^f + I_{311}^f) = C_\gamma fV, \quad (\text{A.1})$$

where V is the irradiated volume and C_a and C_γ are constants.

For two specimens of the same size, one being all a , the other all γ ,

$$I_{211}^0 = C_a V \quad \text{and} \quad (I_{220}^1 + I_{311}^1) = C_\gamma V. \quad (\text{A.2})$$

Therefore,

$$R = \frac{C_a}{C_\gamma} = \frac{I_{211}^0}{I_{220}^1 + I_{311}^1}. \quad (\text{A.3})$$

From A.1 and A.3,

$$I_{211}^e = RC_\gamma(1-f)V \quad \text{and} \quad (I_{220}^f + I_{311}^f) = C_\gamma fV. \quad (\text{A.4})$$

Solving for f ,

$$C_\gamma = \frac{I_{211}^e}{R(1-f)V} = \frac{(I_{220}^f + I_{311}^f)}{fV}, \quad (\text{A.5})$$

$$fI_{211}^f = R(1-f)(I_{220}^f + I_{311}^f). \quad (\text{A.6})$$

Finally,

$$f = \frac{R(I_{220}^f + I_{311}^f)}{I_{211}^f + R(I_{220}^f + I_{311}^f)}. \quad (\text{A.7})$$

REFERENCES

1. R.L. Miller and W.C. Leslie, "Age Hardening in Binary Martensitic Fe-Ni Alloys", Scripta Met. 12, 1125-30(1978).
2. V.F. Buchwald, "The Iron-Nickel-Phosphorous System and the Structure of Iron Meteorites", Acta Polytechnica Scandinavica, Chemistry Including Metallurgy Series, No. 51, Copenhagen, 4-46(1966).
3. S. Floreen, "The Physical Metallurgy of Maraging Steels", Met. Rev., Review 126, 115-128(Sept 1968).
4. W.C. Leslie, The Physical Metallurgy of Steels, McGraw-Hill, New York, New York, 1981, p. 293.
5. R.F. Decker, J.T. Eash, and A.J. Goldman, "18% Ni Maraging Steel", Trans. ASM 55, 58-76(1962).
6. T. Suzuki, "Precipitation Hardening in Maraging Steels-On the Martensitic Ternary Iron Alloys", Trans. ISIJ 14, 67-81(1974).
7. G.R. Speich, "Age-Hardening of Fe-20Pct Ni Martensites", Trans. AIME 227, 1426-32(1963).
8. J.R. Mihalisin, "Age Hardening and Structure of Iron-Nickel-Cobalt Alloys", Trans. ASM 59, 60-70(1966).
9. M. Tanaka, T. Suzuki, and J. Komura, "On the Age-Hardening of Fe-Ni-Co Martensitic Alloys", Bull. Tokyo Inst. Tech., No. 82, 65-77(1967).
10. M. Tanaka, T. Suzuki, "On the Isothermal Age-Hardening of Fe-Ni-Co Martensitic Alloys", Bull. Tokyo Inst. Tech., No. 112, 49-60(1972).
11. G. Thomas, I. Cheng, and J.R. Mihalisin, "Precipitation in Fe-Ni-Co Alloys", Trans. ASM 62, 852-57(1969).
12. D.R. Squires and E.A. Wilson, "Aging and Brittleness in an Fe-Ni-Mn Alloy", Met. Trans., 3, 575-81(1972).
13. R.L. Miller, "Age Hardening in Ni-Mn Steels", U.S. Steel Research Laboratory Report No. 1642, (1972).

14. J.S. Marsh, Alloys of Iron and Nickel I, McGraw-Hill, New York, New York, 1938, p. 54.
15. G.R. Speich, "Constitution of Ternary Alloys Cr-Fe-Ni" in Metals Handbook 8, 8th ed., ASM, Metals Park, Ohio, 1973, pp. 424-26.
16. Y. Inokuti and B. Cantor, "The Microstructure and Kinetics of Martensite Transformations in Splat-Quenched Fe and Fe-Ni Alloys - II. Fe-Ni Alloys", Acta Met. 30, 343-56(1982).
17. G. Sachs and J.W. Spretnak, "The Structure and Properties of Some Iron-Nickel Alloys", AIME Tech. Pub. No. 1246, 1-15(1940).
18. G.R. Speich and P.R. Swann, "Yield Strength and Transformation Substructure of Quenched Iron-Nickel Alloys", J. Iron Steel Inst. 203, 480-85(1965).
19. A. Gilbert and W.S. Owen, "Diffusionless Transformation in Iron-Nickel, Iron-Chromium and Iron-Silicon Alloys", Acta Met. 10, 45-54(1962).
20. W.D. Swanson and J.G. Parr, "Transformations in Iron-Nickel Alloys", J. Iron Steel Inst. 202, 104-06(1964).
21. J.M. Marder and A.R. Marder, "The Morphology of Iron-Nickel Massive Martensite", Trans. ASM 62, 1-10(1969).
22. L. Kaufman and M. Cohen, "The Martensitic Transformation in the Iron-Nickel System", Trans. AIME 206, 1393-1401(1956).
23. S. Jana and C.M. Wayman, "Martensite-to-Fcc Reverse Transformation in an Fe-Ni Alloy", Trans. AIME 239, 1187-1193(1967).
24. S. Shapiro and G. Krauss, "The Crystallography of the Reverse Martensitic Transformation in an Iron-Nickel Alloy", Trans. AIME 239, 1408-15(1967).
25. G. Krauss, Jr. and M. Cohen, "Strengthening and Annealing of Austenite Formed by the Reverse Martensitic Transformation", Trans. AIME 224, 1212-21(1962).
26. S. Jin, J.W. Morris, Jr., Y.L. Chen, G. Thomas, and R.I. Jaffee, "An Investigation of Transformation Strengthening in Precipitation-Hardened Fe-Ni Austenite", Met. Trans. A 9A, 1625-33(1978).
27. E.A. Owen and A.H. Sully, "The Equilibrium Diagram of Iron-Nickel Alloys", Phil. Mag., Series 7, 27, 614-638(1939).

28. E.A. Owen and Y.H. Liu, "Further X-Ray Study of the Equilibrium Diagram of the Iron-Nickel System", J. Iron Steel Inst. 163, 132-37(1949).
29. J.I. Goldstein and R.E. Ogilvie, "A Re-Evaluation of the Iron-Rich Portion of the Fe-Ni System", Trans. AIME 233, 2083-87(1965).
30. A.D. Romig, Jr. and J.I. Goldstein, "Determination of the Fe-Ni and Fe-Ni-P Phase Diagrams at Low Temperatures (700 to 300°C)", Met. Trans. A 11A, 1151-59(1980).
31. A. Ferro, G. Griffa, and I. Ortalli, "On Quench-Enhanced Ordering of Fe₅₀-Ni₅₀ Alloy", Il Nuovo Cimento 3B, (2), 269-80(11Giugno 1971).
32. G. Hausch and H. Warlimont, "Structural Inhomogeneity in Fe-Ni Invar Alloys Studied by Electron Microscopy", Physics Letters 36A, (5), 415-16(27 Sep 1971).
33. G. Hausch and H. Warlimont, "Single Crystalline Elastic Constants of Ferromagnetic Face Centered Cubic Fe-Ni Invar Alloys", Acta Met. 21, 401-14(1973).
34. R.A. Jago, private communication with W.C. Leslie, (16 Mar 81).
35. T. Heumann and G. Karsten, "Karbonylverfahren und Aufdampfverfahren zur Bestimmung von Phasengleichgewichten im Temperaturbereich geringer Beweglichkeit am Beispiel der Eisen-Nickel-Legierungen", Arch. Eisenhuttew. 34, 781-85(1963).
36. O. Dahl, "Zur Frage unterkühlbarer Zustandsänderungen in Eisen-Nickellegierungen", Z.F. Metallkunde 24 107-111(1932).
37. M Hansen and K. Anderko, Constitution of Binary Alloys, Second Ed., McGraw-Hill, New York, New York, 1958, pp. 677-84.
38. J.K. van Deen and F. van der Woude, "Evidence for Direct Order-Disorder Transition in Ni₇₃Fe₂₇", Phys. Rev. B 20, (1), 296-98(1 Jul 1979).
39. J. Pauleve, D. Dautreppe, J. Laugier, and L. Neel, "Une Nouvelle Transition Ordre-Desordre Dans Fe-Ni (50-50)", J. Phys. Rad. 23, 841-43(1962).
40. A. Chamberod, J. Laugier, and J.M. Penisson, "Electron Irradiation Effects on Iron-Nickel Invar Alloys", J. Mag. Mat's. 10, 139-144(1979).

41. P.L. Gruzin, Yu. L. Rodionov, and V.A. Pryakhin, "Phase Diagram of Fcc Iron-Nickel Alloys", Sov. Phys. Dokl. 25, (4), 306-08(April 1980).
42. G. Silvestre, A. Silvent, C. Regnard, and G. Sainfort, "Alliages de Nickel-Fer et de Nickel-Silicium ne Gonflant pas Sous Irradiation aux Neutrons Rapides", J. Nucl. Mat'ls. 57, 125-35(1975).
43. V.F. Buchwald, Handbook of Iron Meteorites, University of California Press, Berkeley, California, 1975.
44. L.S. Lin, J.I. Goldstein, and D.B. Williams, "Analytical Electron Microscopy Study of the Plessite Structure in the Carlton Iron Meteorite", Geochim. Cosmochim. Acta 41, 1861-74(1977).
45. E.R.D. Scott and R.S. Clarke, Jr., "Identification of Clear Taenite in Meteorites as Ordered FeNi", Nature 281, 360-62(4 Oct 1979).
46. S. Mehta, P.M. Novotny, D.B. Williams, and J.I. Goldstein, "Electron-Optical Observations of Ordered FeNi in the Estherville Meteorite", Nature 284, 151-53(13 Mar 1980).
47. J.F. Petersen, M. Aydin, and J.M. Knudsen, "Mossbauer Spectroscopy of an Ordered Phase (Superstructure) of FeNi in an Iron Meteorite", Physics Letters 62A, (3), 192-94(8 Aug 1977).
48. J.F. Albertsen, G.B. Jensen, and J.M. Knudsen, "Structure of Taenite in Two Iron Meteorites", Nature 273, 453-54 (8 Jun 1978).
49. J. Danon, R.B. Scorzelli, I. Souza-Azevedo, J. Laugier, and A. Chamberod, "Santa Catharina Meteorite and Phase Composition in Irradiated Fe-Ni Invar Alloys", Nature 284, 537-38(10 Apr 1980).
50. J.I. Goldstein and D.B. Williams, "Low Temperature Phase Transformations in the Metallic Phases of Meteorites" in Solid-Solid Phase Transformations, (Proc. Conf. 10-14 Aug 1981), H.I. Aaronson, D.E. Laughlin, R.F. Sekerka, and C.M. Wayman Eds., AIME, Warrendale, Pennsylvania, (1982), pp. 715-20.
51. J. Danon, R.B. Scorzelli, I. Souza-Azevedo, and M. Christophe-Michel-Levy, "Iron-Nickel Superstructure in Metal Particles of Chondrites", Nature 281, 469-71(11 Oct 1979).

52. J. Danon, R.B. Scorzelli, and I.S. Azevedo, "Mossbauer Studies of the FeNi Ordered Phase (Superstructure $L1_0$) in Meteorites", J. Physique 41, C1-363-64(1980).
53. J.F. Albertsen, J.M. Knudsen, N.O. Roy-Poulsen, and L. Vistisen, "Meteorites and Thermodynamic Equilibrium in Fcc Iron-Nickel Alloys (25-50%Ni)", Phys. Scripta 22, 171-75(1980).
54. J.F. Albertsen, H.P. Nielsen, and V.F. Buchwald, "On the Fine Structure of Meteoritical Taenite/Tetrataenite and its Interpretation", Phys. Scripta 27, 314-20(1983).
55. K.B. Reuter, D.B. Williams, and J.I. Goldstein, "Microanalysis and Microdiffraction of Two-Phase Regions in the Metallic Phase of the Estherville Meteorite", in Analytical Electron Microscopy 1984 Conf. Proc., D.B. Williams and D.C. Joy, Eds., San Francisco Press, San Francisco, California, 1984, pp. 177-81.
56. J.S. Bowles, M. Hatherly, and A.S. Malin, "FeNi Superlattice Formation by Corrosion of Santa Catharina Meteorite", Nature 276, 168-69(9 Nov 1978).
57. R.I. Botto and G.H. Morrison, "Josephinite: A Unique Nickel-Iron", Amer. J. Sci. 276, 241-74(1976).
58. J. Danon, R.B. Scorzelli, I.S. Azevedo, J.F. Albertsen, J.M. Knudsen, N.O. Roy-Poulsen, Y. Minai, H. Wakita, and T. Tominaga, "Iron-Nickel Alloy Superstructures in the Mineral Josephinite", Radiochem. Radioanal. Letters 38, (5-6), 339-42(1979).
59. C.F. Jaczak, J.A. Larson, and S.W. Shin, Retained Austenite and Its Measurement by X-Ray Diffraction, SP-453, Society of Automotive Engineers, Warrendale, Pennsylvania, 1980.
60. E.E. Underwood, Quantitative Stereology, Addison-Wesley, Reading, Massachusetts, 1970.
61. R.L. Miller, "A Rapid X-Ray Method for the Determination of Retained Austenite", Trans. ASM 57, 892-99(1964).
62. G.T. Eldis, "Correlation of Measurements of Retained Austenite in Carburized Steels by X-Ray Diffraction and Quantitative Metallography", J. Heat Treating 1, (3), 24-30(1980).
63. B.D. Cullity, Elements of X-Ray Diffraction 2nd ed., Addison-Wesley, Reading, Massachusetts, 1978, p. 407.

64. B.L. Averbach and M. Cohen, "X-Ray Determination of Retained Austenite by Integrated Intensities", Trans. TMS-AIME 176, 401-15(1948).
65. M.R. James and J.B. Cohen, "A Portable Residual Stress Analyzer", Tech. Report 19, Dept. of Materials Science, Northwestern University, Evanston, Illinois, (1977).
66. S. Sekito, "A Quantitative Determination of Martensite and Austenite in Quenched and Tempered Steels by Means of X-Ray Analysis", Tohoku University Science Reports 20, ser. 1, 369-76(1931).
67. B.L. Averbach, L.S. Castleman, and M. Cohen, "Measurement of Retained Austenite in Carbon Steels", Trans. ASM 42, 112-20(1950).
68. K.E. Beu, "Modifications of an X-Ray Method for the Measurement of Retained Austenite Concentrations in Hardened Steels", Trans. AIME 194, 1327-28(1952).
69. J.L. Dietche, "Measurement of Retained Austenite with the X-Ray Spectrometer", U.S. Steel Research Laboratory Report No. 678, (1951).
70. S.L. Lopata and E.B. Kula, "Quantitative Phase Analysis in Textured Materials", Trans. AIME 233, 288-93(1965).
71. P.R. Morris, "Measurement of Retained Austenite in Precipitation Hardened Stainless Steels", Trans. AIME 239, 1586-90(1967).
72. M.J. Dickson, "The Significance of Texture Parameters in Phase Analysis by X-Ray Diffraction", J. Appl. Cryst. 2, 176-80(1969).
73. C.J. Ball and P.M. Kelly, "X-Ray Method for Determination of Retained Austenite in Steels with Pronounced Texture", Metal Science 16, 332-34(1982).
74. R.L. Miller, "Volume Fraction Analysis of Phases in Textured Alloys", Trans. ASM 61, 592-597(1968).
75. L.G. Schulz, "A Direct Method of Determining Preferred Orientation of a Flat Reflection Sample Using a Geiger Counter X-Ray Spectrometer", J. Appl. Physics 20, 1030-33(Nov. 1949).
76. W.P. Chernock and P.A. Beck, "Analysis of Certain Errors in the X-Ray Reflection Method for the Quantitative Determination of Preferred Orientations", J. Appl. Physics 23, 341-45(Mar 1952).
77. C. Kim, "X-Ray Method of Measuring Retained Austenite

in Heat Treated White Cast Irons", J. Heat Treating 1, (2), 43-52(1979).

78. R. Fillit, H. Bruyas, F. Maratray, and A. Poulalion, "Measurement of Austenite Content in Various Textured Alloys", Paper A82-10, AIME Annual Meeting, Dallas, Texas, (Feb 1982).

79. K.E. Beu and D.P. Koistinen, "Some Effects of Metal Removal and Heat Treatment on the Surfaces of Hardened Steels", Trans. ASM 48, 213-33(1956).

80. H. Marcus, L.H. Schwartz, and M.E. Fine, "A Study of Precipitation in Stainless and Maraging Steels Using the Mossbauer Effect", Trans. ASM 59, 468-78(1966).

81. G. Balestrino and M. Cavallini, "Mossbauer Spectroscopy Study of Retained Austenite Tempering in 4340 Steels", Scripta Met. 17, 1407-12(1983).

82. L.H. Schwartz and K.J. Kim, "A Mossbauer Study of the Surface Martensite in 1095 Steel", Met. Trans. A 7A, 1567-70(1976).

83. F.E. Huggins and G.P. Huffman, "Rapid Mossbauer-Based Methods for the Determination of Iron-Bearing Phases", J. Appl. Phys. 55, (5), 1404-09(1 Mar 1984).

84. G.P. Huffman and F.E. Huggins, "Applications of Mossbauer Spectroscopy in the Steel Industry" in Mossbauer Spectroscopy and Its Chemical Applications, (Advances in Chemistry Science Series 194), J.G. Stevens and G.K. Shenoy, Eds., Amer. Chem. Soc., Washington, D.C., 1981, pp. 265-301.

85. J.G. Stevens and R.S. Preston, "Useful Information for Fe-57 Mossbauer Spectroscopy" in Mossbauer Effect Data Index, J.G. Stevens and V.E. Stevens, Eds., IFI/Plenum, New York, New York, 1972, pp. 16-22.

86. D.B. Williams, Practical Analytical Electron Microscopy in Materials Science, Philips Electronic Instruments Inc., Mahwah, New Jersey, 1984, pp. 55-90.

87. J.I. Goldstein, "Principals of Thin Film X-Ray Microanalysis" in Introduction to Analytical Electron Microscopy, J.J. Hren, J.I. Goldstein, and D.C. Joy, Eds., Plenum Press, New York, New York, 1979, pp. 83-120.

88. N.J. Zaluzec, "Quantitative X-Ray Microanalysis: Instrumental Considerations and Applications to Materials Science" in Introduction to Analytical Electron Microscopy, J.J. Hren, J.I. Goldstein, and D.C. Joy, Eds., Plenum Press, New York, New York, 1979, pp. 83-120.

89. G. Cliff and G.W. Lorimer, "The Quantitative Analysis of Thin Specimens", J. Microscopy 103, pt. 2, 203-207(Mar 1975).
90. A.D. Romig, Jr., "Quantitative X-Ray Microanalysis of Uranium Alloys in the Analytical Electron Microscope", J. Microscopy 135, pt. 2, 191-202(Aug 1984).
91. J. Philibert and R. Tixier, "Electron Probe Microanalysis of Transmission Electron Microscope Specimens" in Physical Aspects of Electron Microscopy and Microbeam Analysis, B.M. Siegel and D.R. Beaman, Eds., John Wiley and Sons, New York, New York, 1975, pp. 333-354.
92. R. Konig, "Quantitative X-Ray Microanalysis of Thin Foils" in Electron Microscopy in Minerology, H.R. Wenk, Ed., Springer-Verlag, New York, New York, 1976, pp. 526-536.
93. J.I. Goldstein, J.L. Costley, G.W. Lorimer, and S.J.B. Reed, "Quantitative X-Ray Analysis in the Electron Microscope" in Scanning Electron Microscopy I, O. Johari, Ed., IIT Research Institute, Chicago, Illinois, 1977, pp. 315-24.
94. A.D. Romig, Jr., Determination of the Iron-Nickel and Iron-Nickel-Phosphorus Phase Diagrams at Low Temperatures, Ph. D. Dissertation, Lehigh University, Bethlehem, Pennsylvania, 1979, pp. 27-30.
95. L.F. Allard and D.F. Blake, "The Practice of Modifying an Analytical Electron Microscope to Produce Clean X-Ray Spectra" in Microbeam Analysis-1982, K.F.J. Heinrich, Ed., San Francisco Press, San Francisco, California, 1982, pp.8-20.
96. R. Mossbauer, "Kernresonanzfluoreszenz von Gammastrahlung", Z. Physik 151, 124(1958).
97. Mossbauer Spectroscopy, Topics in Applied Physics Vol. 5, U. Gonser, Ed., Springer-Verlag, New York, New York, 1975.
98. A. Vertes, L. Korecz, and L. Burger, Mossbauer Spectroscopy, Studies in Physical and Theoretical Chemistry Series, No. 5, Elsevier Scientific, New York, New York, 1979.
99. G.M. Bancroft, Mossbauer Spectroscopy, McGraw-Hill, London, 1973.
100. N.N. Greenwood and T.C. Gibb, Mossbauer Spectroscopy, Chapman and Hall, London, 1972.

101. Applications of Mossbauer Spectroscopy, R.L. Cohen, Ed., Academic Press, New York, New York, Vol. 1 1976, Vol. 2 1980.
102. J.G. Stevens, G.H.M. Calls, and L.H. Bowen, "Mossbauer Spectroscopy", Anal. Chem. 54, 204R-216R(1982).
103. G.C. Bonazzola, T. Bressani, E. Chiavassa, G. Dellacasa, A. Musso, and B. Minetti, "Possible Improvements of Mossbauer Spectrometers with the Use of Multiwire Proportional Counters", J. Physique 35, (12), C6-687-690(1974).
104. T.H. Gould, Jr., and D.H. Vincent, "Mossbauer Spectroscopy Study of Aging and Fast Neutron Irradiation Effects in a Copper-Rich Cu-Fe Alloy", J. Physique 35, (12), C6-315-19(1974).
105. A.H. Muir, Jr., "Analysis of Complex Mossbauer Spectra by Stripping Techniques" in Mossbauer Effect Methodology Vol. 4, I.J. Gruverman, Ed., Plenum Press, New York, New York, 1968, pp. 75-101.
106. P.E. Clark and S.J. Campbell, "Some Applications of Mossbauer Spectroscopy to Physical Metallurgy", Metals Forum 3, (2), 95-108(1980).
107. Metals Handbook, 8th Ed., Vol. 11, ASM, Metals Park, Ohio, 1976, p.13.
108. C. Lipson and N.J. Sheth, Statistical Design and Analysis of Engineering Experiments, McGraw-Hill, New York, New York, 1973, pp. 13,76.
109. B.D. Cullity, Elements of X-Ray Diffraction, 2nd Ed., Addison-Wesley, Reading, Massachusetts, 1978, p. 392.
110. A. Chamberod, J. Laugier, and J.M. Penisson, "Electron Irradiation Effects on Iron-Nickel Invar Alloys", J. Mag. Mat'ls 10, 139-144(1979).
111. E.A. Fischione Instrument Manufacturing, Pittsburgh, Pennsylvania.
112. Instruction Manual 200-319, Leco Corporation, St. Joseph, Michigan, 1982, p. 4.
113. Instruction Manual 200-306, Leco Corporation, St. Joseph, Michigan, 1980, p. 4.
114. Model 550C thinner, South Bay Technology, Temple City, California.

115. G.F. Knoll, Radiation Detection and Measurement, John Wiley and Sons, New York, New York, 1979, p. 137.
116. Elscint, Hackensack, New Jersey.
117. Ranger Engineering, Fort Worth, Texas.
118. Tennelec, Oak Ridge, Tennessee.
119. Nuclear Data, Schaumburg, Illinois.
120. New England Nuclear, North Billerica, Massachusetts.
121. Alfa Products, Danvers, Massachusetts.
122. W. Wilson and L.J. Swartzendruber, "A Flexible Least Squares Routine for General Mossbauer Effect Spectra Fitting", Computer Physics Communications 7, 151-162(1974).
123. S.S. Hanna, J. Heberle, G.J. Perlow, R.S. Preston, and D.H. Vincent, "Direction of the Effective Magnetic Field at the Nucleus in Ferromagnetic Iron", Phys. Rev. Letters 4, (10), 513-515(15 May 1960).
124. R.S. Preston, S.S. Hanna, and J. Heberle, "Mossbauer Effect in Metallic Iron", Phys. Rev. 128, (5), 2207-18(1 Dec. 1962).
125. S.V. Radcliffe and M. Schatz, "Effects of High Pressure on the Strength and Structure of Martensites", Nature 200, (4902), 161-63(12 Oct 1963).
126. J.W. Edington, Practical Electron Microscopy in Materials Science, Van Nostrand Reinhold, New York, New York, 1976, p. 100.
127. T.J. Headley, private communication, 21 Jan 1985.
128. J.K. van Deen, On Neighbors of Iron, Ph. D dissertation, University Groningen, 1980.
129. C.E. Johnson, M.S. Ridout, and T.E. Cranshaw, "The Mossbauer Effect in Iron Alloys", Proc. Phys. Soc. 81, 1079-1090(1963).

END

FILMED

1-86

DTIC